University of Zululand

University of Zululand

Faculty of Science and Agriculture

Department of Physics

The Study of Low lying Positive Parity Bands in ^{162}Yb.

Linda Mdletshe

A thesis presented for the degree of

Master of Science in Physics

Supervisor: Dr. S. S. Ntshangase[1]

Co-supervisors: Prof. J. F. Sharpey-Schafer[2], Dr. T. S. Dinoko[4] and Dr. S. N. T. Majola[1,3,4]

University of Zululand[1]

University of the Western Cape[2]

University of Stellenbosch[3]

iThemba LABS[4]

June 2017

Declaration

I declare that apart from the recognized references and help, the dissertation submitted for the Master of Science in Physics to the University of Zululand is my own work and has not been submitted to any other University for a degree.

Linda Mdletshe

Signed: ..... Date: .....

Abstract

Over the last decade, iThemba LABS has had an active research program that focuses on the spectroscopy of low lying positive parity bands [1–8], particularly the so-called β and γ vibrational bands, which are traditionally associated with the first excited $K^\pi = 0^+$ and $K^\pi = 2^+$ bands, respectively. Through this program, the nature of these bands has been studied extensively. However, despite this, the microscopic identity of these bands remains elusive in the transitional rare-earth region. This work seeks to give an insight on the microscopic nature of these bands by studying the spectroscopy of ^{162}Yb. The data for the nucleus of interest (^{162}Yb) was collected at iThemba LABS, using the ^{150}Sm (^{16}O, 4n) ^{162}Yb fusion evaporation reaction. The γ rays emitted from the reaction products were detected using the AFRODITE γ ray spectrometer [9] equipped with escape-suppressed clover detectors. A total of 10 bands have been observed in this work. The DCO and polarization measurements have not only been used to confirm assignments that were made by previous in-beam works on well established structures [10–12] - but have also been instrumental in the assignment of spins and parities for the majority of newly established bands in ^{162}Yb.

Further, the current study has not only confirmed all the rotational structures reported by previous in-beam works but has also extended the level scheme of ^{162}Yb by establishing 6 new bands. More importantly, a band built on the above-mentioned $K^\pi = 0^+$ excitation has been identified for the first time. In addition, for the first time in ^{162}Yb, we also report rotational levels that form band structures of both the odd and even spin components of the $K^\pi = 2^+$ γ vibrational band.

Contents

List of Figures

CHAPTER 1

1 Introduction

Many deformed nuclei have low-lying excitations which have traditionally been regarded as vibrations or rotations of the nuclear shape [13] . These collective excitations are observed with the quantum numbers $K^\pi = 0^+$, $K^\pi = 2^+$, $K^\pi = 0^-$ to 3^-. These states are traditionally regarded as the β (beta) and γ (gamma) and Ω (octupole) bands, respectively, and they always lie within the pairing gap. Deformed nuclei in the transitional rare earth region have been studied extensively in recent years, particularly at low spin [1–7, 14]. Central to the focus of these studies is the fundamental question about the validity of the Bohr-Hamiltonian description of the first excited $K^\pi = 0^+$ band, in the $N \sim 90$ region, as a β vibration along the symmetry axis.

Even though investigations made in these studies continue to provide a useful insight on various aspects of the $K^\pi = 0^+$ states, a lack of experimental data still exist in some of these transitional rare-earth nuclei. The nucleus, ytterbium-162 (^{162}Yb), is one of the rare-earth nuclei which does not have sufficient data, more especially at low spin. Ytterbium-162 is an even-even nucleus with an atomic number $Z = 70$ and neutron number $N = 92$. Previous experiments [11, 12] made a successful attempt in identifying the band-heads of some of the low-lying excited states in ^{162}Yb, namely the $K^\pi = 0^+$ and $K^\pi = 2^+$ states, which are traditionally associated with the so-called β and γ vibrational bands, respectively. The current study has fully established rotational structures built on these bands (i.e. β and γ vibrational bands) in ^{162}Yb. The microscopic properties of these bands are then theoretically explained with the aid of the five-dimensional collective Hamiltonian (5DCH) based on the covariant density functional theory (CDFT) [15–18]. In a search for a definitive and complete microscopic picture of the so-called γ and β vibrational bands in the transitional rare earth nuclei, a comprehensive systematic review has been performed for nuclei in the $A \sim 160$ mass region - with emphasis on $N \sim 90$ isotones.

Some of the experimental results obtained in this work are explained using the Cranked-Shell Model (CSM) [19]. Shown in Figure 1 is the neutron CSM quasiparticle diagram

for ^{162}Yb showing the quasiparticle energy, expressed in units of the harmonic oscillator energy $\hbar\omega_0$ as a function of the rotational frequency, expressed in units of the harmonic frequency ω_0. The parameters used to construct this diagram are shown on top of Figure 1, where ε_2 is the quadrupole deformation parameter, ε_4 is the hexadecapole deformation parameter, ω_0 is the harmonic oscillator frequency, λ is the Fermi energy, and Δ is the paring gap parameter.

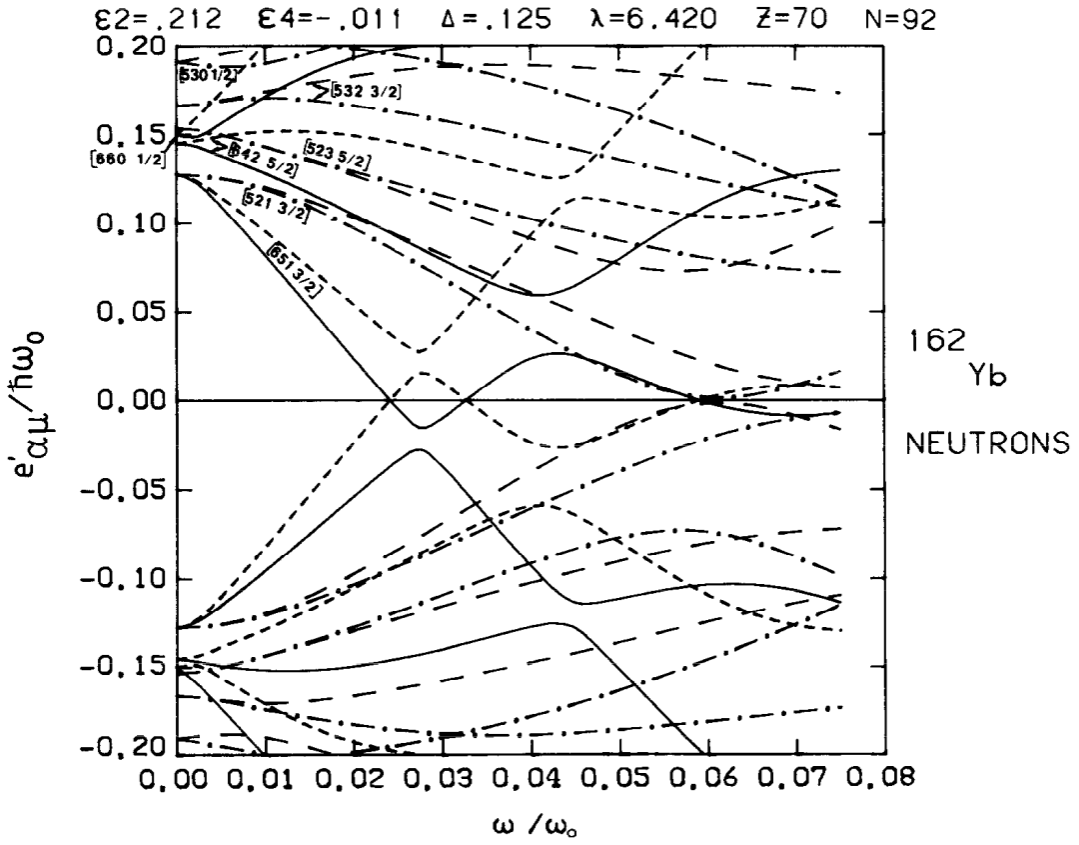

Figure 1: Shows the neutron CSM quasiparticle diagram for the nucleus ^{162}Yb. The solid lines and dotted-lines correspond to trajectories with positive parity and signatures $\alpha = 1/2$ and $\alpha = -1/2$ respectively, whereas the dashed-lines and dashed-dotted lines correspond to trajectories with negative parity and signatures $\alpha = -1/2$ and $\alpha = 1/2$ (see ref. [18]).

CHAPTER 2

2 Nuclear Structure Theory

Experimental observations and construction of models made in nuclear physics to interpret the structure and the behavior of the nucleus have led us to a better understanding of nuclear structure. Major models of a nucleus, the liquid-drop and shell model, had great success in explaining the fundamental properties of nuclei but failed to explain some of the properties. The liquid-drop model, formulated by N. Bohr [20], had a great success in explaining the properties of heavy nuclei, such as uranium. It modeled the atomic nucleus as a drop of liquid held together by surface tension. In 1939 [21], N. Bohr and J. A. Wheeler used this model to explain nuclear fission, that is, a heavy atomic nucleus, such as uranium, could split to form new lighter nuclei.

On the other hand, the shell model was actually good at explaining the properties of lighter nuclei. It also explained why the atomic nuclei with magic numbers are more stable than normally stable nuclei, but was less successful in describing some of the fundamental properties observed in heavy nuclei, such as uranium. Magic numbers $(2, 8, 20, 28, 50, 82, 126)$ can be well explained in terms of this model, which considers each nucleon to be moving in some mean field potential and classifies the energy level in terms of quantum numbers (nlj). This model predicted the electric quadrupole moments to be very small. However, heavier nuclei with mass numbers (A) in the range $A = 150 - 190$ and $A > 220$ [22], have larger electric quadrupole moments. The failure of this model to correctly predict the electric quadrupole moments for heavy nuclei arises from the assumption that the nucleons move in a spherically symmetric potential.

2.1 The Collective Model

It was clear that both ideas of the liquid-drop and shell models could not fully explain the properties of the atomic nucleus individually. The limited success made by these models led to a combination of their ideas into a single unified model of the nucleus, initially suggested by J. Rainwater [23]. The unified model is currently known as the collective nuclear model. This model, proposed by A. Bohr and B. R. Mottelson in 1953 [24],

considers the motion of the whole nucleus. It takes the effect of non-spherically symmetric potentials into consideration, which leads to a large deformation for heavier nuclei, and therefore large electric quadrupole moments. In this model, the kind of motions that the nucleus can have is divided into two parts, rotational and vibrational motions. These collective motions are discussed in the following subsections.

2.1.1 Rotational motion

A nucleus that is not deformed or whose nucleon density distributions are spherically symmetric cannot have rotational excitations [22]. The quadrupole moment of such a nucleus is zero, however, a nucleus with non-zero quadrupole moment can have excited levels due to rotation about axes perpendicular to the axis of symmetry.

The rotation of a deformed nucleus about the axis through the center perpendicular to the axis of symmetry is shown in Figure 2. These excited levels have different energies, depending on the number of nucleons in a nucleus.

For a nucleus whose atomic and neutron number are both even (even-even nucleus), the ground state has spin zero and the excited rotational levels (E_{Rot}) are given by equation 1 [25],

$$E_{Rot} = \frac{I(I+1)\hbar^2}{2\mathcal{I}} \tag{1}$$

where I is the rotational spin, and $\mathcal{I}$ is the moment of inertia of the nucleus. For an axially derformed even-even nuclei with $K = 0$, only even values of I are allowed. Equation 2 shows a numerical description of rotational levels corresponding to odd nuclei.

$$E_{Rot} = \frac{(I(I+1) - K(K+1))\hbar^2}{2\mathcal{I}} \tag{2}$$

where K is the non-zero spin of the ground state and in these nuclei I can take the values $K+1$, $K+2$, $K+3$ etc.

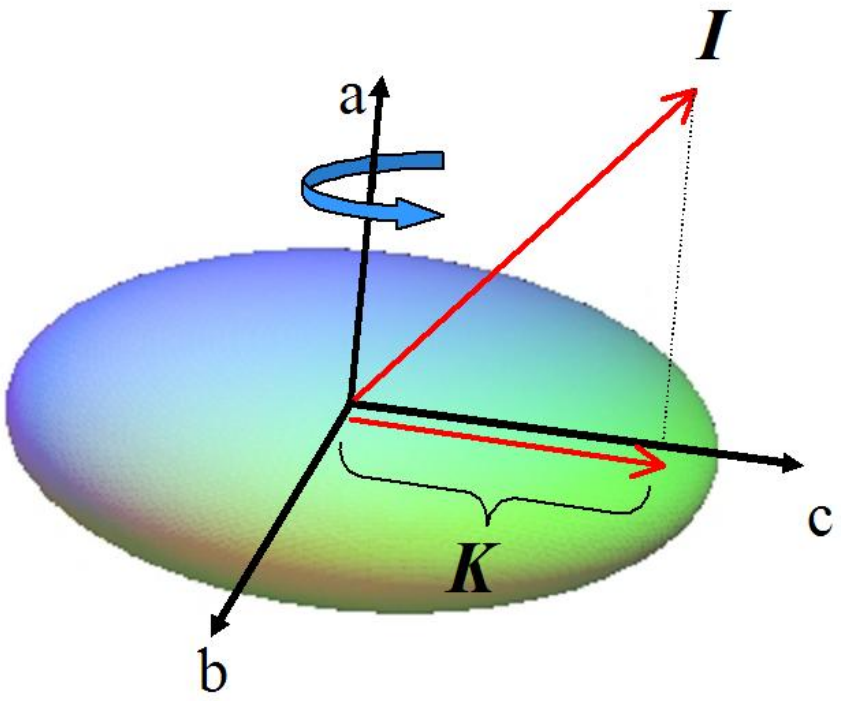

Figure 2: A deformed nucleus with axial symmetry showing the rotation axis (a), the nuclear symmetry axis (c), the total angular momentum (I), and projection K onto (c) [26].

2.1.2 Vibrational motion

There are different modes of vibration that have been observed in nuclei, namely dipole vibration, quadrupole vibration , octupole vibration, etc.

Equation 3 [22] is used to describe the vibrational modes of a nucleus. If the shape of a nucleus is changing from spherical to non-spherical as a function of time, the shape can be described in terms of distinct surface points from the center of the nucleus as a function of (θ, ϕ). If the distance (R) is the same from all points on the surface to the center, then the surface is spherical, this means R does not depend on (θ, ϕ). The distance R becomes a function of (θ, ϕ) if the surface is non-spherical and can be expanded in terms of spherical harmonics $Y_{\lambda\mu}(\theta, \phi)$. The time dependent coordinate $R(t)$, in the direction (θ, ϕ), is given by equation 3 ,

$$R(t) = R_{av} + \sum_{\lambda \geq 1} \sum_{\mu=-\mu}^{+\lambda} a_{\lambda\mu}(t) Y_{\lambda\mu}(\theta, \phi) \tag{3}$$

where R_{av} is an average radius and $a_{\lambda\mu}(t)$ is an expansion coefficient (time dependent).

The dipole vibration ($\lambda = 1$) corresponds to shifts of the center of mass of the nucleus. However, higher order terms (i.e. $\lambda = 2$, $\lambda = 3$, etc.) do cause distortion of the surface.

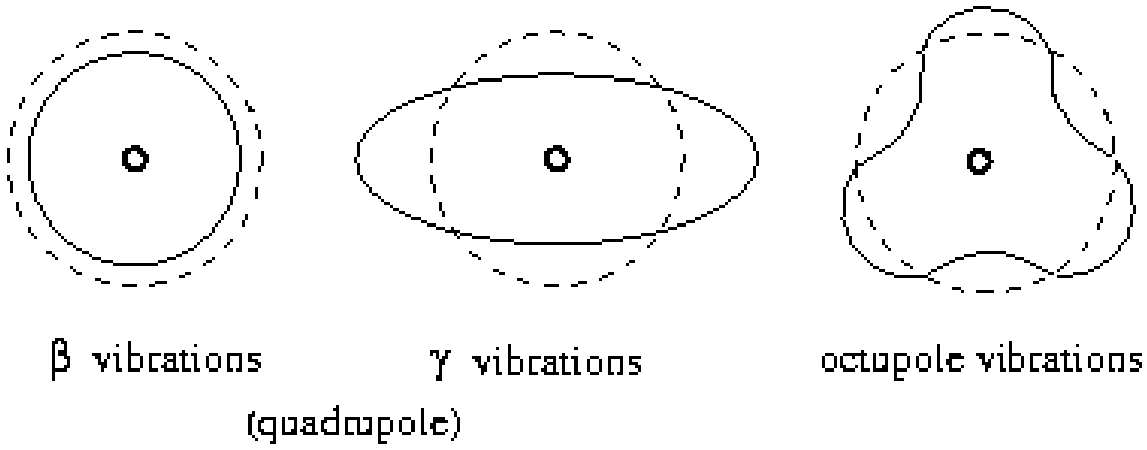

Figure 3: The different modes of vibration, showing quadrupole and octupole vibrations when viewed along the symmetry axis [27].

The quadrupole vibration ($\lambda = 2$) is divided into two parts, the first one is γ vibration and the second one is the β vibration. In a γ vibration, a cut in a plane perpendicular to the symmetry axes of the nucleus oscillate between a spherical shape and an ellipsoidal shape. When a nucleus is in a β vibration mode, the nucleons move inward and outward from the center of the nucleus in phase with one another, so that nucleus expands and contracts along the symmetry axis (see Figure 3). The octupole vibration ($\lambda = 3$), is a vibration of a nuclear shape in which the nucleus is deformed from a spherical to a pear shape. This type of vibration is shown in Figure 3, together with the quadrupole vibrations.

The typical spectra for low-lying excitation (together with the ground-state band) with quantum numbers $K^\pi = 0^+$ and $K^\pi = 2^+$ in many deformed nuclei [28] is shown in Figure 4. These low-lying excitations have traditionally been identified as a β-vibration ($K^\pi = 0^+$) and a γ-vibration ($K^\pi = 2^+$) [29]. However, the experimental evidence shows that these low-lying excitations $K^\pi = 0^+$ may not be due to β-vibrations but to 2p-2p neutron pairing isomers forming a 'second vacuum' (SV) on which all the normal nuclear excitations are built [1, 2], this shall be discussed in more detail in Chapter 5.

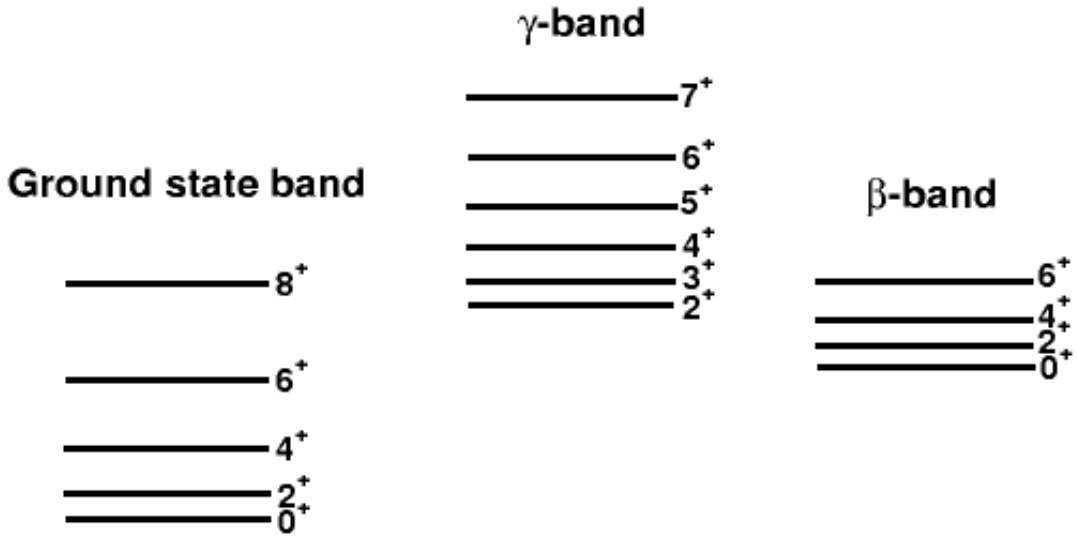

Figure 4: Diagram showing the ground-state, γ and β bands for the deformed nucleus.

3 Experimental Details

The experiment was carried out at iThemba LABS, and the objective was to study the detailed spectroscopy of the nucleus ^{162}Yb at low spin. The fusion-evaporation reaction ^{150}Sm(^{16}O,4n)^{162}Yb was used to populate the excited states of ^{162}Yb. The ^{16}O beam of 83 MeV, delivered by the Separated-Sector Cyclotron (SSC), shown in Figure 5, was used to bombard a ^{150}Sm target of 3 mg/cm^2 with 95.59% of isotopically enrichment. This experiment was run over one weekend. With the target thickness that was used, beams of less than 10 pnA were able to give enough counting rate to acquire 7.4$\times$ 10^9 $\gamma\gamma$ coincidences in the allocated time. The γ rays emitted during this fusion-evaporation experiment were detected using the AFRODITE γ ray spectrometer.

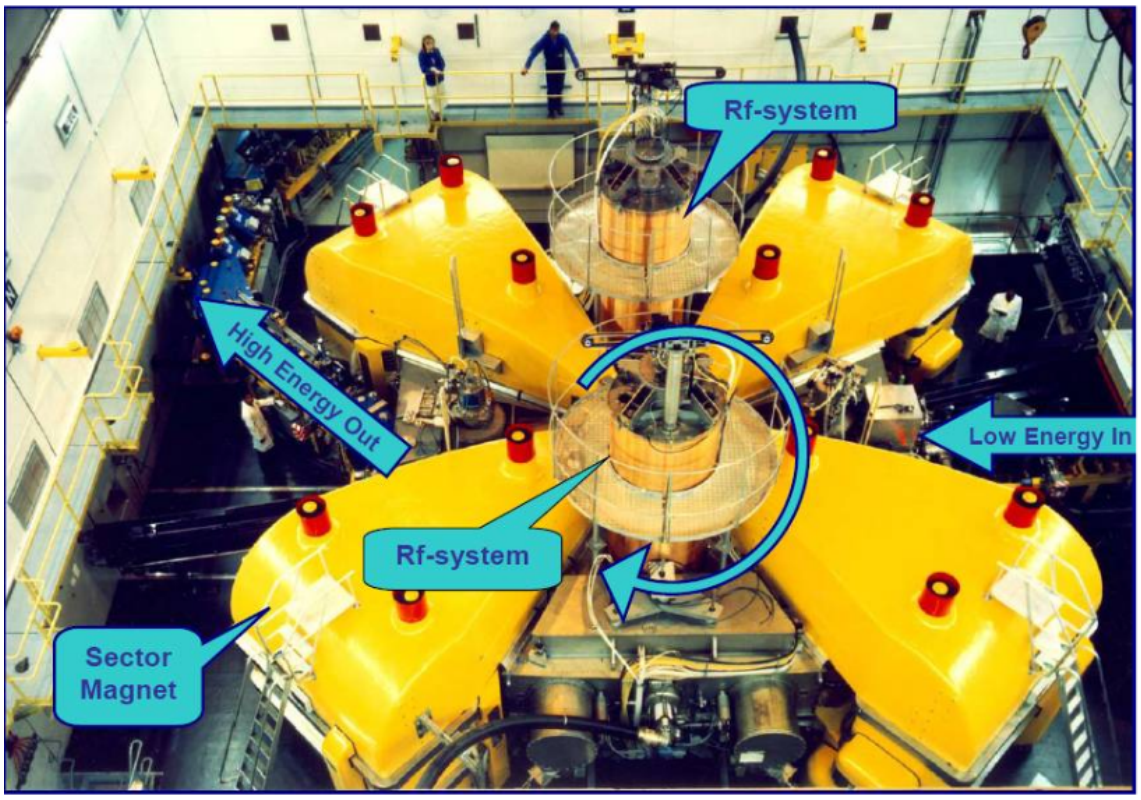

Figure 5: The K-200 SSC, at iThemba LABS, accelerates protons to energies of 200 MeV [30].

3.1 Fusion-evaporation reaction

There are different types of nuclear reactions that can be used to reach the highly excited states of a nucleus. In the present work, the fusion-evaporation reaction was used to excite the rotational states in ^{162}Yb.

Figure 6 shows how a fusion-evaporation reaction proceeds. In this reaction, a nuclear projectile comes into close contact with the target nucleus, resulting in the formation of a compound nucleus, which is highly unstable. One can think of this compound nucleus as a hot, charged, rotating liquid drop. The compound nucleus decays by either electromagnetic emission or particle evaporation; this is where alpha particles, protons, and neutrons are emitted from the compound nucleus. In a short period of time, of about 10^{-18} seconds, the compound nucleus decays rapidly, evaporating particles to carry away energy.

The evaporation of these particles leaves the nucleus cooled but not entirely. The nucleus at this point is still spinning at a very high rotational frequency. These evaporated particles decrease the excitation energy of the compound nucleus but carry off a little amount of angular momentum. The evaporation process stops when the excitation energy remaining in a nucleus is within one nucleon separation energy. After all possible particles have evaporated, the nuclear de-excitation continues by an emission of electromagnetic radiation and it eventually reaches the ground state.

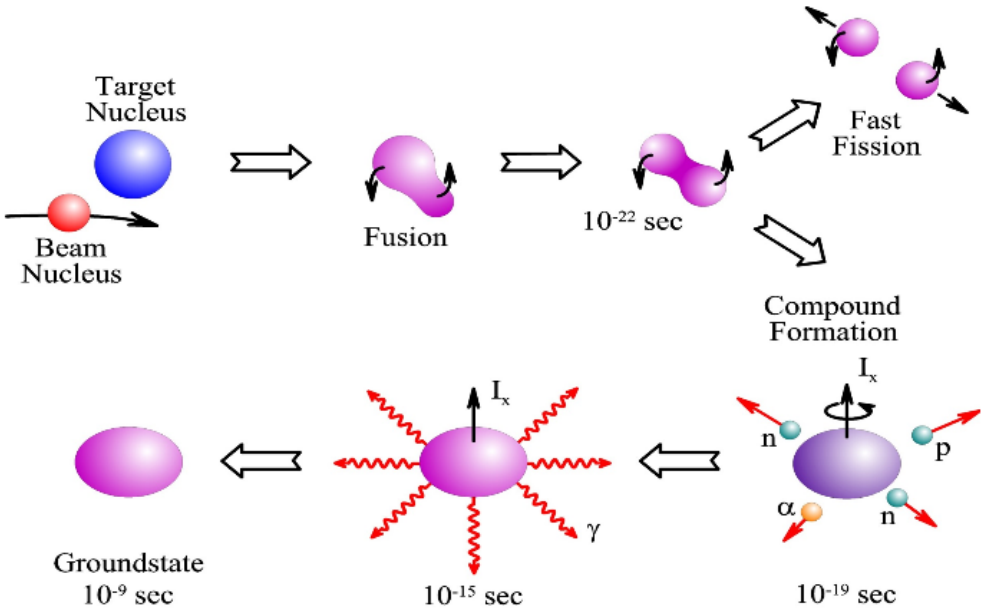

Figure 6: Schematic diagram showing how the fusion-evaporation reaction proceeds [31].

3.2 Choosing beam energy

Choosing suitable beam energy is one of the most important things to be taken into consideration when the fusion-evaporation reaction is used. In this reaction two nuclei composed of neutral and/or positively charged particles come close enough to interact and form one or more different atomic nuclei. Since both nuclei consist of positive charges, particularly protons, it is not easy to bring them into contact. One condition that has to be satisfied in order to fuse these nuclei is that the energy of the projectile nucleus (beam energy) must be high enough to overcome the electric repulsion between the protons (Coulomb barrier). In any fusion-evaporation experiment, it is important to calculate the Coulomb barrier before using any software simulation to estimate the suitable beam energy.

We used equation 4 [22] to calculate the Coulomb barrier (V_{cb}).

$$V_{cb} = \frac{1.44 Z_1 Z_2}{1.16(A_1^{\frac{1}{3}} + A_2^{\frac{1}{3}} + 2)} \tag{4}$$

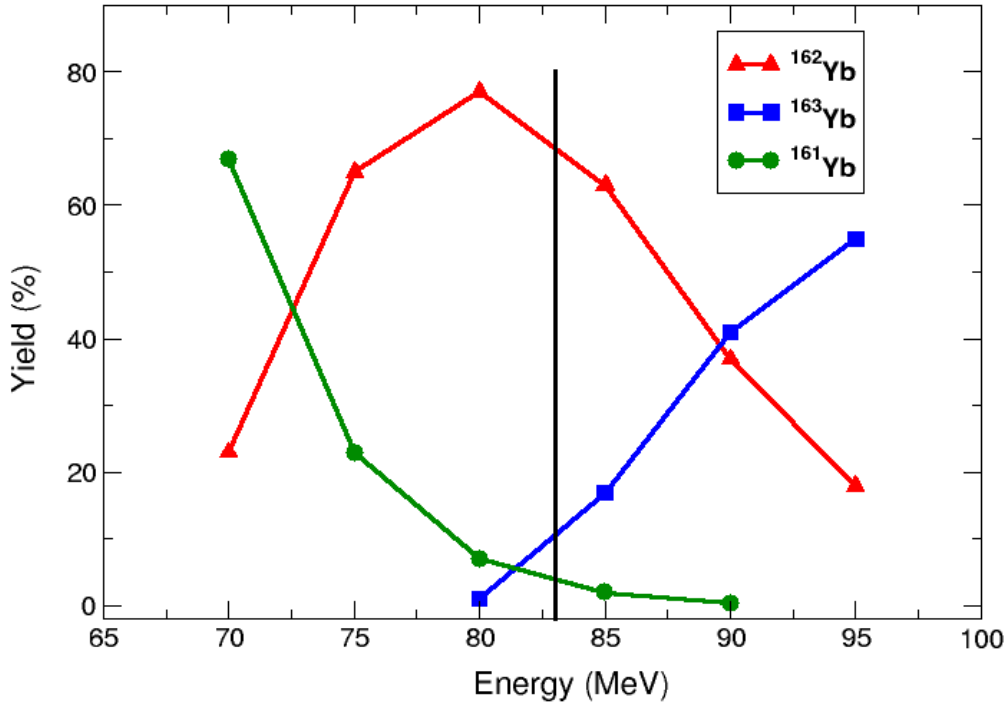

Figure 7: The calculated yield (%) curves for Yb isotopes and the vertical line indicating where the optimal beam energy was chosen.

In this equation, Z_1 and Z_2 represent the atomic numbers for the projectile and target nucleus respectively, whereas A_1 and A_2 denote the mass numbers for the projectile and target nucleus. The Coulomb barrier for our reaction, calculated using equation 4 is 62.6 MeV. After calculating the Coulomb barrier, the fusion-evaporation code PACE4 (Projected Angular-momentum Coupled Evaporation) [32] was then used to estimate the optimal beam energy. Figure 7 shows the calculated percentage yield curves for Yb isotopes that were populated during this fusion-evaporation experiment. The vertical line indicates where the beam energy (83 MeV) was chosen, which yields 71.3% of the nucleus of interest ^{162}Yb and less than 10% of each of the other isotopes. In Figure 7, it can be seen that the beam of 83 MeV is slightly above the maximum yield percentange of ^{162}Yb. The beam energy adjustment has been made in order to take into account the energy loss in the target.

3.3 Detection of gamma radiation

The γ rays that were emitted during this fusion-evaporation experiment were detected using the AFRODITE γ ray spectrometer [9]. This spectrometer was designed to detect both high and low energy photons with reasonably high efficiency by combining large volume escape suppressed High Purity Germanium (HPGe) detectors (clovers) with Low Energy Photon Spectrometers (LEPS). This array consists of 8 clover detectors, and 8 LEPS for photons between 30 and 300 keV. However, LEPS detectors were not used in the present work. Each clover detector consists of four HPGe crystals (see Figure 9). Under normal operation, these detectors need to be maintained at temperatures of approximately -180 ^{0}C. If any of these detectors is not in good condition, it has to be removed from the set up. Hence, in our experiment we used 7 clover detectors to detect γ rays that were emitted. Four clovers were positioned at 90^0 and the other three at 135^0 with respect to the beam line as shown in Figure 8.

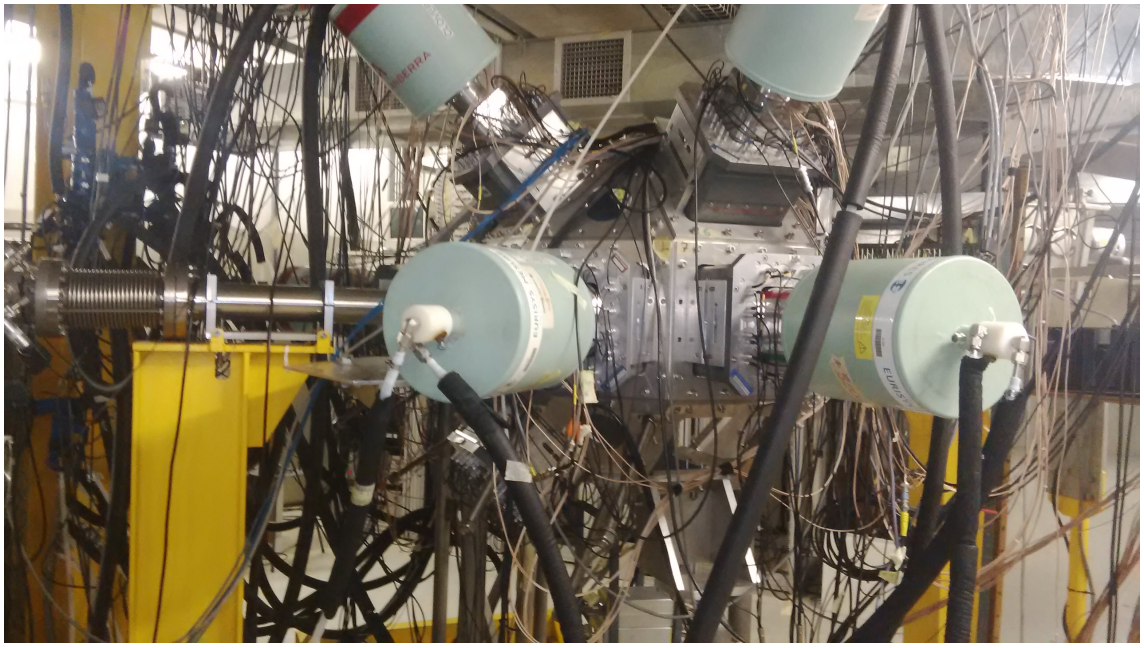

Figure 8: The AFRODITE clover detectors positioned at 90^0 and 135^0 with respect to the beam line.

A germanium γ ray spectrum usually contains Compton continuum events which lead to a decrease in the signal to noise ratio. In order to reduce these events and thus, increase the

signal to noise ratio, the germanium detector has to be surrounded by a high efficiency γ ray scintillator. These scintillation detectors greatly improve the peak-to-total ratio (P/T) of the array by rejecting the scattered radiation from the Ge crystals , meaning that if a γ ray is detected in both scintillation and Ge detector within some defined period of time, then it is not considered as useful data. In the AFRODITE spectrometer, the HPGe crystals are surrounded by the γ ray scintillator called Bismuth Germanate Oxide (BGO), with chemical composition $Bi_4Ge_3O_{12}$. Bismuth's high atomic number and high density make BGO a very efficient γ ray absorber.

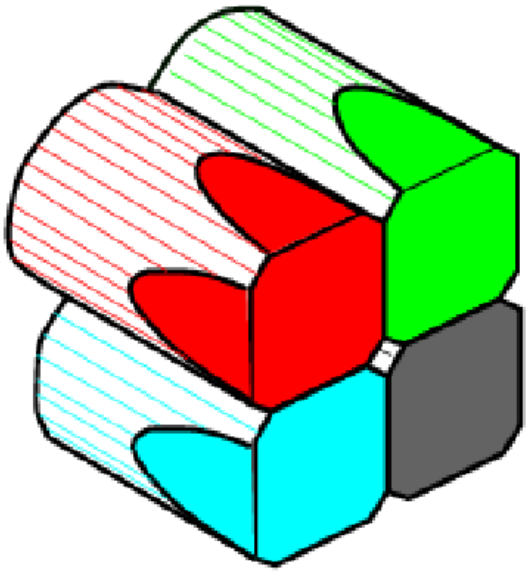

Figure 9: The four-HPGe crystals of the clover detector [33].

3.4 Data analysis method

Before and after the experiment, the data from sources ^{152}Eu and ^{60}Co were collected for efficiency and energy calibration. These sources were placed independently in front of the clover detectors such that all the detectors can detect γ rays emitted by these sources. The data collected before the experiment is used to obtain gain coefficients that are used for energy calibration. These gain coefficients are for making sure that the energy peaks are at rightful energies. The RadWare ENCAL and EFFIT programs [34, 35] were used to determine the energy and efficiency calibration, respectively. The ENCAL program fits an energy calibration to each detector in the form,

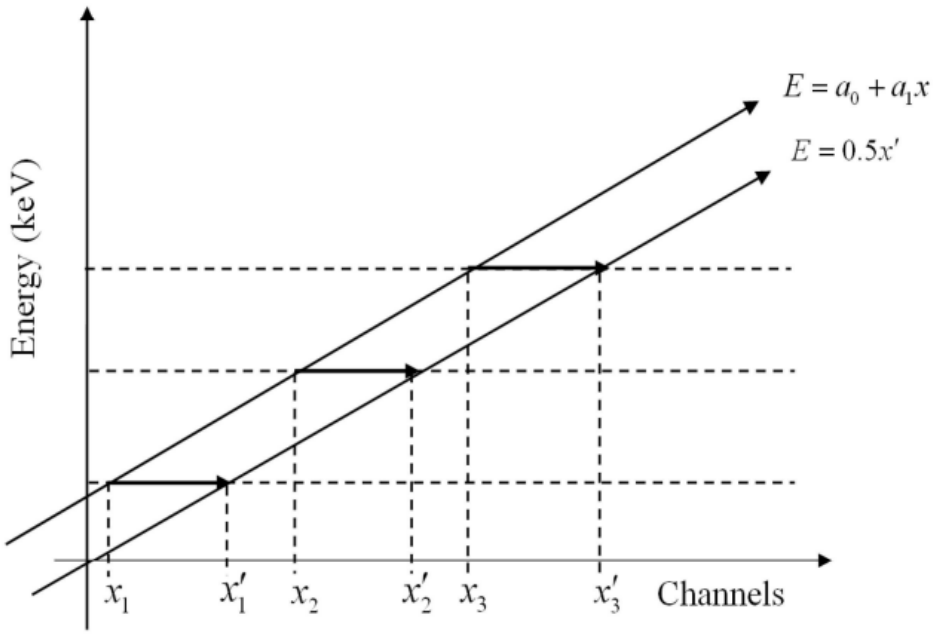

Figure 10: A diagram showing how the energy calibration was performed [4].

$$E = a_0 + a_1 x + a_2 x^2 \tag{5}$$

where x is the channel number. The channels are mapped to calibration of $E = 0.5x'$, where x' are new channels as shown in Figure 10. Figure 11 shows a fit to the efficiency calibration of a Ge detector, obtained using the ^{152}Eu source. In this figure, it is observed that the maximum detection efficiency for clover detectors occurs at 150 keV and the detection efficiency decreases as the energy increases.

During the fusion-evaporation experiment, the data acquired is stored on a hard-disk, ready for the analysis. But, before the analysis can be carried out, the data has to be sorted. In the present work, the data has been sorted using the software-package MIDAS MTsort. The gain coefficients obtained from the data collected before the experiment, are also used to sort the in-beam data. After sorting the data, we obtain the spectra, and then assess if the energy peaks are at their rightful energies. If the energy peaks are not at their rightful energies, the new gain coefficients are calculated and the data is sorted again. Matrices are obtained after sorting the data and are converted to RadWare matrix formats (.mat or .m4b). These matrices store energies of γ rays detected by clover

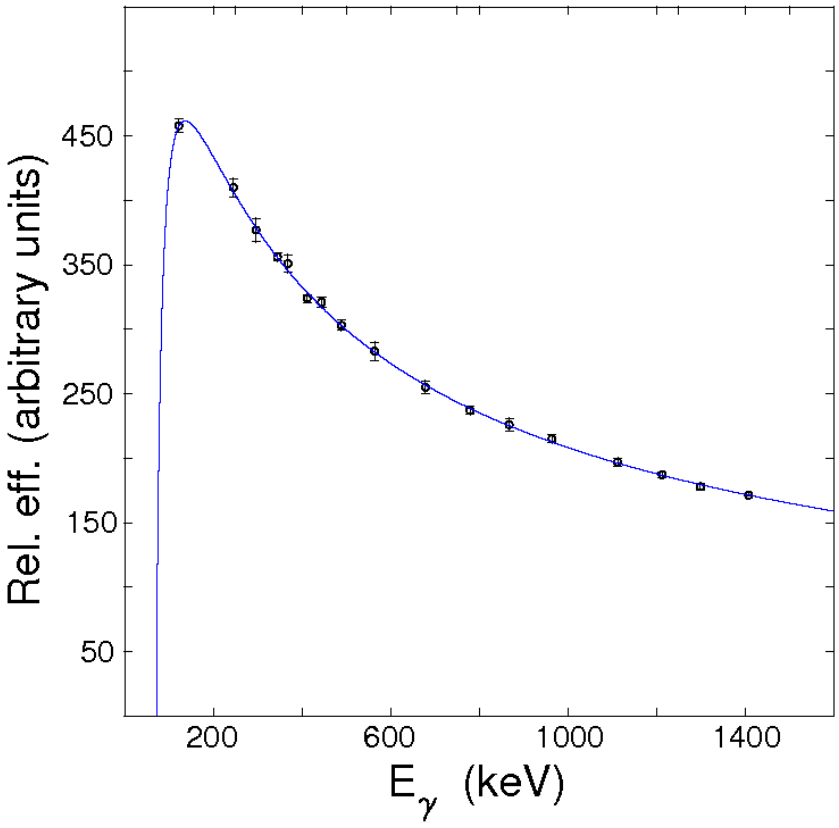

Figure 11: Relative efficiency curve for AFRODITE detectors, obtained using a ^{152}Eu source.

detectors and are used to build the level scheme.

3.5 Nuclear Decay

Nuclear decay is the process whereby an unstable atomic nucleus loses energy by emitting radiation. There are three major types of nuclear decay, namely alpha (α), beta (β) and gamma (γ) decay.

In α decay, a nucleus emits a particle containing two protons and two neutrons (α particle), the nucleus changes into another nucleus with four less particles normally called the daughter nucleus. In β decay, one of the protons in a nucleus is transformed into a neutron and a positron is emitted (β^+ decay) or one of the neutrons is transformed into a proton and an electron is emitted (β^- decay). In this type of decay, the nucleus also changes into a daughter nucleus with one less neutron or proton. Contrary to α and

β decays, when the nucleus decays through γ decay, a nucleus remains unchanged; the same nucleus de-excites from some excited state to the ground state or lower excited state.

When a nucleus decays through α and β processes, usually the daughter nucleus is created in an excited state and then decays to lower states by emitting photons (γ rays). Figure 12 shows a nucleus ^{60}Co which decays to the excited ^{60}Ni (daughter nucleus), then the daughter nucleus decays to the ground state through the emission of two γ rays.

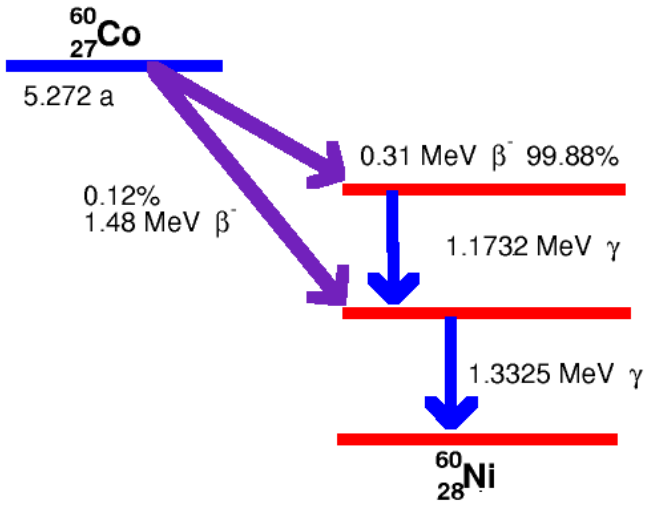

Figure 12: Diagram showing the nucleus ^{60}Co decaying to the excited nucleus ^{60}Ni by β^- decay, then the nucleus ^{60}Ni decays to the ground state by emitting two γ rays.

The three basic nuclear properties (excitation energy, spin and parity) of an excited nuclear state can be measured using conservation laws and electromagnetic selection rules. For a γ transition between states of initial spin I_i^π and final spin I_f^π , the γ ray selection rules are that the decay can proceed by a photon of multipole order L where,

$$|I_i - I_f| \leq L \leq I_i + I_f \tag{6}$$

The general rule is that the transition having the lowest multipole order L dominates the decays. The electric and magnetic nature of γ transitions is decided by the parity conservation law, which is given by,

$$\pi_i = \pi_f \pi_L \tag{7}$$

The parity of an electric transition of multipole order L is given by $(-1)^L$, this implies that the parity is positive for even multipole order L and negative for odd multipole order L. On the other hand, the parity of a magnetic transition of multipole order L is given by $(-1)^{L+1}$, here, contrary to the electric transition, the parity is positive for odd values of L and negative for even values of L. In Figure 13, it can be seen that for electric transitions there is no parity change (the parity in initial state is the same as the parity in final state) if L is even, whereas in a magnetic transition there is no parity change if L is odd.

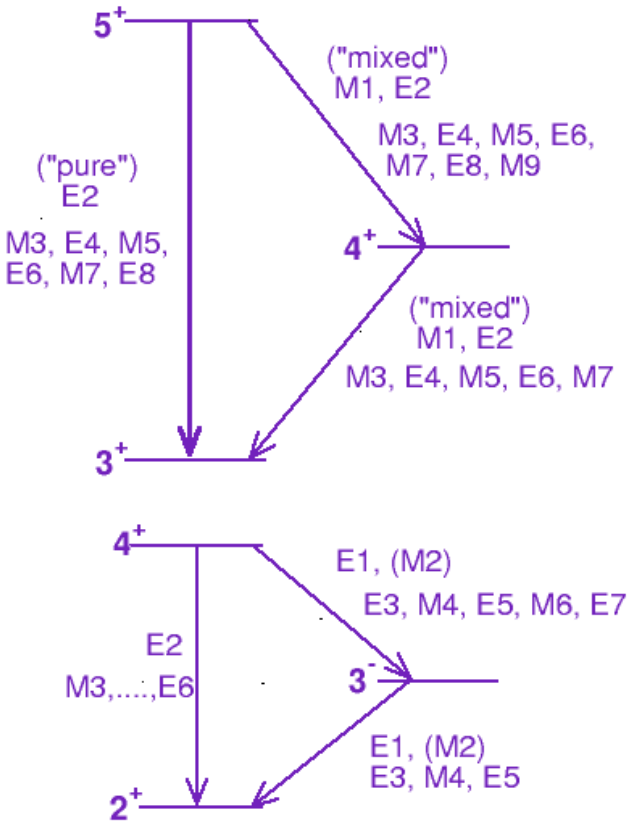

Figure 13: Schematic decay scheme showing how the γ ray selection rule works.

3.6 DCO and Linear Polarization Measurements

In an excited nucleus, the nuclear transitions between excited states can be manifested through the emission of γ rays. These transitions can be classified by their multipolarity, i.e. electric or magnetic (see section 3.5). In a fusion-evaporation reaction, the multipolarity of γ transitions, and relative spins and parities of the levels can be determined using Directional Correlations of γ rays from Oriented states of nuclei (DCO) and linear polarization.

3.6.1 DCO ratios

In order to determine whether the γ ray transition is a dipole or quadrupole, one needs to measure the DCO ratios. For the DCO ratios, the coincidence data are sorted into an asymmetric matrix whose one axis correspond to γ ray energy deposited in the detectors positioned at θ_1, the other axis correspond to γ ray energy deposited in the detectors at θ_2. A gate corresponding to a γ ray of known multipolarity is made on one of these axes and the coincidence spectrum is projected on the other axis. The same gate can be made on different axis, such that a resulting coincidence spectrum is projected on the other axis. From these coincidence spectra, the intensities of the γ ray transitions can be obtained. Thus, one can define the DCO ratio (R_{DCO}) for the γ transitions as:

$$R_{DCO} = \frac{I^{\theta_2}_{\gamma_1}(Gated^{\theta_1}_{\gamma_2})}{I^{\theta_1}_{\gamma_1}(Gated^{\theta_2}_{\gamma_2})} \tag{8}$$

where the term, $I^{\theta_2}_{\gamma_1}(Gated^{\theta_1}_{\gamma_2})$, represents the intensity of γ_1 detected at an angle, θ_2, gated with γ_2 at θ_1 with the respect to the beam direction. The term, $I^{\theta_1}_{\gamma_1}(Gated^{\theta_2}_{\gamma_2})$, denotes the intensity of γ_1 detected at θ_1, gated with γ_2 at θ_2. In the AFRODITE array, the angles, θ_1 and θ_2 are 135^0 and 90^0 respectively. When measuring DCO ratios, one has to be careful when making a gate, as gates made on transitions with different multipolarities (i.e. dipole or quadrupole) give different results. For instance, when gates are set on quadrupole transitions, the R_{DCO} values for dipole and quadrupole transitions are respectively ~ 0.5 and ~ 1. However, a gate made on dipole transitions gives ~ 1.1 and ~ 1.7 R_{DCO} values for dipole and quadrupole transitions respectively.

3.6.2 Linear polarization

As mentioned above, the DCO ratios can only give information about the multipolarity of the transition. In other words, the information given by R_{DCO} is necessary but not sufficient for accurate assignment of a γ ray's electromagnetic nature. When assigning spin and parity, one needs to know whether the γ ray transition is electric or magnetic.

The linear polarization helps to distinguish the electric and magnetic nature of the γ ray transition. A polarization matrix is constructed from the data corresponding to the energy detected in any detector on one axis, while the other axis corresponds to energy scattered in a perpendicular or parallel segment of the clover detector with respect to the beam direction. From the projected spectra, the number of perpendicular and parallel scatters for a given γ ray energy can be obtained. The polarization anisotropy P, is defined as:

$$P = \frac{A_P}{Q} \tag{9}$$

P is determined on the basis of the experimental asymmetry between horizontally (parallel) and vertically (perpendicular) scattered γ rays. In this equation, the numerator A_p is given by equation 10 [36] and Q is the polarization sensitivity for clover detectors [37].

$$A_P = \frac{aN_V - N_H}{aN_V + N_H} \tag{10}$$

Where N_V and N_H are the number of γ rays scattered perpendicular and parallel to the beam direction respectively, and a is the relative efficiency parameter. This parameter is determined using the unpolarized γ-rays and is defined as:

$$a = \frac{N_H}{N_V} \tag{11}$$

The uncertainty in the measured A_P, is calculated using equation 12,

$$\Delta A_P = \frac{2}{(N_V + N_H)^2}\sqrt{(N_H\sigma_V)^2 + (N_V\sigma_H)} \tag{12}$$

where σ_V and σ_H are the uncertainities on the number of γ rays scattered vertically and horizontally at at 90^0 with respect to the bea line, respectively.

A positive value for A_P, indicates a pure electric transition, as this transition prefers to scatter in the perpendicular direction with the respect to the beam axis; while a negative

value for A_P, indicates a pure magnetic transition due to its preferential scattering along the parallel direction.

4 Experimental Results

4.1 The total projection

The detailed spectroscopy of ^{162}Yb has been studied. The full projection spectrum of ^{162}Yb is shown in Figure 14. It consists of a total of 7.4×10^9 $\gamma\gamma$ coincidences. This projection was used to build the level scheme of ^{162}Yb, shown in Figure 15. This level scheme shows almost all the γ ray transitions that were observed in the previous study [10] but with an addition of 40 new transitions, and was built using the data from our experiment.

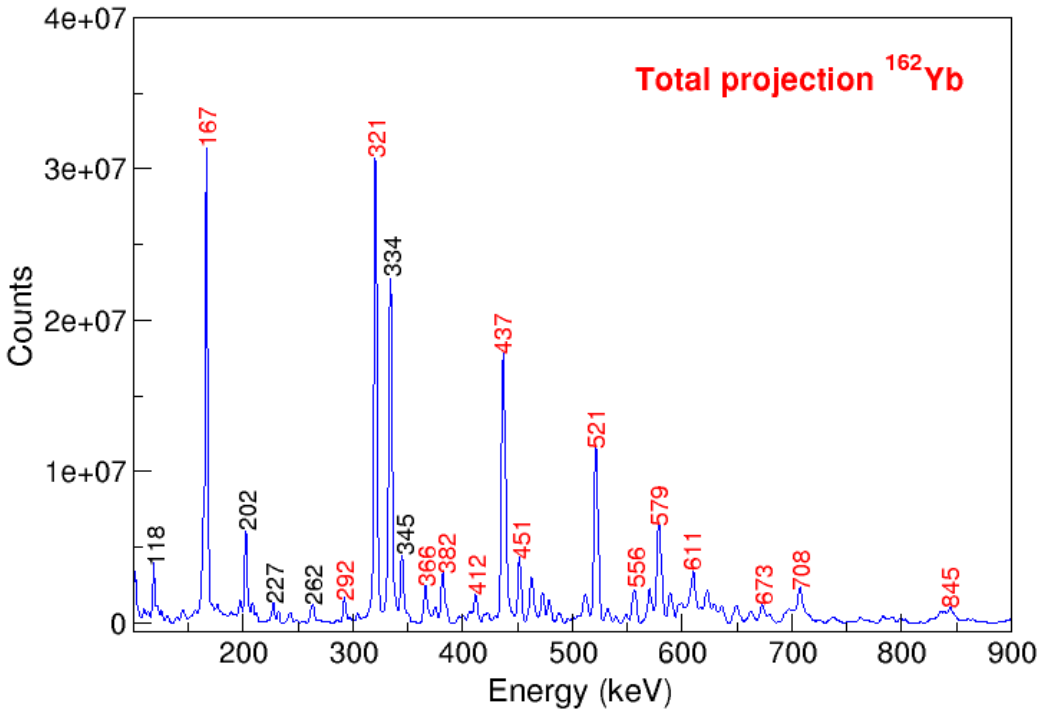

Figure 14: The full projection spectrum of the nucleus ^{162}Yb showing the strongest γ ray transitions that were populated in the experiment. Transitions belonging to other nuclei are indicated by black labels.

4.1.1 Contaminants

As can be seen in Figure 14, the projection spectrum of the nucleus of interest has some γ rays that do not belong to ^{162}Yb (contaminants). The contaminants that were strongly populated in the experiment are Yb isotopes. These isotopes were populated as a result of different number of neutrons emitted as the compound nucleus was cooling off to the ground state during the experiment. The nucleus ^{163}Yb was amongst the most predominantly populated contaminants in the experiment, and we observed almost all the bands that have been previously reported in this nucleus. The present work, further observes the extended ground-state band of ^{163}Yb, that has been extended by Sithole [38]. In fusion-evaporation reactions, the product nuclei are proton rich and usually decay by β^+ and electron capture decay [39]. Thus, transitions resulting from this β decay were also observed. We have built the level schemes for all contaminants that we have accounted for in this current work.

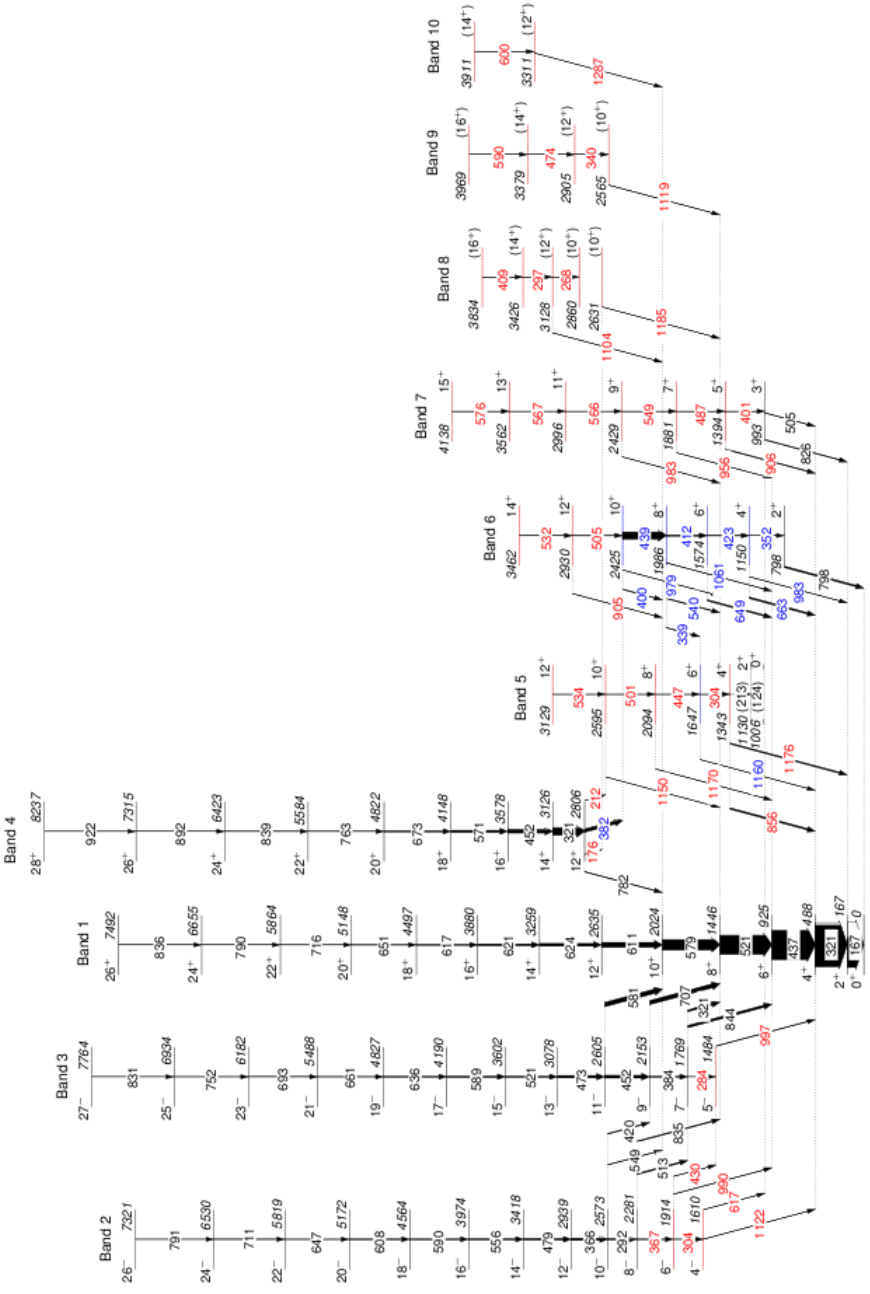

Figure 15: The level scheme of ^{162}Yb showing the γ transitions observed in this experiment. Transitions and energy levels that were previously observed are colored in black and newly observed transitions and levels are colored in red. Transitions and energy levels that were previously placed in different bands are highlighted in blue. Tentative γ ray energies, spins and parities are given within parentheses. The widths of the arrows are proportional to the transition intensities.

4.2 DCO and Linear Polarization

The DCO and polarization measurements were performed for almost all γ ray energies that were previously reported. Some of these γ ray transitions were weakly populated in the current work, and consequently we could not measure their DCO and polarization values.

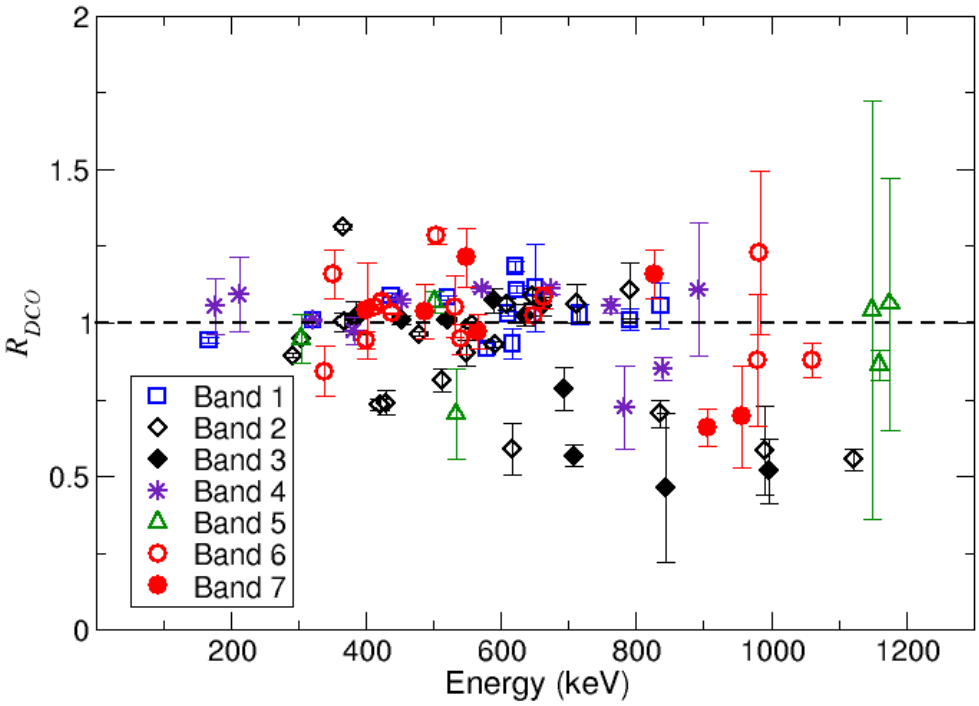

Figure 16: Plot for the measured DCO ratios (R_{DCO}).

The measurements were also performed for the newly observed transitions and were found to be consistent with $E1$, $M1$, and $E2$ characters. All the measured DCO and polarization values for the γ ray energies observed in the present work, together with their multipolarities are presented in the appendix. In Figure 16, we show the plot for the measured DCO ratios. It can be seen that most of the measured DCO ratios lie close to one (dotted-line), indicating a quadrupole character. DCO ratios that lie close to 0.5 are dipole transitions. Figure 17 shows the plot for the measured polarization values. In this figure, most of the polarization values lie above zero, which indicate an electric

transition. A very few values lie below zero, these values indicate magnetic transitions.

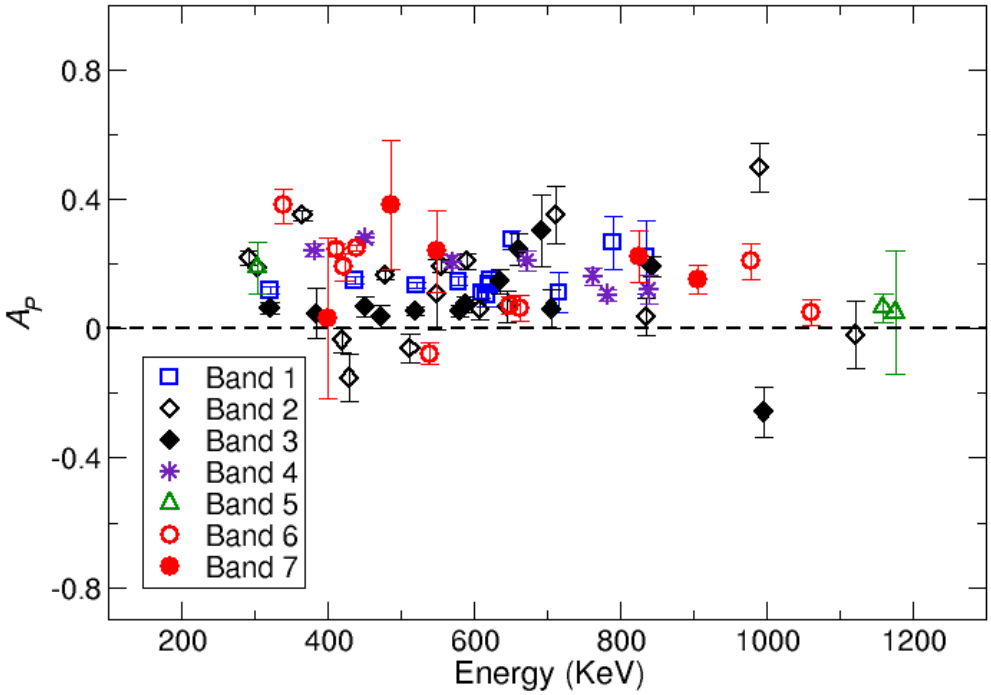

Figure 17: Plot for the measured polarization anisotropy (A_P).

4.3 Band 1 (Ground-state band)

In the present work, the ground-state band has been observed up to spin 26^+. The previous experiment [10] observed this band up to spin 28^+. The spectrum showing all the ground-state members populated in this current work is shown in Figure 18. DCO ratios and polarization measurements for the populated γ transitions were performed, and the measured transitions are consistent with the stretched $E2$ character. DCO and polarization measurements for these transitions are shown in the Appendix, on page 74 .

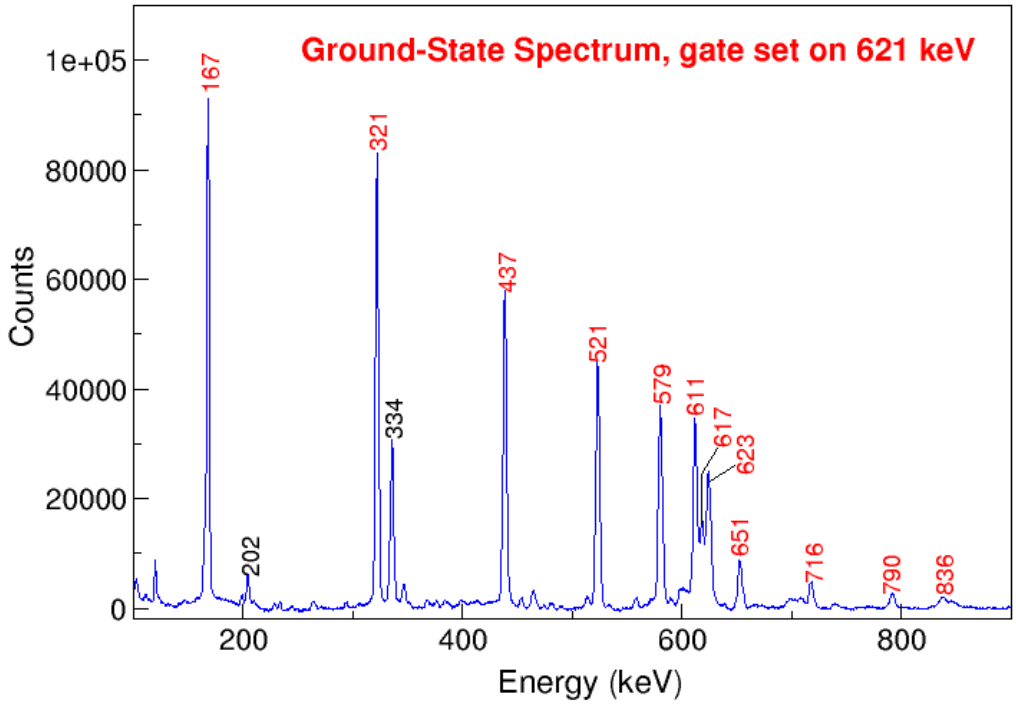

Figure 18: The ground-state spectrum obtained by setting the gate on 621 keV, showing all the ground-state members that were populated in the experiment (colored in red) and some few contaminants (colored in black).

4.4 Band 2

We observed band 2 up to spin 26^- with two additional levels at lower spin. The previous experiment [10] observed this band up to spin 36^-. In the present work we could not

populate this band to such high spins, but we managed to extend it at low spin with two levels (spin), namely 1914 (6^-) and 1610 (4^-) keV with the transitions, 367 and 304 keV, respectively.

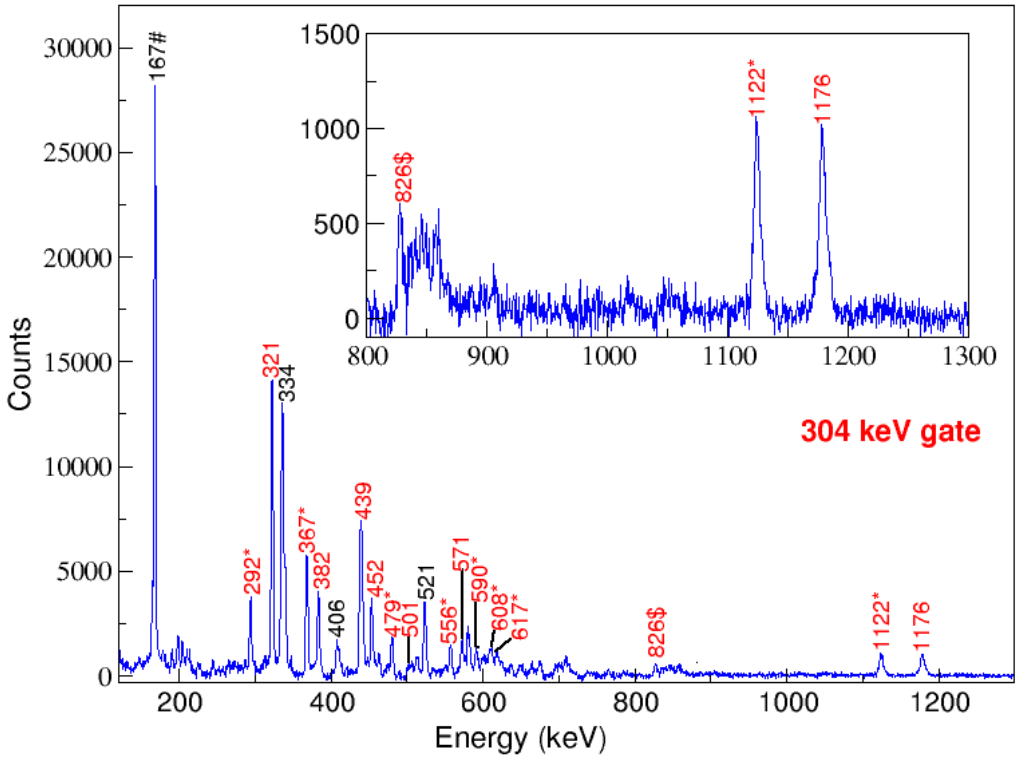

Figure 19: The spectrum obtained by setting a gate on the transition at 304 keV. The γ rays that are in coincidence with this transition are members of bands 4, 5, and 6 (colored in red). Members of band 2 are colored in red with an asterisk (*)) while those of band 7 are marked by a dollar sign ($). The ground-state member in coincidence with 304 keV, is marked by a hash (#). The other transitions, colored in black, are contaminants. Insert figure shows only the high-energy part of the same gate.

The γ transition, 304 keV, is of particular interest as it sees both γ rays in negative-parity and positive-parity bands which are not connected by any transition. Shown in Figure 19 is the spectrum obtained by setting a gate on this transition. In this figure, it can be seen that both members of the negative-parity band (band 2) and the positive-parity bands (bands 4, 5 and 6) are in coincidence with 304 keV, including the two γ transitions at higher energies, namely the 1122 and 1176 keV transitions.

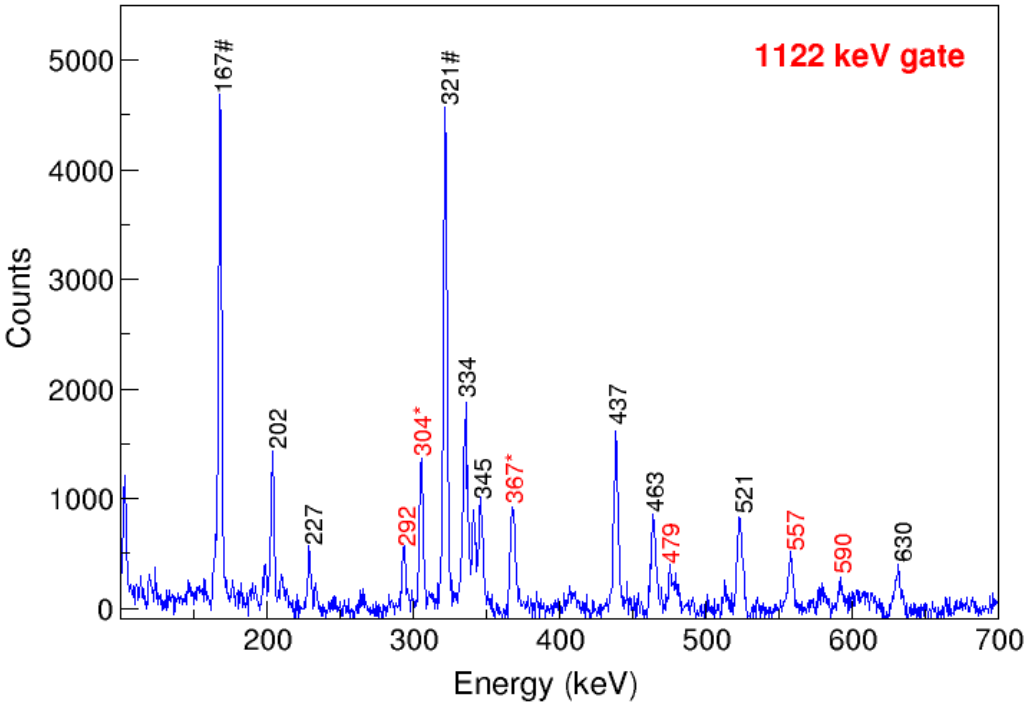

Figure 20: The spectrum showing the γ rays that are in coincidence with 1122 keV (colored in red), which are the members of band 2. These transitions include the two newly observed γ rays (marked by a symbol (*)). Transitions marked by a hash, are ground-state members in coincidence with 1122 keV. The transitions colored in black are contaminants from other reaction channels and / or other bands of ^{162}Yb , not associated with band 2.

When the gate is set on the 1122 keV transition (see Figure 20), the coincidence spectrum shows only the members of band 2, including the two newly observed γ ray energies (304 keV and 367 keV).

However, setting a gate on the 1176 keV transition, the coincidence spectrum shows the γ rays associated with positive-parity bands and the newly observed transition 304 keV (see Figure 21). Thus, the 1122 keV transition is in coincidence with γ rays belonging to band 2 and the 1176 keV transition is in coincidence with the γ rays associated with the positive-parity bands.

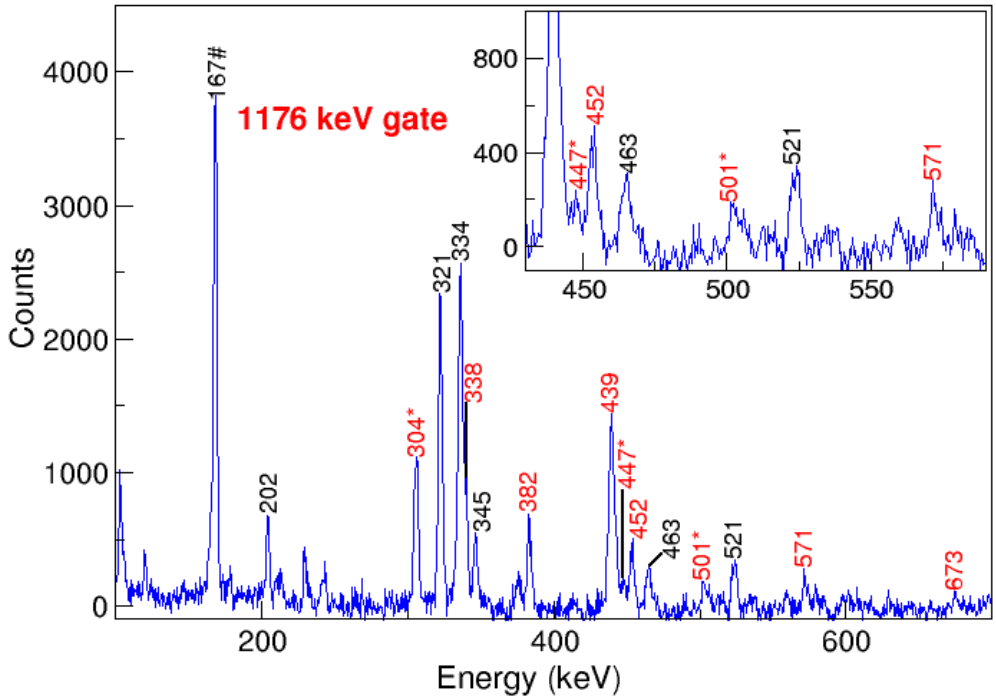

Figure 21: Shows the γ transitions that are in coincidence with 1176 keV (colored in red) and these are the γ rays associate with positive-parity bands 4, 5 and 6. The transitions marked by an asterisk, are newly established members of band 5. Insert figure shows the spectrum of the same gate, but only showing the energy part from 430 to 600 keV. The ground-state member in coincidence with 1176 keV (marked by hash) and contaminants are colored in black.

As shown in Figures 20 and 21, the 304 keV is the only γ ray, among all the γ transitions highlighted in red, that appears in both 1122 and 1176 keV gates. The appearance of this transition in both gates and being in coincidence with γ rays in different bands, suggests that the 304 keV is a doublet.

The newly observed transition, 367 keV, depopulates a level at 1914 keV. The 430 and 990 keV transitions also decaying out of this level populate band 3 and the ground-state band (see Figure 22), respectively. The DCO and polarization measurements for some of the newly observed transitions were performed. The measurements for 304 and 367

keV were found to be consistent with the $E2$ character. We have also measured the DCO and polarization for the transitions that were reported in the previous experiments. Most in-band members of band 2, measured in this current work, are consistent with $E2$ character.

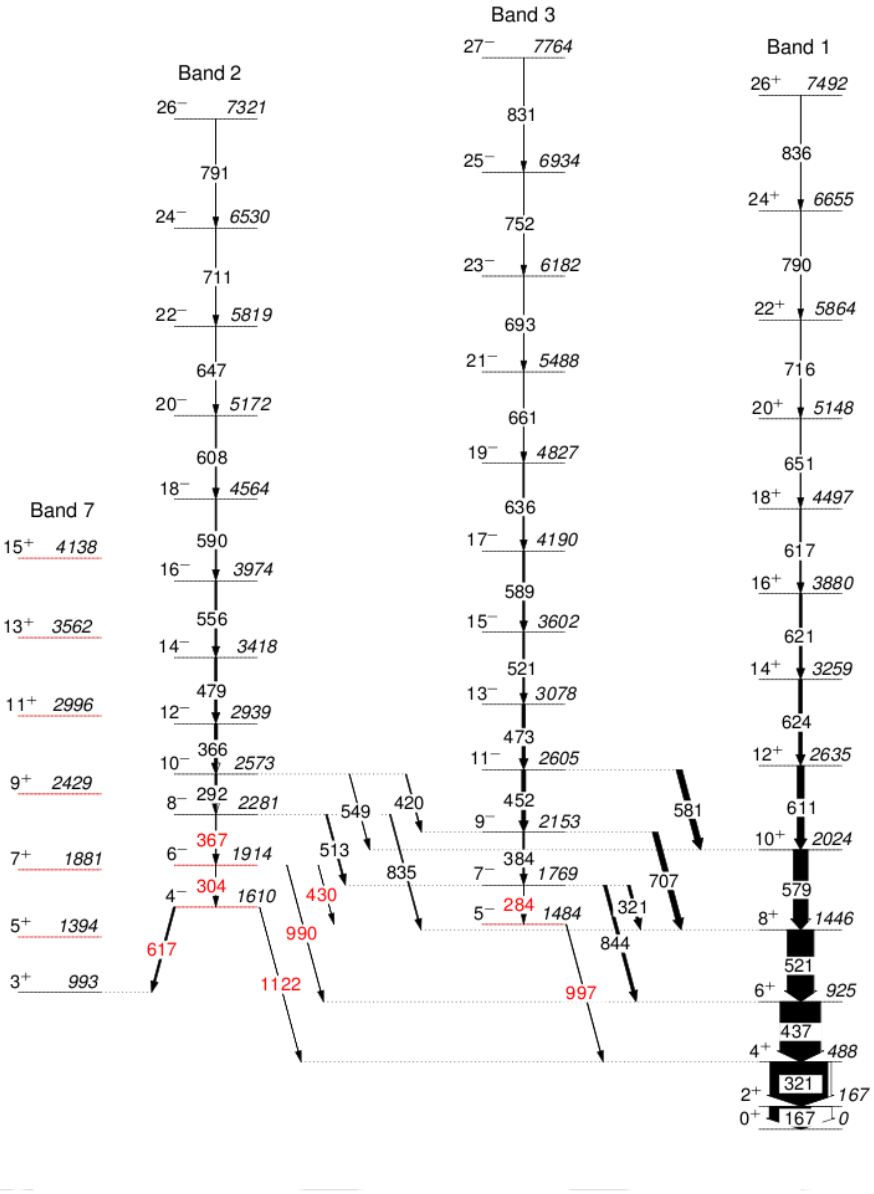

Figure 22: Partial level scheme of ^{162}Yb showing the γ transitions for the negative parity bands together with band 7 levels, connected by 617 keV with band 2. Transitions and energy levels that were previously observed are colored in black and newly observed transitions and levels are colored in red.

4.5 Band 3

The previous experiment [10] observed band 3 up to spin 37^-. The present experiment only observes band 3 up to spin 27^- with one more additional level at the lower spin. It is believed that this newly added level, at 1484 keV, belongs to band 3. The evidence for this level is based on the two transitions, namely the 430 keV and 997 keV, decaying into and out of this level, respectively.

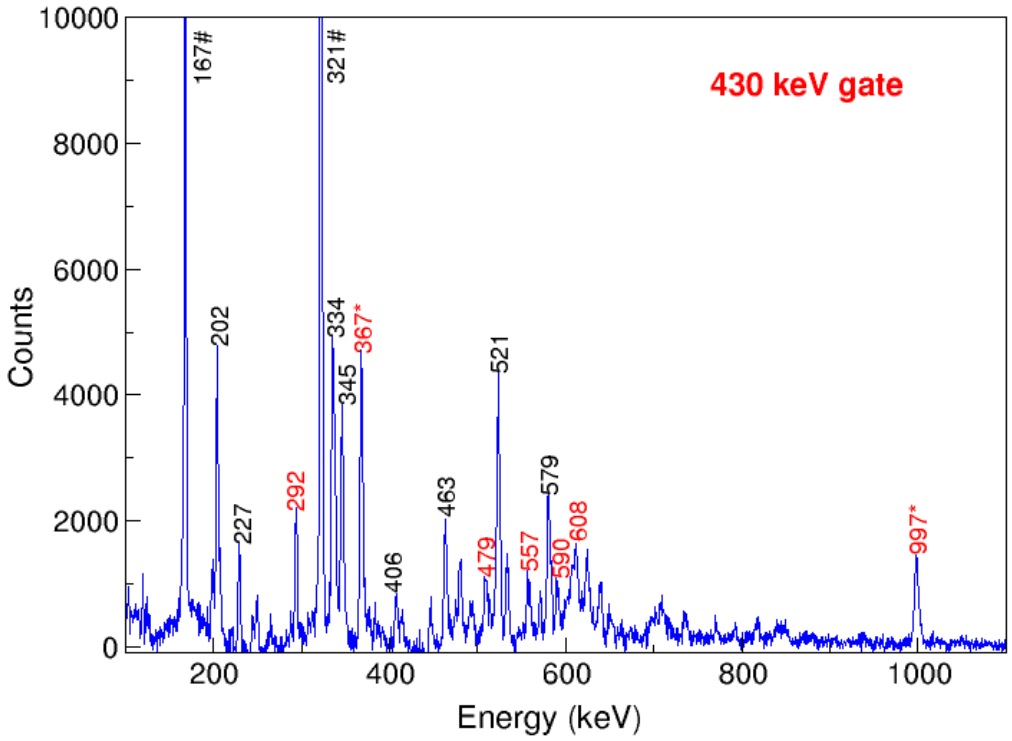

Figure 23: A gated spectrum (on 430 keV) confirming the newly observed 367 keV and 997 keV transitions (denoted by asterisks). The transitions that are in coincidence with the 430 keV transition are highlighted in red, including ground-state members marked by a hash sign. The other transitions, colored in black, are contaminants and transitions that are not in coincidence with 430 keV.

The DCO and polarization measurements for these transitions were performed. the DCO measurements, for both transitions, are consistent with a dipole character. On one hand,

the polarization measurement for the 430 keV γ ray is consistent with a dipole magnetic transition. On the other hand, the polarization measurement for 997 keV γ ray is consistent being an electric dipole transition. The gates made on these two transitions are shown in Figures 23 and 24. These figures confirm that both the 430 and 997 keV transitions are in the same decay path with in-band members of band 2. However, it is worth noting that the 997 keV transition is not clearly visible when a gate is set upon the 284 keV transition, see Figure 24. We believe that the reason for this is that the 284 keV transition, which is the γ transition from the level at 1769 keV to the newly added level at 1484 keV, is very weakly populated. However, a gate at 284 keV does show a very weak 997 keV γ ray, as shown in the insert of Figure 24.

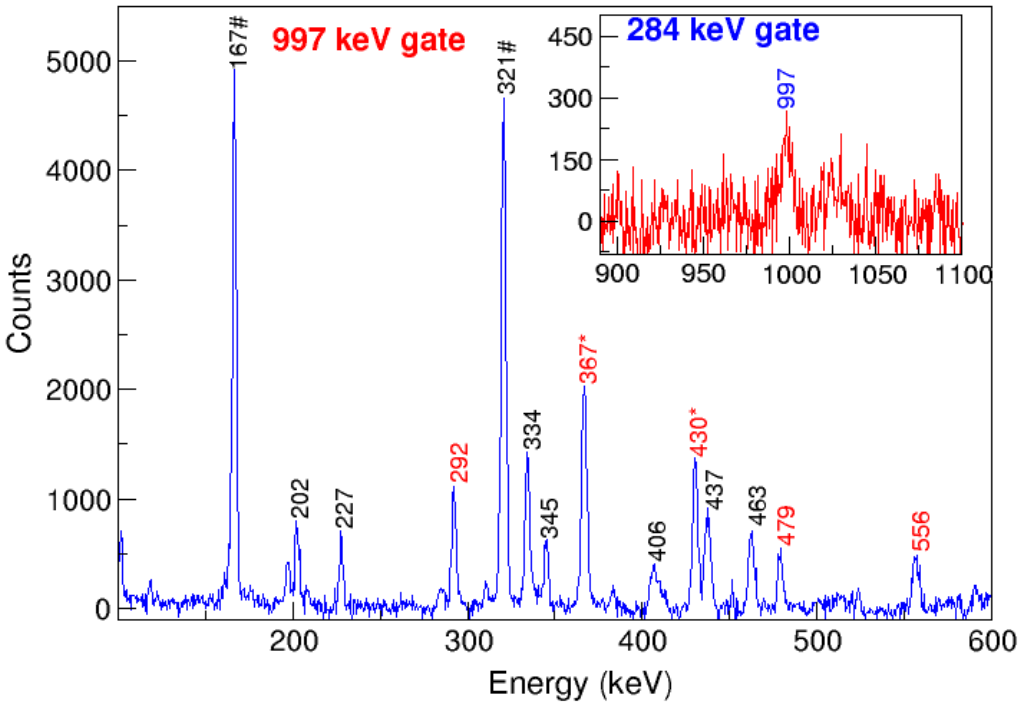

Figure 24: The spectrum showing the newly observed transitions (marked by an asterisk). This spectrum was obtained by setting a gate on the 997 keV transition. The γ ray energies colored in red, are band 2 members and are in coincidence with the 430 keV transition. The labeling for other transitions is still the same as defined in Figure 23. Insert figure shows the spectrum obtained by setting a gate on the 284 keV transition.

4.6 Band 4 (S-band)

This band is observed in many deformed nuclei and is commonly known as the S-band. When the excitation energy minus the energy of a rigid rotor is plotted against spins; this band usually crosses the ground-state band (see Figure 38).
At around spin 12^+, the ground-state and S-bands interchange the yrast characteristics. As shown in Figure 15, the ground-state band (band 1) is a yrast band from spin 0^+ up to 12^+. The S-band (band 4) becomes the yrast band at spin 14^+ up to the highest spins. The present work observes this band up to spin 28^+ and there is no new level that has been added to this band but there are two newly observed transitions decaying out of the 2806 keV level, see Figure 26. The spectrum showing the newly observed transition (212 keV) is shown in Figure 25.

In this band, there are four depopulating transitions, namely a 782, 382, 176 and 212 keV. All of these transitions are decaying to the different bands (see Figure 26). The 782 and 382 keV transitions have been observed in the previous experiments, while the 212 and 176 keV transitions have been observed in this current work for the first time. All these transitions depopulate the level at 2806 keV, at spin 12^+. The crossing occurs after this spin where the yrast characteristics of the ground-state band are being taken over by the S-band. The 782 keV transition links this band to the ground-state band and the 382 keV transition links the S-band to the even γ band. The newly observed transition, 212 keV, provides a connection between the S-band and the 0_2^+ band. The 176 keV transition decays to the newly observed level at 2631 keV, which is linked by the 1185 keV transition to the ground-state band, see Figure 26. The DCO and polarization measurements for most of these band members were performed and were found to be consistent with the stretched $E2$ character. Due to the low statistics, we could not measure the DCO and polarization for some few transitions in this band.

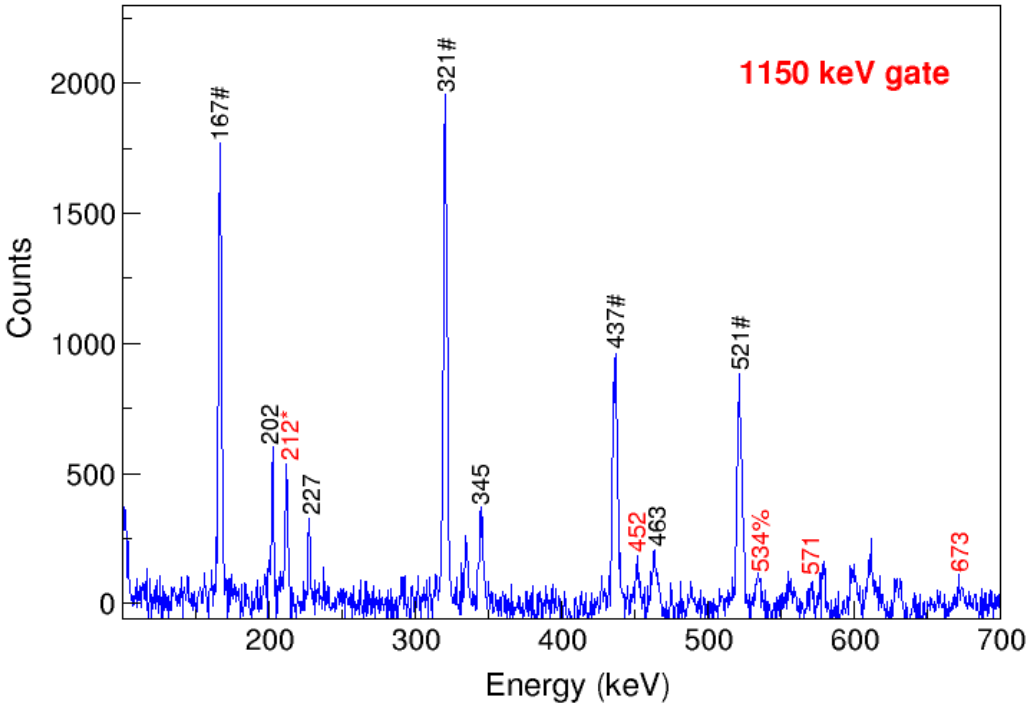

Figure 25: A gated spectrum, confirming the newly observed 212 and 534 keV transitions, marked by an asterisk and a percentage sign (%) respectively. The transitions marked by a hash sign, are the ground-state members in coincidence with 1150 keV transition. The transitions colored in red are S-band members also in coincidence with this transition. The γ ray energies from other reaction channels are colored in black.

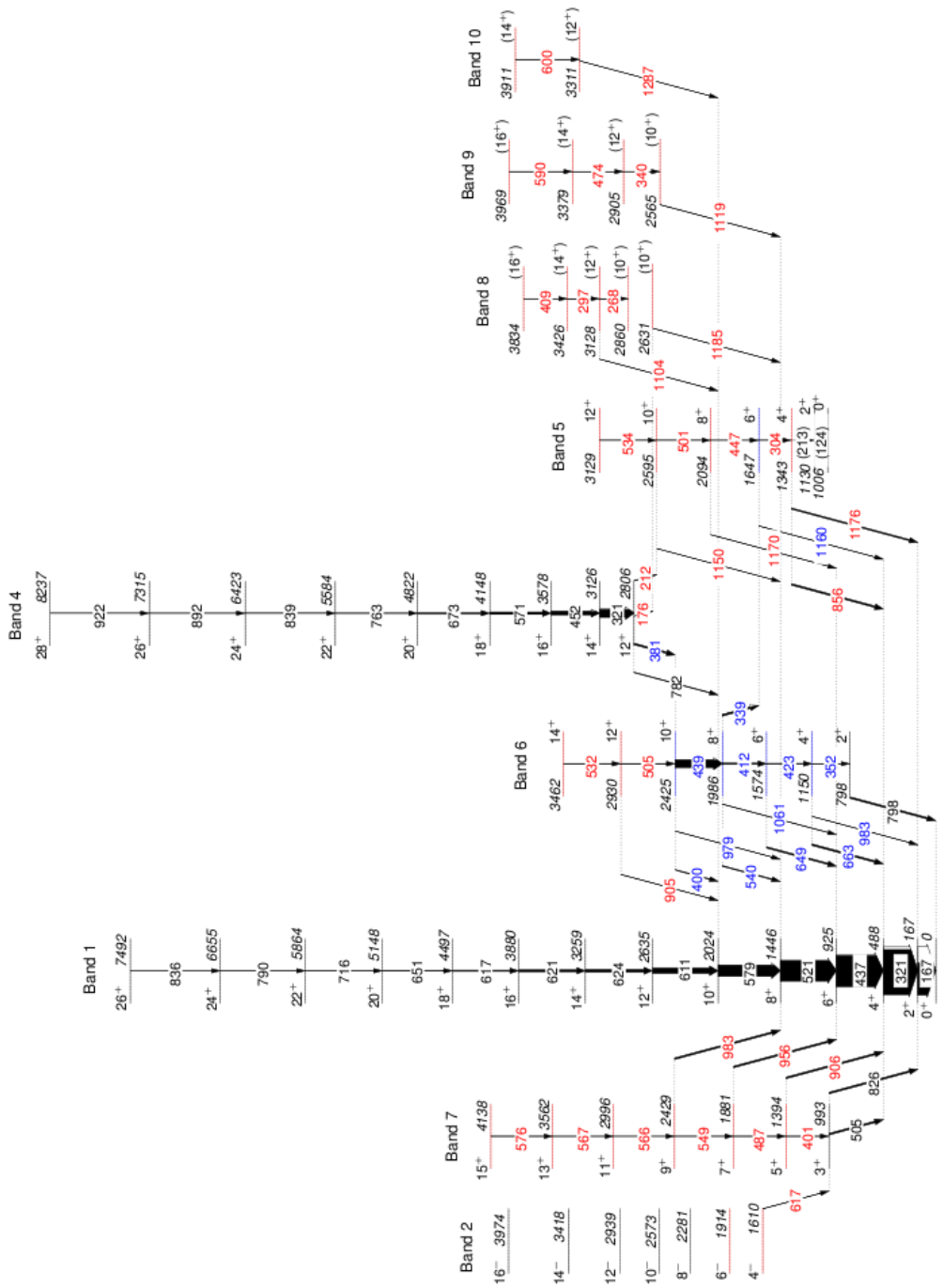

Figure 26: Partial level scheme of ^{162}Yb, showing the positive-parity bands. The newly observed transitions and energy levels are highlighted in red and the previously reported transitions and levels are in black. Transitions and energy levels that were previously placed in different bands are highlighted in blue. Tentative γ ray energies, spins and parities are given within parentheses.

4.7 Band 5 (0_2^+ band)

The present work observes band 5 up to spin 12^+. The four members of this band colored in red are observed for the first time in this current work, Figure 27. These in-band γ rays (304, 447, 501, and 534 keV) are very weakly populated compared to the strong out-of-band transitions decaying out of this band. As a result, when the gate is set on any of them, we are unable to clearly observe all γ-ray energies that are in coincidence.

The first excited level of the 0_2^+ band was first observed by MacCutchan et al [11]. In Figure 27, we show all levels of this band that have been previously reported and the newly observed ones. The 304 keV transition is a doublet and has been discussed in section 4.4. This transition decaying to the 1343 keV level is reported for the first time in this current study. The evidence for this level is based on the 1176 keV transition, which decays to the ground-state band. The spectra confirming the existence of this level are shown in Figures 19 and 21.

The level at 1647 keV, has been observed in previous experiments, the evidence for this level was based on the populating transition 339 keV and depopulating transition 1160 keV. In the present work, we observe a new γ transition, 447 keV from a level at 2094 keV, which is in coincidence with 1160, 1176 and 304 keV transitions (see Figures 28 and 29). However, the transition 339 keV is also in coincidence with the aforementioned transitions (see Figure 30). It is also in coincidence with the members of band 6. This suggests that the 339 keV transition links band 6 with band 5.

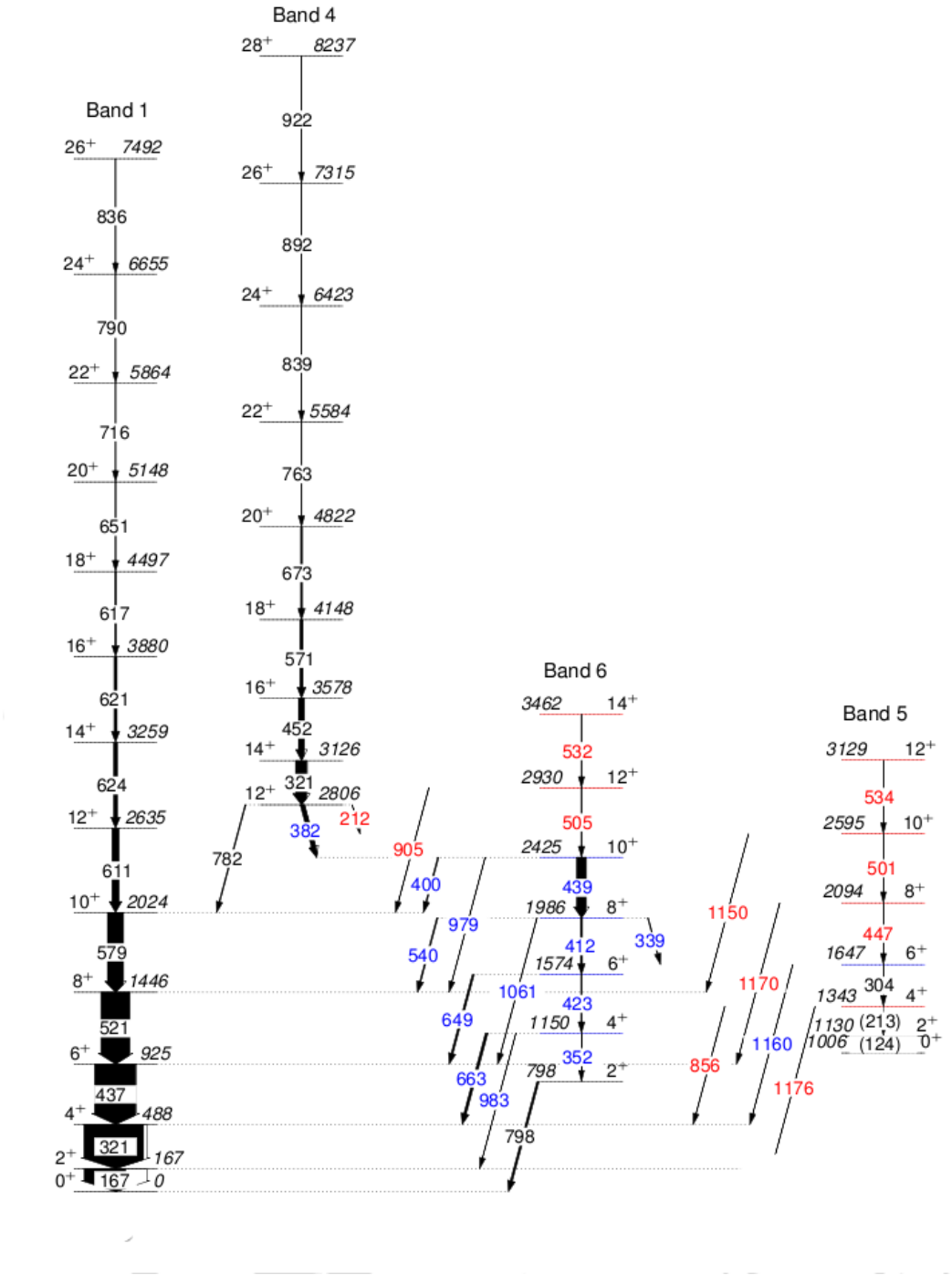

Figure 27: Partial level scheme of ^{162}Yb, showing the ground state, even-γ, 0_2^+ and S-bands. The newly observed transitions and energy levels are highlighted in red and the previously reported transitions and levels are in black. Transitions and energy levels that were previously placed in different bands are highlighted in blue.

From the level at 2094 keV, there is a γ ray transition (1170 keV) that is decaying out of band 5 and feeding the ground-state band. When the gate is set on this transition (see Figure 31), we clearly see the other two members (501 and 534 keV) of band 5 together with the members of band 4 connected by the transition 212 keV. The transition, 501 keV, is from the level at 2595 keV. This level has one populating transition from another band, which links band 5 with band 4. There is also one transition that decays out of band 5 from this level to the ground-state band. The spectrum obtained by setting the gate on this 1150 keV transition is shown in Figure 25. Due to the lack of statistics we could not measure the DCO and polarization for some members of band 5. The transitions that we managed to measure DCO and polarization values for, were found to be consistent with $E2$ character.

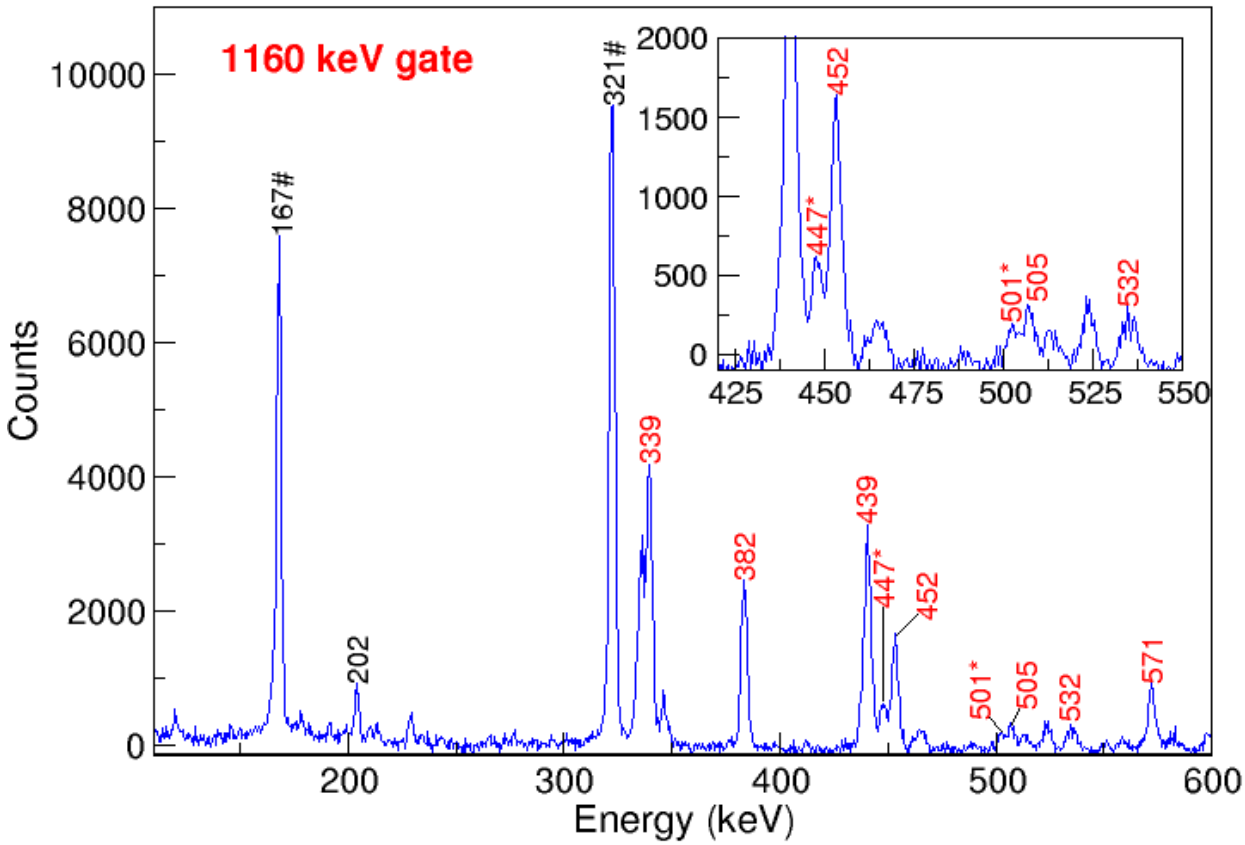

Figure 28: A spectrum obtained by setting a gate at 1160 keV, showing the newly observed members of band 5, marked by asterisks. The γ ray energies colored in red without an asterisks, are bands 4 and 6 members in coincidence with the 1160 keV γ ray, and the ones marked by a hash (#) are band 1 members in coincidence with this transition. The transition in black is a contaminant. Insert figure shows the spectrum of the same gate, from 425 to 550 keV.

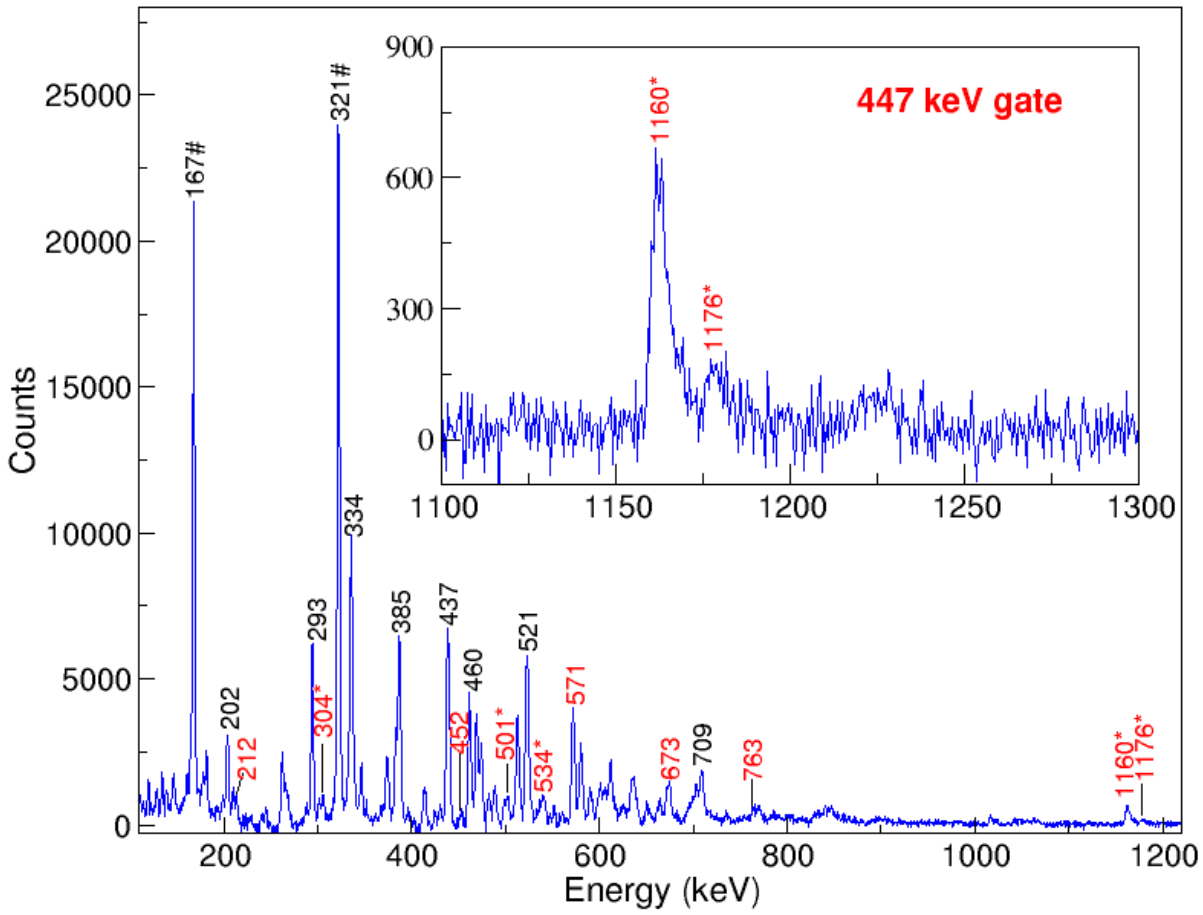

Figure 29: A spectrum obtained by setting a gate on the newly observed 447 keV transition, showing the members of band 5 (marked by asterisks). The γ ray energies marked by hash sign, are band 1 members in coincidence with 447 keV and the transitions highlighted in black are the ones that do not belong to the nucleus of interest or are not associated with band 5. Insert figure shows only the high-energy part of the same gate.

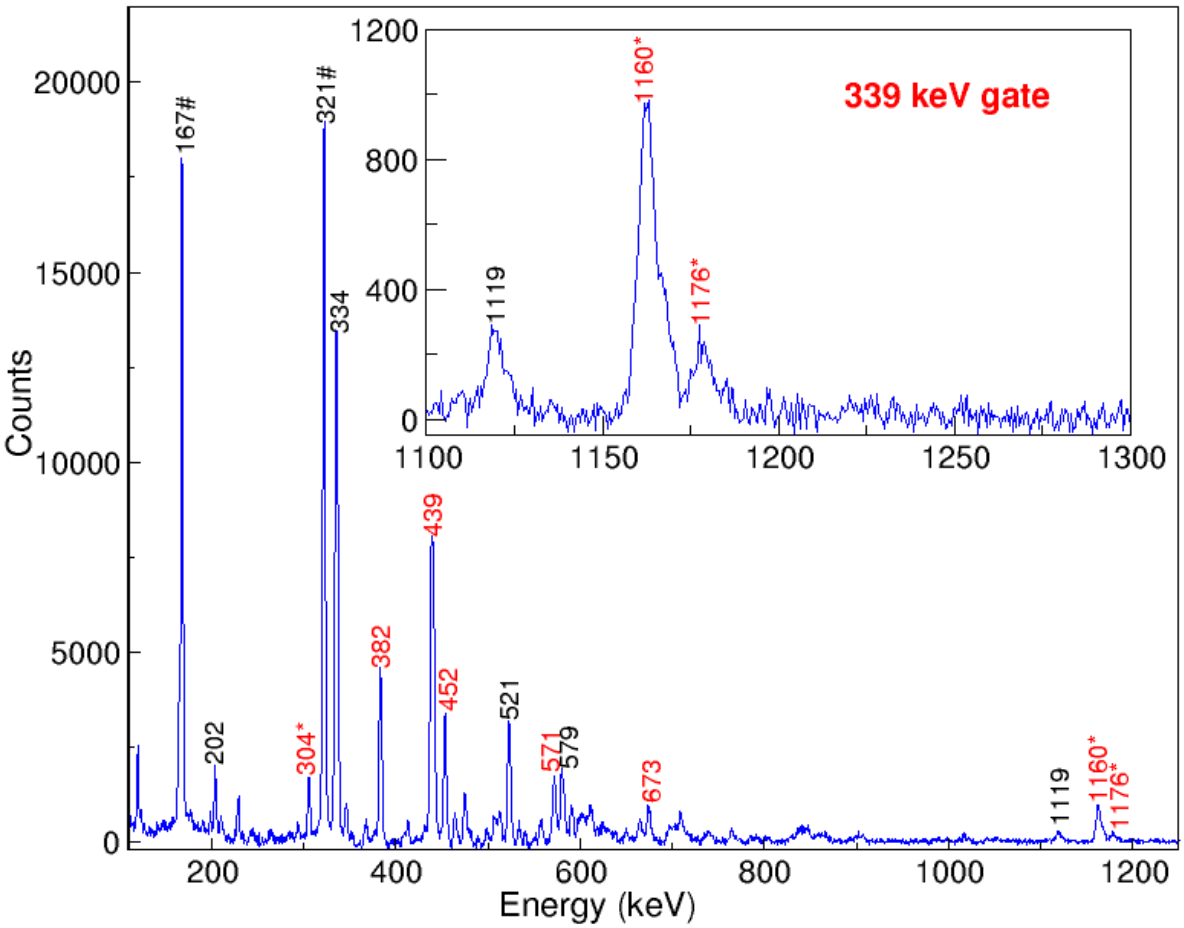

Figure 30: A gated spectrum showing members of band 5 that are in coincidence with the 339 keV γ ray (marked by an asterisks). The labeling for the other γ ray energies is still the same as defined in Figure 29. The high-energy part of this gate is clearly shown in the insert figure.

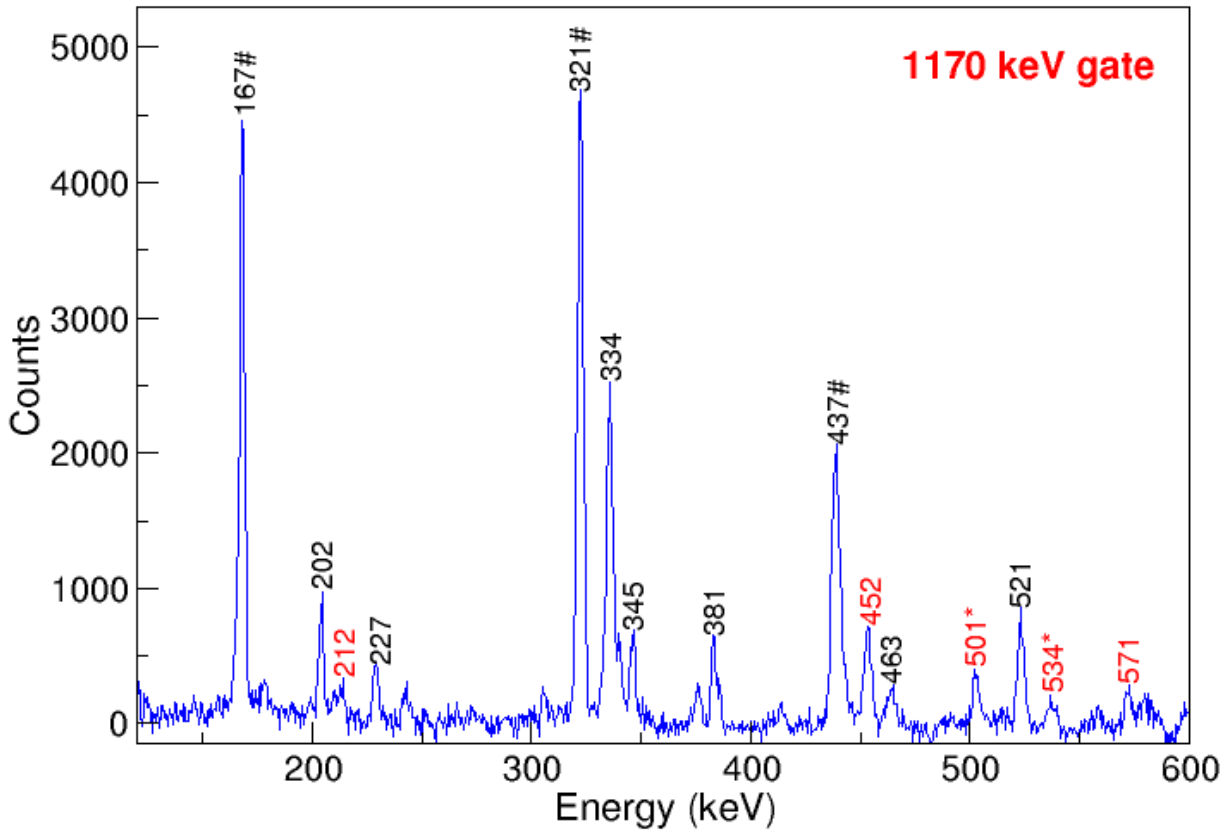

Figure 31: A spectrum obtained by setting a gate at 1170 keV. Transitions that are colored in red (without an asterisks) are band 4 members, while transitions marked with an asterisks, are band 5 members. The labeling for the other γ-ray energies is still the same as defined in Figure 29.

4.8 Band 6 (Even-γ band)

The first excited 2^+ level of band 6 has been reported in the previous experiment [11], at 798 keV. This is the only level, for band 6, that has been firmly established in ^{162}Yb. The evidence for this level was based on the two depopulating transitions, a 798 keV and 632 keV feeding the ground-state band and one populating transition (194 keV) from the odd-γ level at 992 keV. However, in this current study, the 632 keV and 194 keV

transitions could not be observed. On the other hand, the 798 keV transition is weakly observed. This is because the statistics of the present coincidence data were not enough to clearly observe these transitions.

In the present work, it has been suggested that the 1150, 1574, 1986 and 2425 keV levels seen by Mo et al [10], are the 4^+, 6^+, 8^+ and 10^+ members of the even γ band. This suggestion is based on the populating transition 352 keV, which decays from the level 1150 keV to the even-γ band level at 798 keV. In addition, the plot of excitation energy minus the energy of a rigid rotor as a function of spin agrees with this suggestion, as the behavior of this band tracks the ground-state band (see Figure 38).
This band has been extended by two more transitions, a 505 and 532 keV at the levels 2930 and 3462 keV, respectively. At the 2930 keV level, there is also a newly observed 905 keV transition, which decays out of this band to the ground-state band level, at 2024 keV. The partial level scheme of ^{162}Yb showing this band and other positive-parity bands is shown in Figure 27. In this figure, it is worth noting that the majority of the levels were previously not assigned as band members of the even-γ band.

4.9 Band 7 (Odd-γ band)

The previous study [10] observed only one member of the odd γ band level, a 3^+ level at at 993 keV. This level was identified on the basis of three transitions, namely a 826 keV, 505 keV and 194 keV decaying out of the aforementioned level. The first two transitions respectively feed the ground-state band levels at 167 keV and 487 keV, while the last transition feeds the even-γ band level at 798 keV.

The 826 and 505 keV transitions are also confirmed by the present work and they are in coincidence with 6 more transitions, namely a 401, 487, 549, 566, 567 and 576 keV, reported for the first time in this work. The partial level scheme of ^{162}Yb showing the extended odd-γ band is shown in Figure 32. The spectra confirming the existence of some of the in-band members of band 7 are shown in Figures 33, 34, 35 and 36.
Setting a gate on the 956 keV transition (see Figure 34 (a)), at the 1881 keV level, allows us to properly see the 549, 566, and 576 keV in-band members. However, the 567 and 576

keV transitions can also be seen, clearly, when the gate is set on the 983 keV transition at the level, 2429 keV (see Figure 34 (b)). The 956 and 983 keV transitions are clearly seen when one sets the gates on the 549 and 566 keV γ ray energies (see Figure 36). It can be seen in this figure that the 566 keV gate clearly shows the 567 keV in-band member, which is not easy to see when the gate is set on the other transitions, as this member is very close in energy to a strong 566 keV transition.

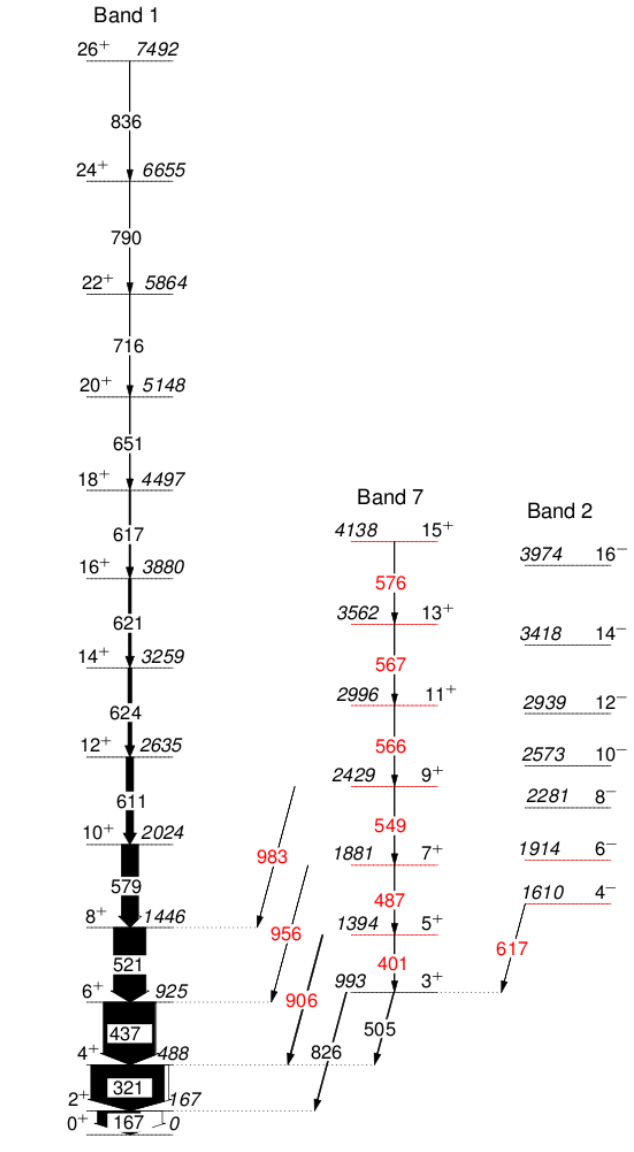

Figure 32: Partial level scheme of ^{162}Yb, showing the ground-state band, an odd γ band, and the energy levels for band 2. The newly observed transitions and energy levels are highlighted in red.

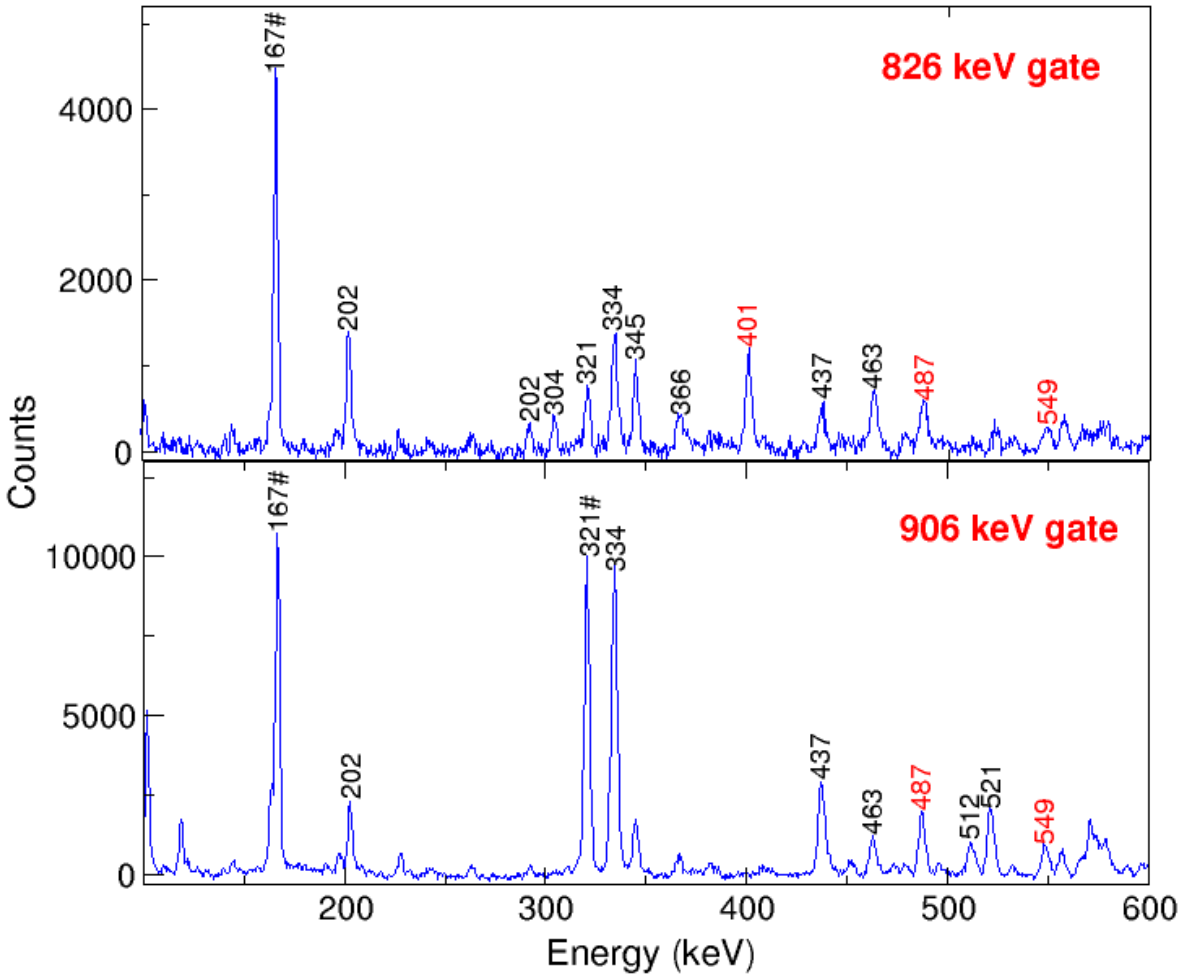

Figure 33: Spectra obtained by setting the gates on the 826 keV (top) and 906 keV (bottom) depopulating transitions of band 7, confirming the extended odd-γ band. In these spectra, the γ transitions that belong to the odd-γ band are colored in red. The ground-state members that are in coincidence with the odd-γ band members are marked by a hash sign. Transitions that do not belong to ^{162}Yb or that are not associated with odd-γ band are colored in black.

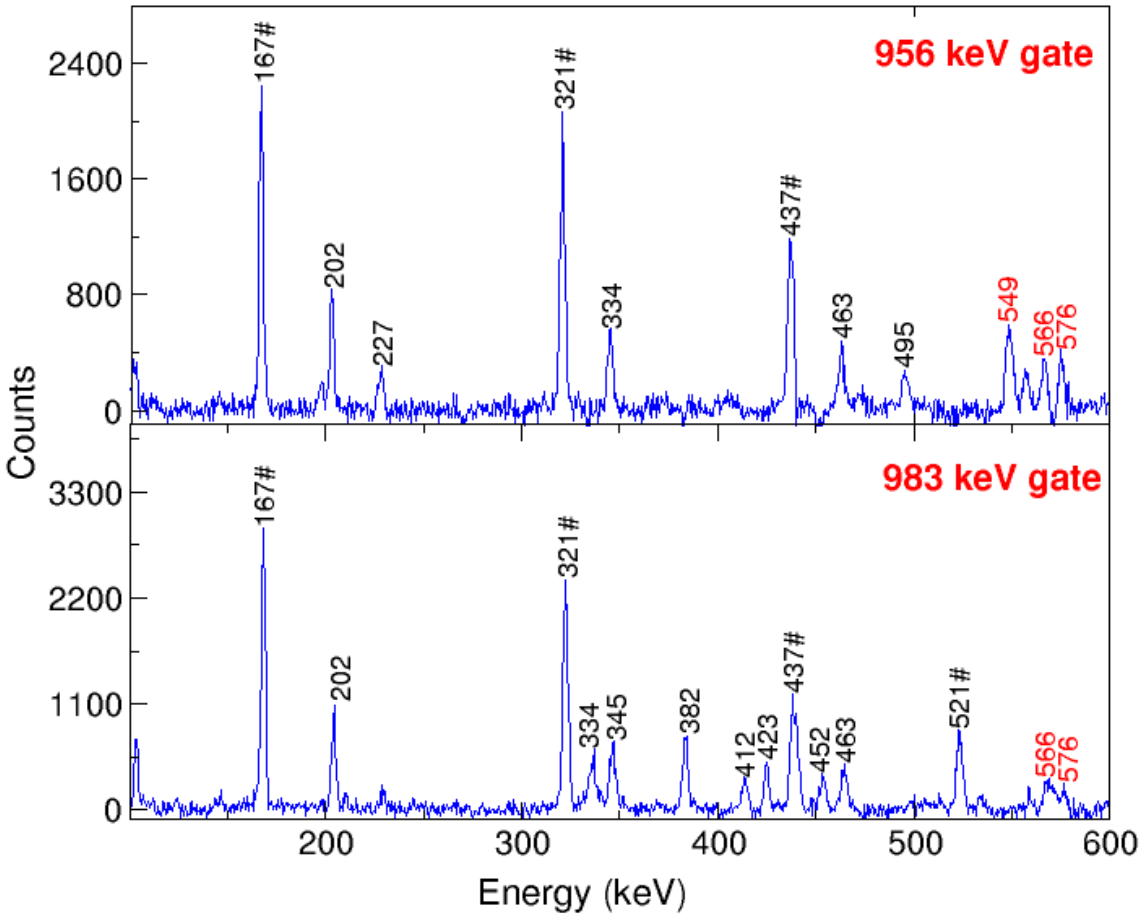

Figure 34: Spectra obtained by setting the gates at 956 keV (top) and 983 keV (bottom) γ-ray energies, which confirm the existence of band 7. The labeling for the γ-ray energies in these spectra is the same as defined in Figure 33.

The spectra obtained by setting the gates on the four depopulating transitions (826, 906, 956 and 983 keV) of band 7 are shown in Figures 33 and 34. In Figures 35 and 36 we show the spectra obtained by setting the gates on the in-band members of this band. These gates confirm the existence of the extended odd-γ band. Thus, the odd-γ band has been extended from spin 3^+ up to spin 15^+.

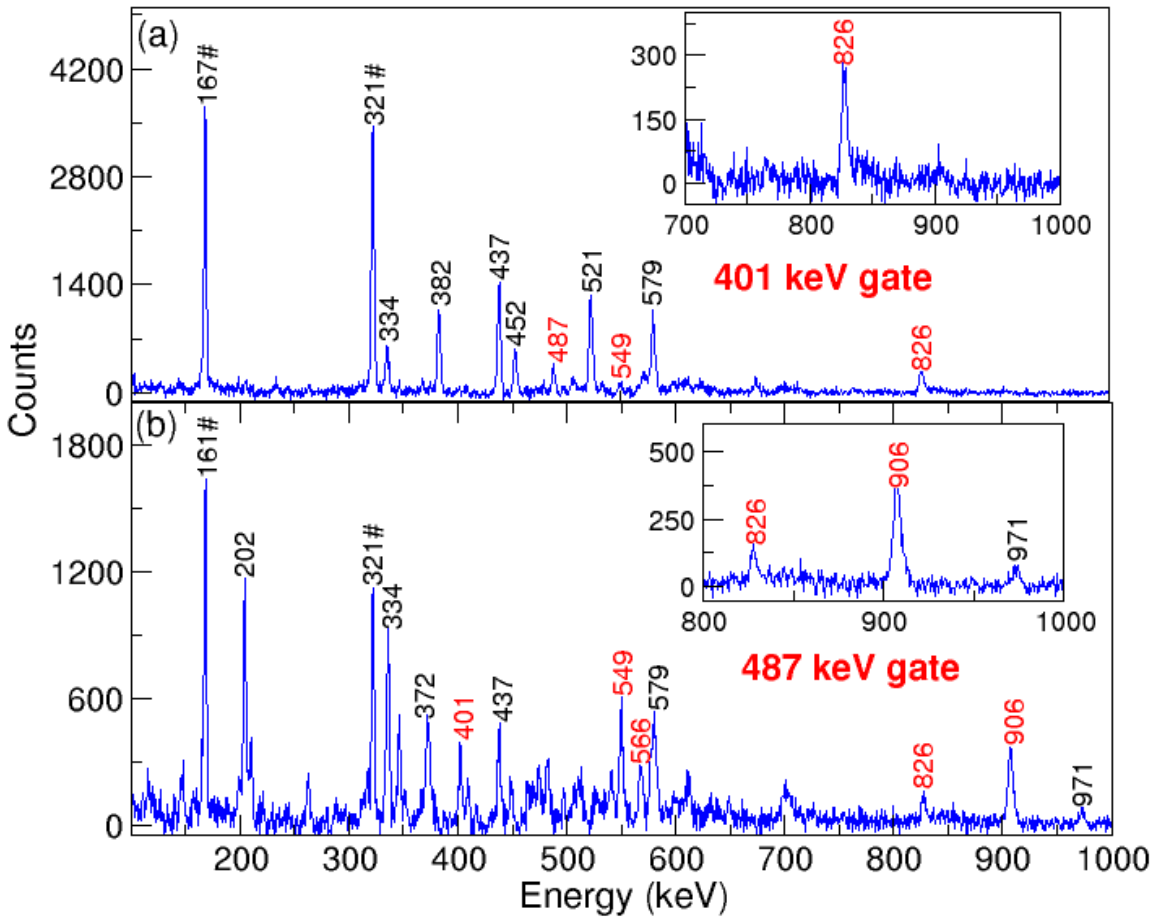

Figure 35: Spectra obtained by setting the gates at 401 keV (a) and 487 keV (b), the in-band members of the odd-γ band, confirming its existence. The labeling for the γ-ray energies in these spectra is the same as defined in Figure 33. In both upper and lower panels of this figure, the insert figures show only the high-energy part of the same gates.

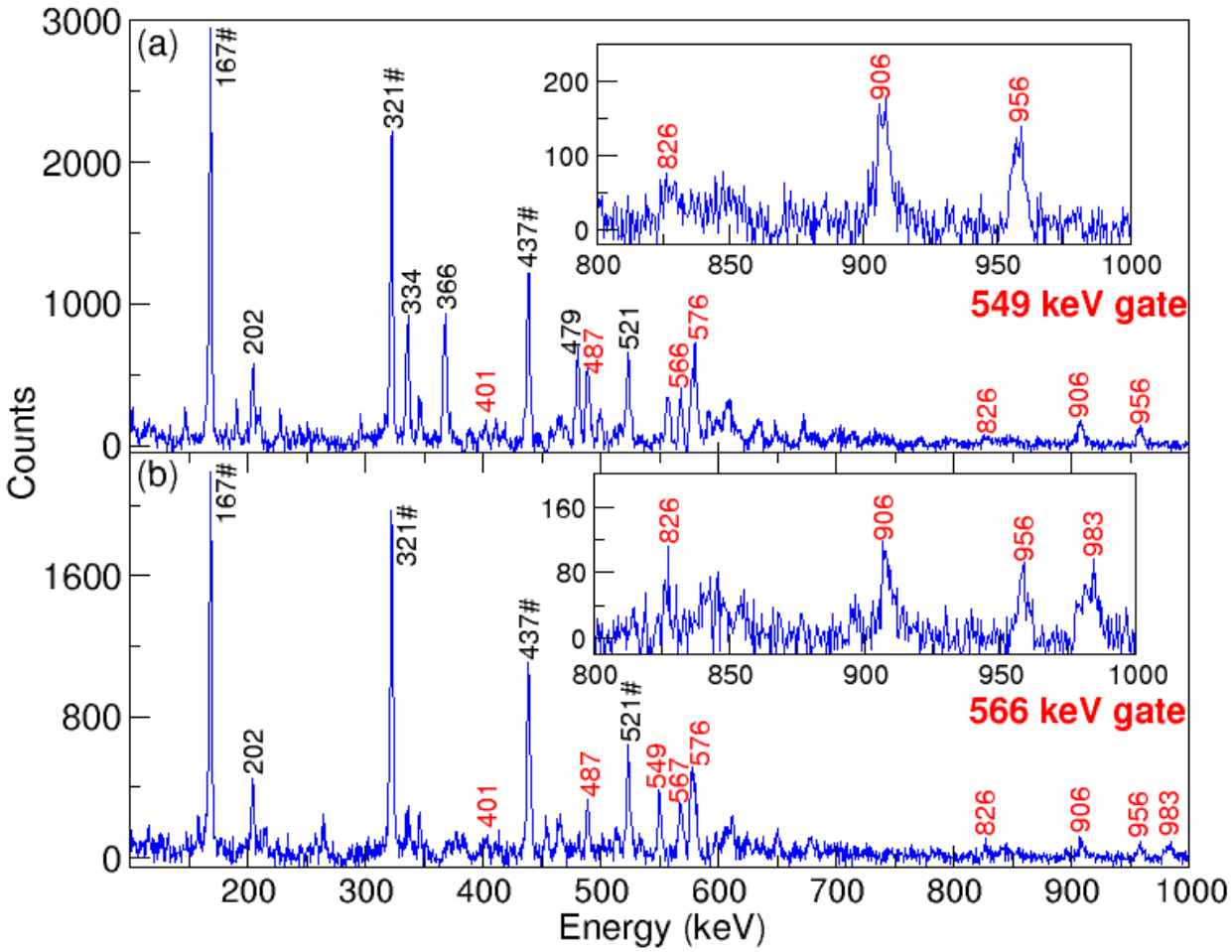

Figure 36: Spectra obtained by setting the gates at 549 keV (a) and 566 keV (b), the in-band members of the odd-γ band, confirming its existence. The labeling for the γ-ray energies in these spectra is the same as defined in Figure 33. The high-energy parts of these spectra are clearly shown in the insert figures.

5 Discussion

The current study focuses on the spectroscopy of low lying positive parity bands, namely bands 5, 6 and 7. The physics pertaining to bands 1, 2, 3 and 4 is not discussed in the current study as it has been well addressed in the previous study [10]. As alluded to earlier, bands 5, 6 and 7 are amongst the newly established structures, reported for the first time in this work. These structures are built on the first excited $K^\pi = 0_2^+$ (band 5) and $K^\pi = 2_\gamma^+$ bands (bands 6 and 7), which are traditionally associated with beta (β) and gamma (γ) vibrational bands.

Some of the studies that have been carried out over the years [1, 2, 14] suggest that the structures associated with the former do not possess the properties expected for a β band (in terms of the electromagnetic transitions and level spacings) - more specifically in the transitional rare-earth nuclei with $N \sim 90$. According to [1, 2], these $K^\pi = 0_2^+$ bands are not due to β vibration along the symmetry axis (as postulated by Bohr and Mottelson) but are a "second vacuum" that can be better explained as a 2p-2h neutron state lowered into the pairing gap by the configuration dependent pairing.
Majola [33] and Shi et al., [18] recently carried out a comprehensive systematic study for the first excited $K^\pi = 0_2^+$ and $K^\pi = 2_\gamma^+$ bands of nuclei with $N = 88, 90$ and 92 and with proton numbers ranging from $Z = 62$ to 70. The theoretical approach that has been adopted by these studies [18, 33] uses a modern form of the Bohr Hamiltonian, a five-dimensional collective Hamiltonian (5DCH) based on the covariant density functional theory (CDFT). The solutions of the 5DCH-CDFT corresponding to the $K^\pi = 0_2^+$ and $K^\pi = 2_\gamma^+$ bands are then interpreted as the β and γ vibrational bands, respectively. The aforementioned studies [18,33] reported that there is a good agreement between the measured observables and the 5DCH-CDFT calculations – in terms of the level energies and transition rates. Thus implying that the traditional interpretation of the $K^\pi = 0_2^+$ as a β vibration remains valid. The nucleus of interest, namely ^{162}Yb, has $N = 92$ neutrons and is in the vicinity of these nuclei ($N \sim 90$ with $Z = 62$ to 70), with $K^\pi = 0_2^+$ and $K^\pi = 2_\gamma^+$ bands that were thoroughly investigated by [18, 33] and found to be in good agreement

with the solutions of the 5DCH-CDFT calculations. The main aim of this study is to test whether the newly established low lying positive parity excitations (i.e. bands 5, 6 and 7) in ^{162}Yb can better be described by the 5DCH-CDFT calculations, which has been successful in explaining the microscopic properties of its counterparts in the neighboring nuclei. The current results are also explained in the context of the systematic of the region in order to get a much deeper insight on the microscopic nature of the $K^{\pi} = 0_2^+$ and $K^{\pi} = 2_{\gamma}^+$ bands in the $N \sim 90$ nuclei. While the majority of the experimental data for the systematic nuclei studied in this work have been mainly collected at iThemba LABS, using the AFRODITE array [9] , some of the data sets were collected using the JUROGAM [40] and GAMMASPHERE arrays [41].

5.1 Systematic of the first excited $K^{\pi} = 0_2^+$ and the $K^{\pi} = 2_{\gamma}^+$ bands for the transitional rare-earth nuclei with $N \sim 90$.

The systematic behavior of the $K^{\pi} = 0_2^+$ and $K^{\pi} = 2_{\gamma}^+$ low-lying structures have been extensively studied in the last few years. Significant progress has been made in identifying the bands built on these $K^{\pi} = 0_2^+$ and $K^{\pi} = 2_{\gamma}^+$ structures in the transitional rare-earth region. In a search for a definitive and complete microscopic picture of the so-called γ and β vibrational bands in the transitional rare-earth nuclei, a comprehensive systematic review has been performed for nuclei in the $A \sim 160$ mass region - with emphasis on $N \sim 90$ isotones and they are compared with the experimental results of the nucleus of interest, namely ^{162}Yb.

Shown in Figure 37 are systematic plots of excitation energy (minus the energy of a rigid rotor) [42] of rotational levels built on the ground-state, 0_2^+, and γ bands observed in transitional rare-earth nuclei with $N = 88, 90$ and 92. The new experimental results deduced from the current work are also shown in this figure, see Figure 37 (c).
The structural behavior as well as the trends for the majority of 0_2^+ and γ bands, in $N = 88, 90$ isotones, shown in Figure 37, have been well established and are explained in detail in Ref. [33]. Here we focus mainly on our new experimental results, presented in Chapter 4, and we discuss them in the systematic context of ^{162}Yb being an $N = 92$ isotone and $Z = 70$ isotope.

When one moves from the $N = 88$ isotones to $N = 92$ isotones, a change in deformation is expected. In almost all cases presented in Figure 37, the moment of inertia gradually changes as a function of neutron number N. In fact, the slopes of all bands become less steep with increase in N and this is due to the change in deformation. The change in deformation seems to have a major effect on the moment of inertia of the 0_2^+ band. This is more apparent for lighter nuclei with $N = 92$, such as ^{154}Sm and ^{156}Gd, where the structural behavior of moment of inertia for the 0_2^+ bands is fast approaching that of a rigid rotor. This trend becomes more pronounced with increase in the number of neutrons (i.e. $N = 94, 96$ etc).

Just like in the $N = 88, 90$ nuclei, at low spin, the 0_2^+ bands lie low in excitation energy, relative to γ bands. However, this trend changes as the proton number increases, and this change is accompanied by a band crossing between the γ and 0_2^+ bands. In the case of $N = 92$ isotones, the crossing begin to take place in ^{156}Gd. This phenomenon is somehow delayed for $N = 88, 90$ isotones and it does not occur until one reaches the Er isotopes, particularly ^{156}Er and ^{158}Er, see Figure 37.

As can be seen in Figure 37, rotational structures built on γ bands have also been observed in all $N = 88, 90$, and 92 isotones except for ^{158}Yb - where the odd spin members of the γ bands remain elusive. According to [43], γ bands generally track their intrinsic configuration as a function of spin. In other words, γ bands are expected to have a moment of inertia similar to that of their intrinsic configuration. This appears to be the case for all the ground-state and γ bands presented in Figure 37 with the exception of a few cases where even spin members of the γ bands deviate from this trend. In general, there are more rotational levels built on positive parity structures with even spin compared to those built on their odd spin counterpart. This therefore makes the structures built on the former to be more susceptible to band mixing and/ or crossing. As a result, in some cases, the even spin γ bands may mix with neighboring levels, such as those built on the $K^\pi = 0_2^+$ bands, causing the former to lie low in energy, relative to their odd spin counterpart - thus distorting the aforementioned "tracking pattern" in even spin γ bands. This phenomenon is clearly demonstrated in Figure 37, where all odd γ bands in this figure faithfully track the ground-state band throughout as a function of spin, while

some of the even γ bands deviate from this trend mainly because of the band crossings. This is even more apparent in ^{156}Er and ^{160,162}Yb where the odd spin members of the γ band faithfully track the ground state band while the rotational levels of their even spin counterpart deviate from this trend - mainly because of the band mixing due to the crossing between its members and the levels built on the 0_2^+ band.

The interaction observed between the γ and 0_2^+ bands in ^{156}Er and ^{160,162}Yb actually forms what is known as a Landau-Zenner crossing [44–47] - where the interacting levels of the crossing bands that lie close in energy repel each other. Thus triggering an interchange in nuclear properties.
This phenomenon is demonstrated for ^{162}Yb in Figure 38 - where the crossing occurs at about spin 6^+. It can be seen in Figure 38 (a) that the even spin members of the γ band interact with the 0_2^+ band, forming a classical Landau-Zenner crossing [44–47]. Figure 38 (b) shows the behavior of the crossing bands (bands 5 and 6) after exchanging their energy level after the crossing point (6^+). Basically, the latter shows how the mixing bands look like after the band crossing has been untangled. In the following subsection the level energies presented in Figure 37 are compared with theory. Here the Landau-Zenner crossings have been untangled in ^{156}Er and ^{160,162}Yb for comparison purposes.

The 0_2^+ bands have been observed in all nuclei with the exception of ^{158}Yb, see Figure 37. It is worth noting that the even spin γ band in ^{158}Yb had previously been interpreted as a 0_2^+ band in [33]. However, in the current study we have revised this interpretation and reassigned this structure to be a candidate for the even spin γ band. The arguments used to justify this reassignment are given below.
Firstly, the band-head energy of the γ band is generally fixed at $\sim 1MeV$ from Sm to Yb and this is consistent with the band in question being a candidate for the 0_2^+ band in ^{158}Yb. On the other hand, as mentioned above, at low spin, the 0_2^+ bands in lighter $N = 88$ isotones, presented in Figure 37, lie low in excitation energy, relative to the even spin members of the γ bands. However, this trend changes with increase in proton number. In fact, the band-head energy of the 0_2^+ band appears to increase gradually in excitation energy, such that its band-head energy can be expected to be well above 1 MeV in ^{158}Yb. This is not compatible with the general trend expected for 0_2^+ bands in

Yb isotopes in the $A \sim 160$ mass region, see Figure 37 (a), (b) and (c), and therefore leaves the band in question as the ideal candidate for the γ band in ^{158}Yb.

Finally, in Yb isotopes, even spin members of the γ band get pushed down in energy, as a function of spin due to band crossing. The effect of such a crossing is also evident in the γ band in ^{158}Yb.

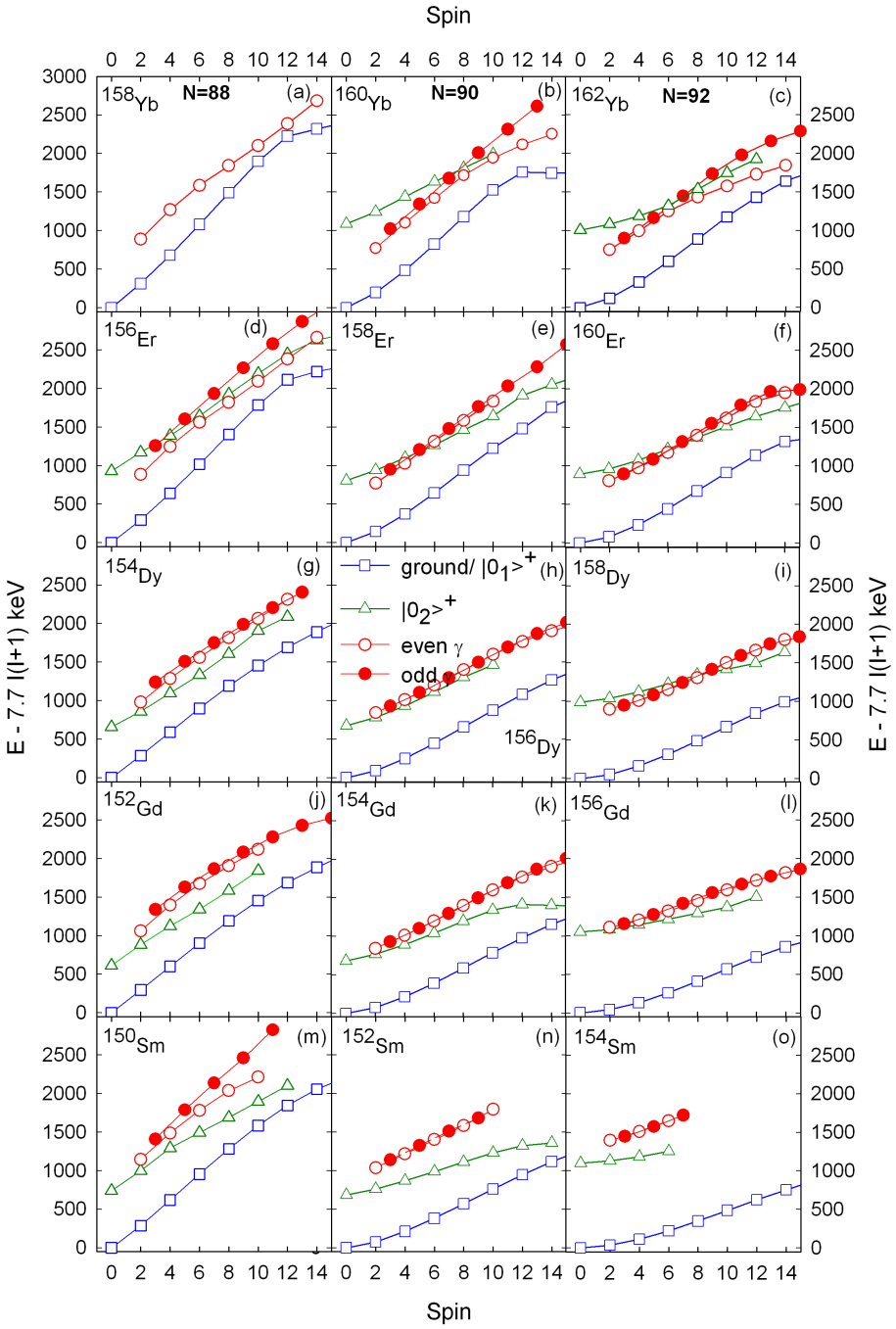

Figure 37: A plot of excitation energy minus the energy of a rigid rotor for the ground-state band, γ band, and 0_2^+ band observed in nuclei with $N = 88, 90$, and 92. Modified from [33].

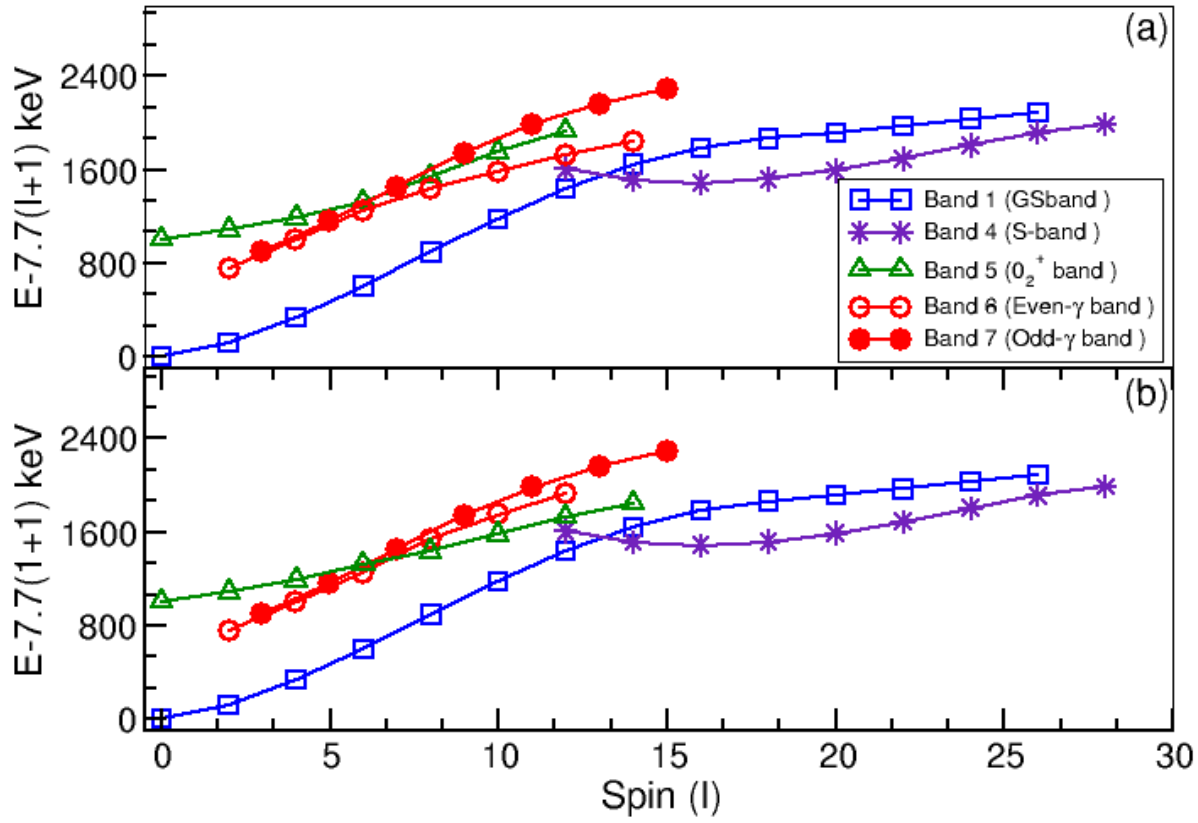

Figure 38: A plot of excitation energy minus the energy of a rigid rotor for the ground-state band, γ band, 0_2^+ band and S-band, showing the crossing between bands 5 and 6 before (a) and after (b) exchanging their energy levels after the crossing point ($\sim 6^+$).

5.2 Systematic comparison between observables and the solutions of the 5DCH-CDFT for $N \sim 90$ nuclei with $A \sim 160$.

The low-lying excitations in even-even deformed nuclei, with $N = 88, 90$, and 92, can be explained using the five-dimensional collective Hamiltonian (5DCH) [16, 17]. The 5DCH can simultaneously treat the quadrupole vibrational and rotational excitations. In this approach, the potential is calculated by the microscopic method based on the density functional theory. The parameters are determined by constrained self-consistent relativistic mean-field calculations for triaxial shapes and pairing correlations are taken

into account by means of the BCS method. The collective Hamiltonian is defined as:

$$\hat{H}_{coll}(\beta,\gamma) = \hat{T}_{vib}(\beta,\gamma) + \hat{T}_{rot}(\beta,\gamma,\Omega) + V_{coll}(\beta,\gamma) \tag{13}$$

where $\hat{T}_{vib}(\beta,\gamma)$ is the vibrational kinetic energy, $\hat{T}_{rot}(\beta,\gamma,\Omega)$ is the rotational kinetic energy and $V_{coll}(\beta,\gamma)$ is the collective potential. The angles $\Omega \equiv (\phi,\theta,\psi)$, are the Euler angles that define the orientation of the intrinsic principal axes in the laboratory frame and (β,γ) are the deformation parameters. The three terms of equation 13 are well explained in refs. [16–18]. The diagonalization of the Hamiltonian in equation 12, deduced using the PC-F1 density functional gives rise to an excitation spectrum with band-head energies with $K = 0^+$ and $K = 2^+$ states, which correspond to single phonon vibrational states with a varying degree of angular momenta components along the symmetry axis. These structures are respectively known as β ($K = 0^+$) and γ ($K = 2^+$) vibrational bands.

5.3 Level energies

Figures 39, 40 and 41, show systematic comparison between the theory and experimental data presented in Figure 37. Generally, there is a very good agreement between data and theory for both γ and 0_2^+ bands, particularly for $N = 88, 90$ isotones, see Figures 39 and 40.

(i) The energy spacings between the ground, γ and 0_2^+ bands are well approximated. The order of appearance is also well reproduced as a function of excitation energy.
(ii) The energy splititng between the odd spin and even members of the γ band is quite remarkable. It is worth noting that the band that has been reassigned to be a γ band candidate in this work is in good agreement with the prediction of the 5DCH-CDFT calculations, thus giving us confidence in our assignment.
(iii) All the unperturbed members of the γ band, particularly the odd spin members, appear to track the ground-state band as expected. This trend is well reproduced by the calculations.
(iv) Finally, there is an apparent band crossing observed between members of the γ bands and the 0_2^+ bands, particularly for the heavy $N = 88$ and 90 isotones – from Er to Yb. This phenomenon is also well reproduced by the theory.

With the aid of data from the current work, we also confirm similar trends in ^{162}Yb, as outlined above for $N = 88$ and 90 isotones, namely (i), (ii), (iii) and (iv). While features highlighted in (ii) and (iv) above, pertaining to γ bands are also well reproduced by the theory, there appear to be a discrepancy between the predicted and experimental levels of the majority of 0_2^+ bands with $N = 92$. In fact, the theory seem to underestimate the excitation energy for ^{158}Dy, ^{160}Er and ^{162}Yb. On the contrary, an overestimation is actually observed for the lighter $N = 92$ isotones, namely ^{156}Gd and ^{154}Sm. These discrepancies have been identified as the sole reason why features highlighted in (i) and (iv) cannot be reproduced by the calculations in some of $N = 92$ isotones.

It is worth noting that the moment of inertia for the experimental bands, drops gradually, after spin 8^+, particularly for 0_2^+ bands in $N = 90$ isotones. This is in contrast with what is observed theoretically where these level energies continuously increase with spin. We attribute this discrepancy to the influence of band crossing(s) that is beyond the scope of the present 5DCH-CDFT calculation.

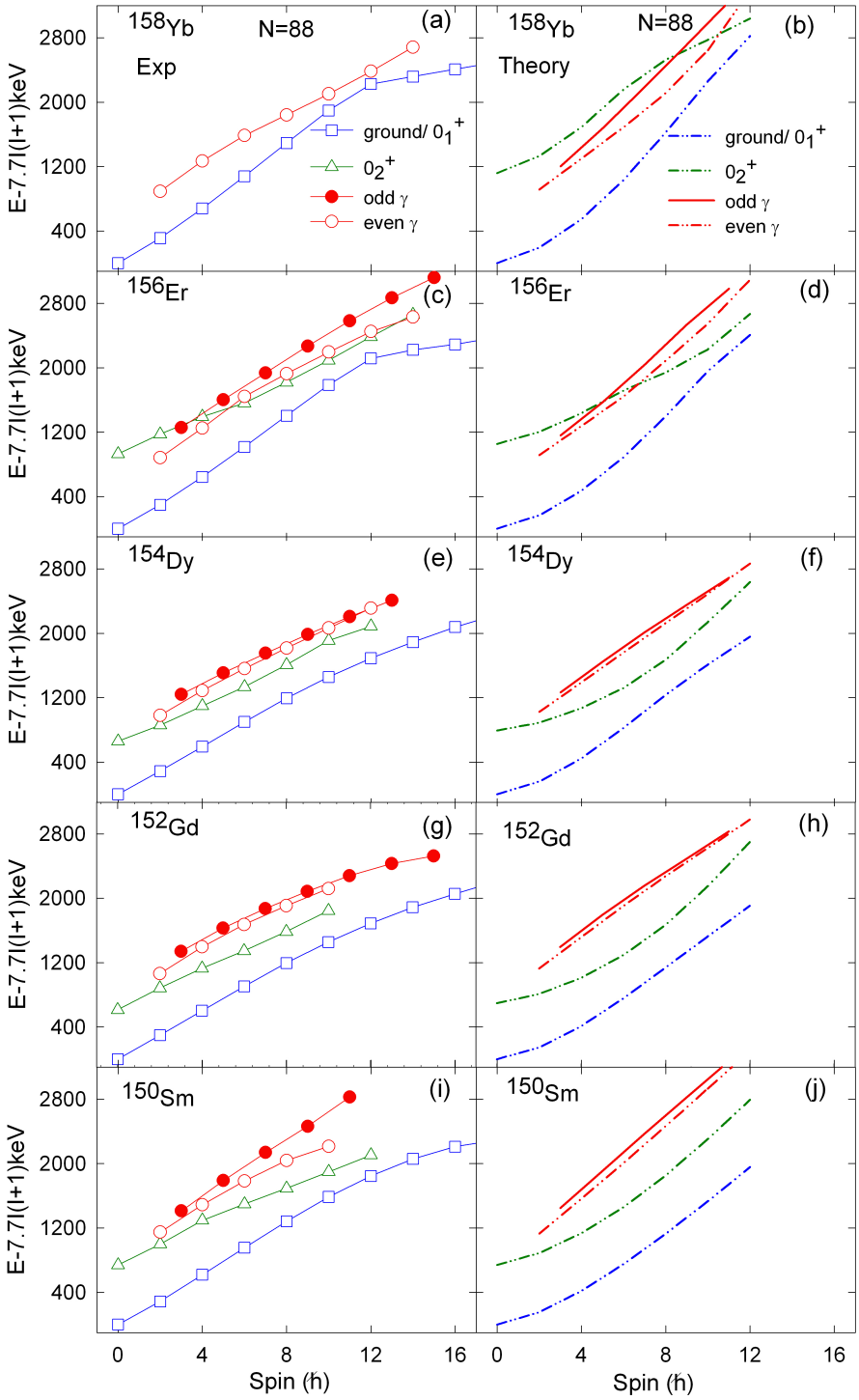

Figure 39: A plot of excitation energy minus the energy of a rigid rotor for the ground-state band, γ band, and 0_2^+ band observed in nuclei with $N = 88$, in comparison with the theoretical data, calculated by 5DCH-CDFT with density functional PC-PK1. Modified from [18].

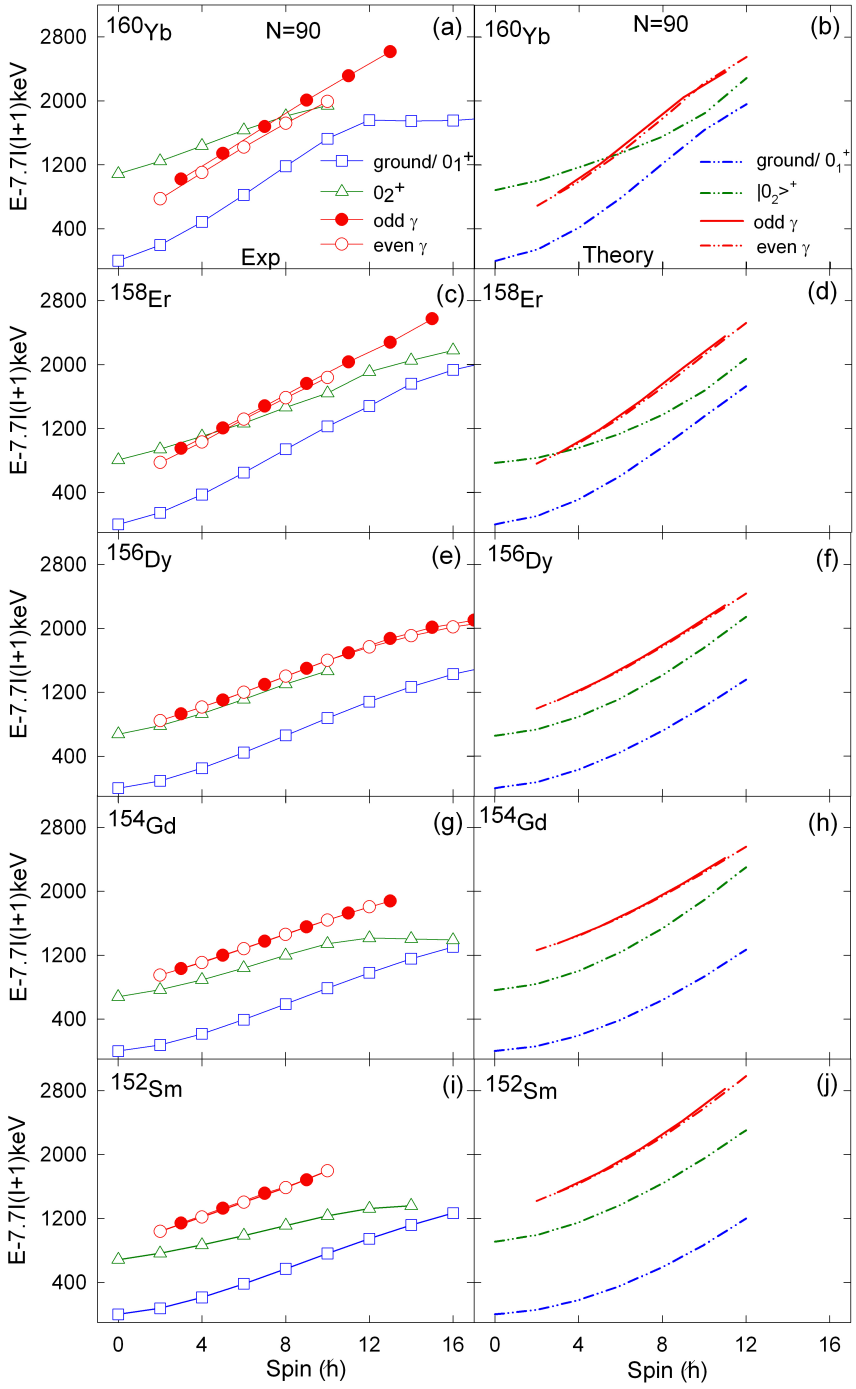

Figure 40: A plot of excitation energy minus the energy of a rigid rotor for the ground-state band, γ band, and 0_2^+ band observed in nuclei with $N = 90$, in comparison with theoretical data, calculated by 5DCH-CDFT with density functional PC-PK1. Modified from [18].

.

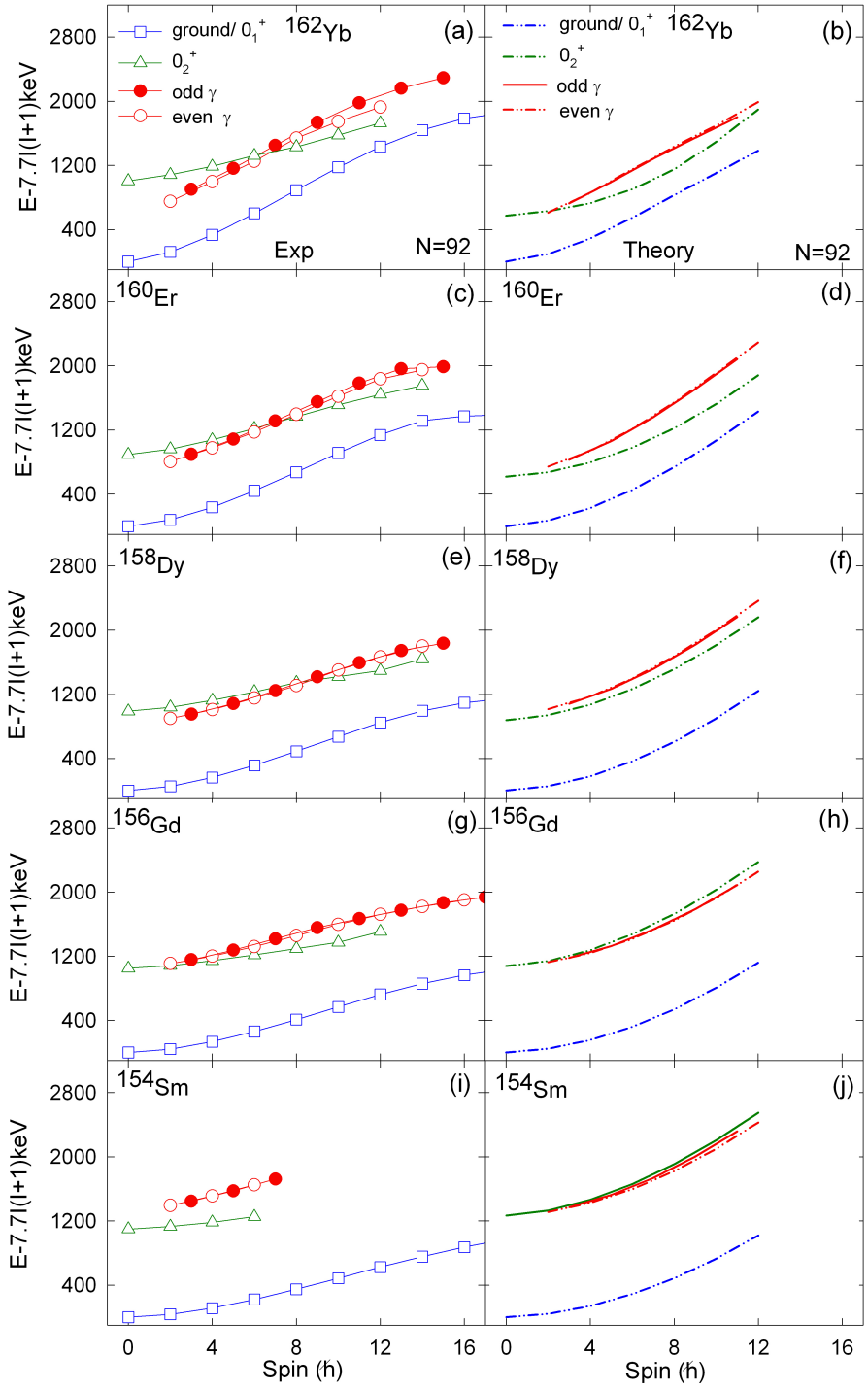

Figure 41: A plot of excitation energy minus the energy of a rigid rotor for the ground-state band, γ band, and 0_2^+ band observed in nuclei with $N = 92$, in comparison with theoretical data, calculated by 5DCH-CDFT with density functional PC-PK1. Modified from [18].

5.4 Transition rates and probabilities

In the 5DCH-CDFT model, the $B(E2)$ transition rates, which are parameter free may be determined using the value of the proton charge. These transition rates can be calculated for in-band transitions as well as inter-band transitions, connecting the excited states of the vibrational bands to the ground-state band. In turn, these quantities can be compared to experimental $B(E2)$ values as demonstrated below. The theory of transition probabilities is well established and has been well explained in [48].

Figure 42 shows the in-band $B(E2 : I \rightarrow I-2)$ values deduced for the ground-state and 0_2^+ bands in $N = 88, 90$ and 92 isotones. At low spin, the experimental data appear to increase with increase in spin, for both bands, and this trend is remarkably well reproduced by the calculations. However, it is worth noting that there is a gradual decrease in the experimental $B(E2 : I \rightarrow I-2)$ values, at relatively high spin, particularly for Dy to Yb isotopes. This experimental feature is not well accounted for theoretically. This discrepancy may be attributed to the influence of band crossing(s) that goes beyond the scope of the present 5DCH-CDFT calculation. In Figure 42, it is clear that the 5DCH-CDFT calculation predicts a different trend for the in-band $B(E2 : I \rightarrow I-2)$ values between the ground-state and 0_2^+ bands, namely ^{154}Dy, ^{156,158,160}Er, and ^{160,162}Yb. Unfortunately, currently there is still no experimental data for these cases. The discrepancy predicted for the behavioral changes between the ground-state and 0_2^+ bands may imply that the deformations of the two bands are different, thus suggesting that these nuclei are likely to manifest the phenomena of shape coexistence. However, more experimental data are needed to confirm this.

The branching ratios for electric quadrupole and magnetic dipole transitions, depopulating the same state can be calculated using the following equation,

$$\frac{B(M1 : I \rightarrow I-I)}{B(E2 : I \rightarrow I-2)} = 0.697 \frac{[E_\gamma(I \rightarrow I-2)]^5}{[E_\gamma(I \rightarrow I-I)]^3} \frac{1}{(\delta^2+1)} \frac{1}{\lambda} [\frac{\mu_N^2}{e^2 b^2}] \tag{14}$$

where E_γ is the γ ray energy, δ is the mixing ratio parameter, which gives information about the $E2/M1$ admixture in the dipole magnetic transitions and λ is multipole order. The term $\frac{1}{\lambda}$, is a ratio of measured intensities for both the $M1$ and $E2$ transitions.

Figures 43 - 46 show a systematic comparison between the experiment and 5DCH-CDFT calculations for branching ratios of 0_2^+ and γ bands with respect to the ground-state band. Figures 43 and 44 respectively show that the agreement between data and theory for the branching ratios, out-of-band $I \rightarrow I$ and $I \rightarrow (I-2)$ to the in-band $B(E2)$, is very good. In Figure 43, the structural behavior for experimental $B(E2; I_{0_2^+} \rightarrow (I-2)_g / B(E2; I_{0_2^+} \rightarrow (I-2)_{0_2^+}$ branching ratios are well reproduced by theory. It is worth noting that the theory, at low spin, seem to underestimate the branching ratios for some nuclei with $N = 88$. A quite impressive agreement is observed between the experimental and theoretical results in the $N = 90$ isotone. In the $N = 92$ isotone, the comparison has only been made for ^{158}Dy, as there are currently no experimental data available for other nuclei. The experimental branching ratios for this nucleus are well reproduced by theory at low spin, however, a sudden increase in $B(E2; I_{0_2^+} \rightarrow (I-2)_g / B(E2; I_{0_2^+} \rightarrow (I-2)_{0_2^+}$ values is observed at relatively higher spin ($I > 8^+$), whereas the theoretical values remain almost constant as spin increases. We attribute this discrepancy to the influence of band crossing(s) that is beyond the scope of the present 5DCH-CDFT calculation.

Figure 44 shows a very good agreement between the theory and experimental results for $B(E2; I_{0_2^+} \rightarrow (I-2)_g / B(E2; I_{0_2^+} \rightarrow (I-2)_{0_2^+}$. It is worth noting that there are minor discrepancies for some of the $N = 92$ isotones, where the structural behavior for experimental values are not well reproduced by theory. This may be due to band crossing observed between the 0_2^+ and γ bands.

In Figure 45, it is seen that the theoretical values of the 5DCH model reproduces the $B(E2; I_\gamma \rightarrow I_g) / B(E2; I_\gamma \rightarrow (I-2)_\gamma$ branching ratios (i.e. for γ bands) very well in almost all cases presented in this figure. The branching ratios for the transitions decaying out of the odd spin states of the γ bands are shown in Figure 46. In this figure, the vertical lines can be understood as an error bar, thus implying that the $B(E)$ value with a correct mixing ratio lies anywhere within the limit. The lowest values of this vertical lines correspond to $\delta = 1$ (see Equation 14), while the highest correspond to a pure $E2$. Finally, Figure 46 shows a good agreement between the experimental data and theory. In particular, the staggering trend between the $B(E2; I_\gamma \rightarrow (I-2)_g) / B(E2; I_\gamma \rightarrow (I-2)_\gamma$ for odd I and $B(E2; I_\gamma \rightarrow (I-2)_g) / B(E2; I_\gamma \rightarrow (I-2)_\gamma$ for even I is well reproduced

by theory.

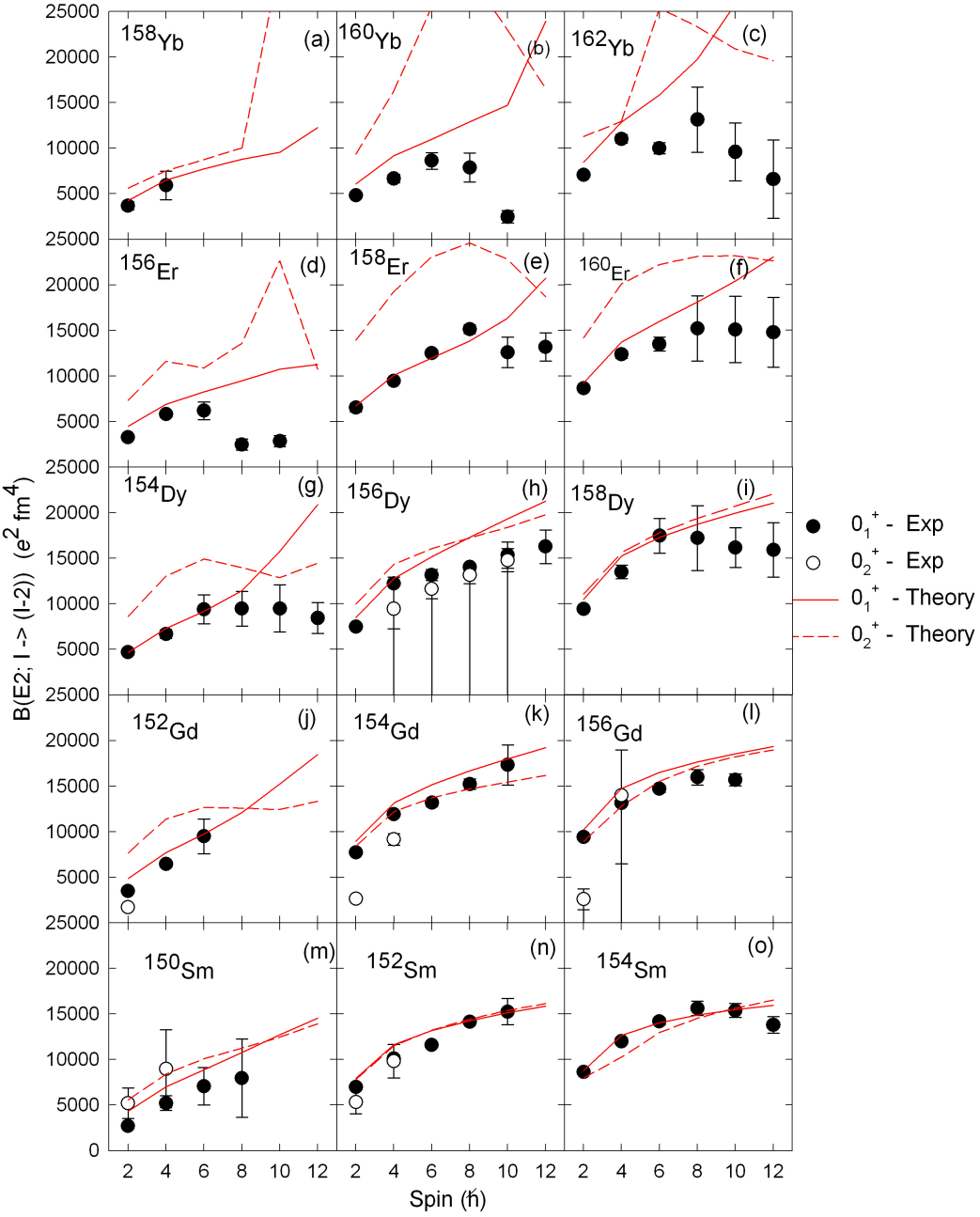

Figure 42: The experimental in-band $B(E2 : I \rightarrow I-2)$ values for the ground-state and 0_2^+ bands in $N = 88, 90$ and 92 isotones, in comparison with the theoretical calculations. Modified from [18].

.

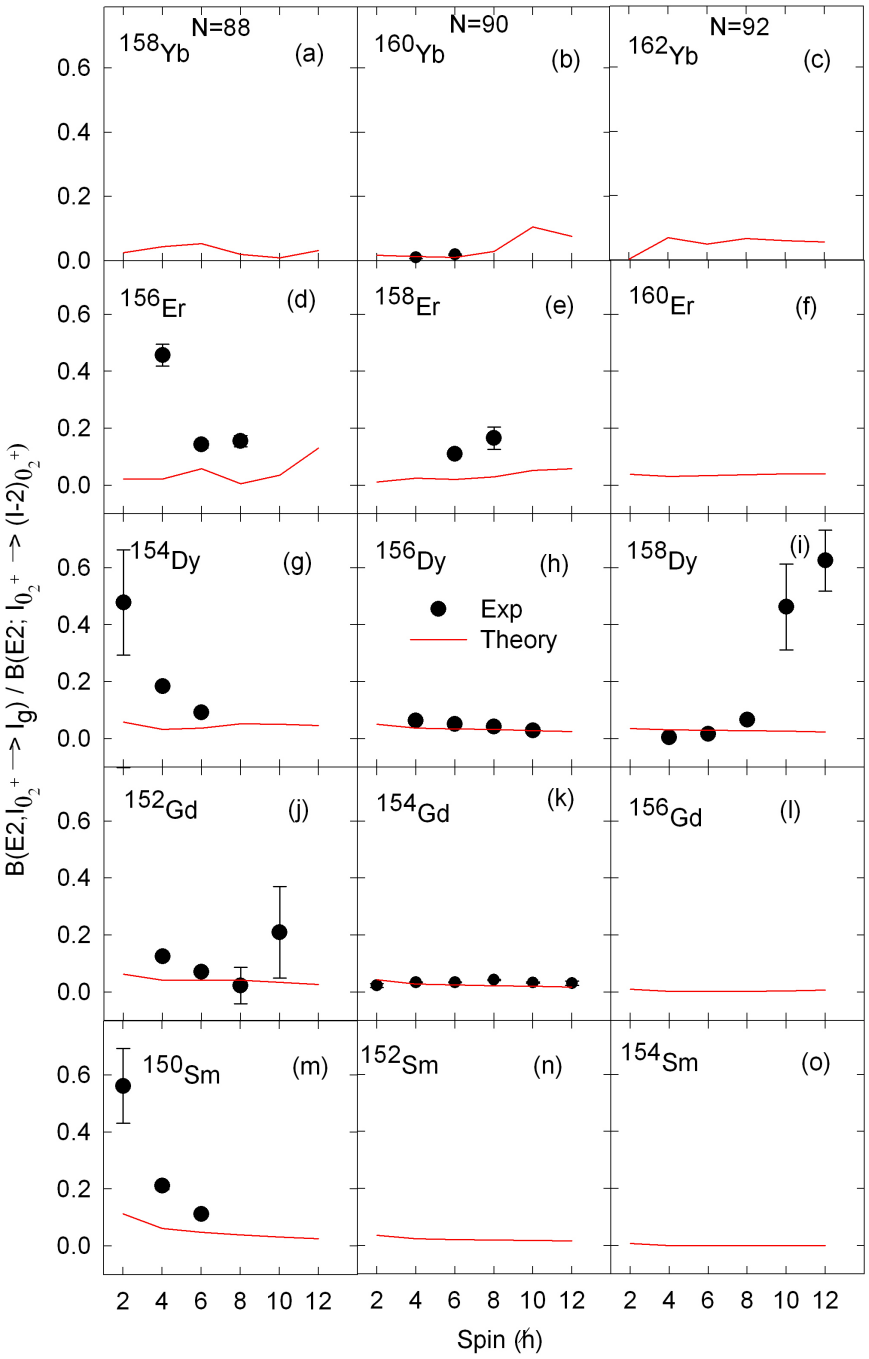

Figure 43: The available experimental branching ratios for out-of-band to in-band transitions, $B(E2; I_{0_2^+} \rightarrow I_g / B(E2; I_{0_2^+} \rightarrow (I-2)_{0_2^+}$ for the 0_2^+ bands in the N = 88, 90, and 92 isotones, in comparison with the theoretical calculations. Modified from [18].

.

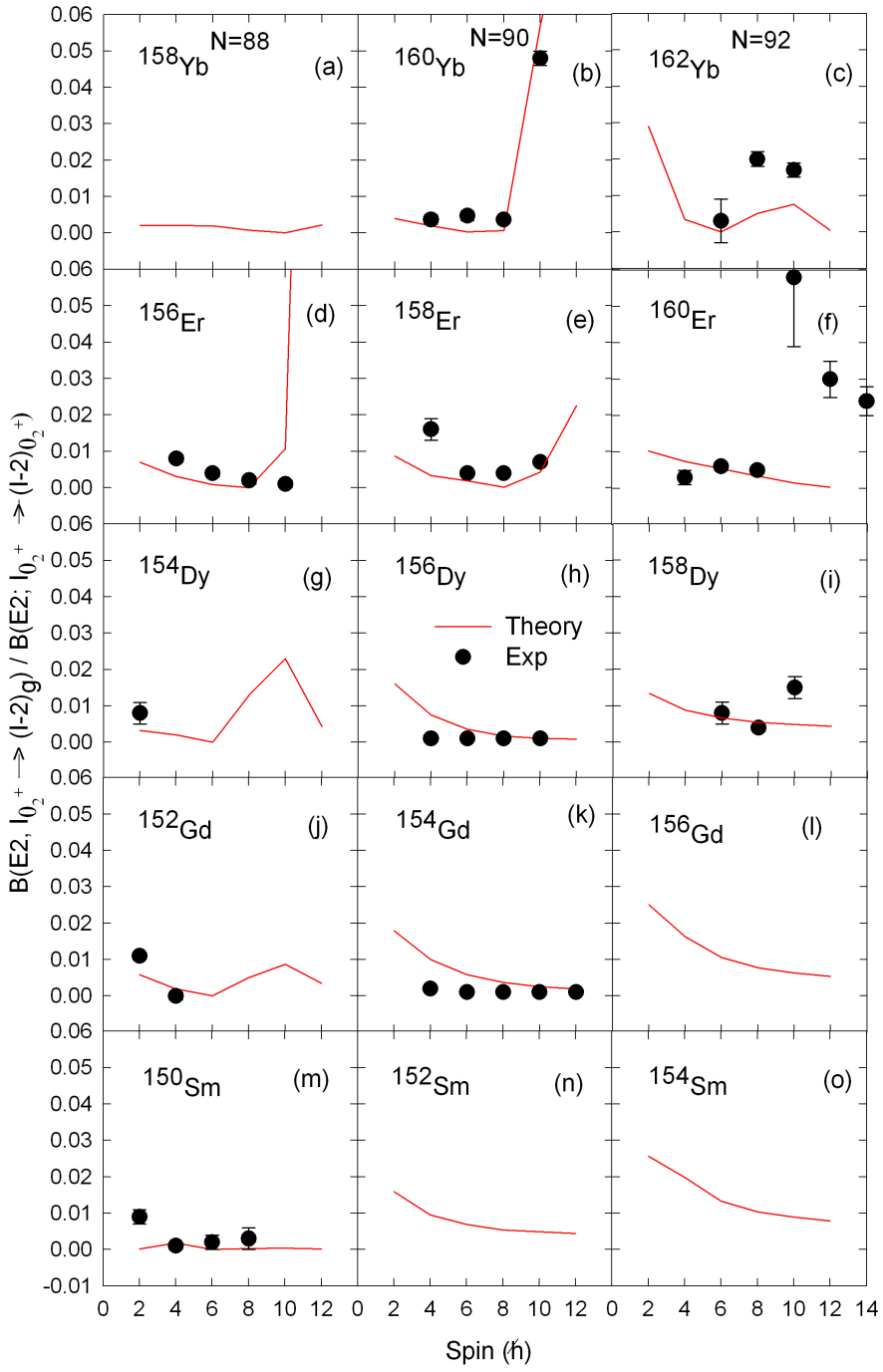

Figure 44: The available experimental branching ratios for out-of-band to in-band transitions, $B(E2; I_{0_2^+} \rightarrow (I-2)_g / B(E2; I_{0_2^+} \rightarrow (I-2)_{0_2^+}$ for the 0_2^+ bands in the N = 88, 90, and 92 isotones, in comparison with the theoretical calculations. Modified from [18].

.

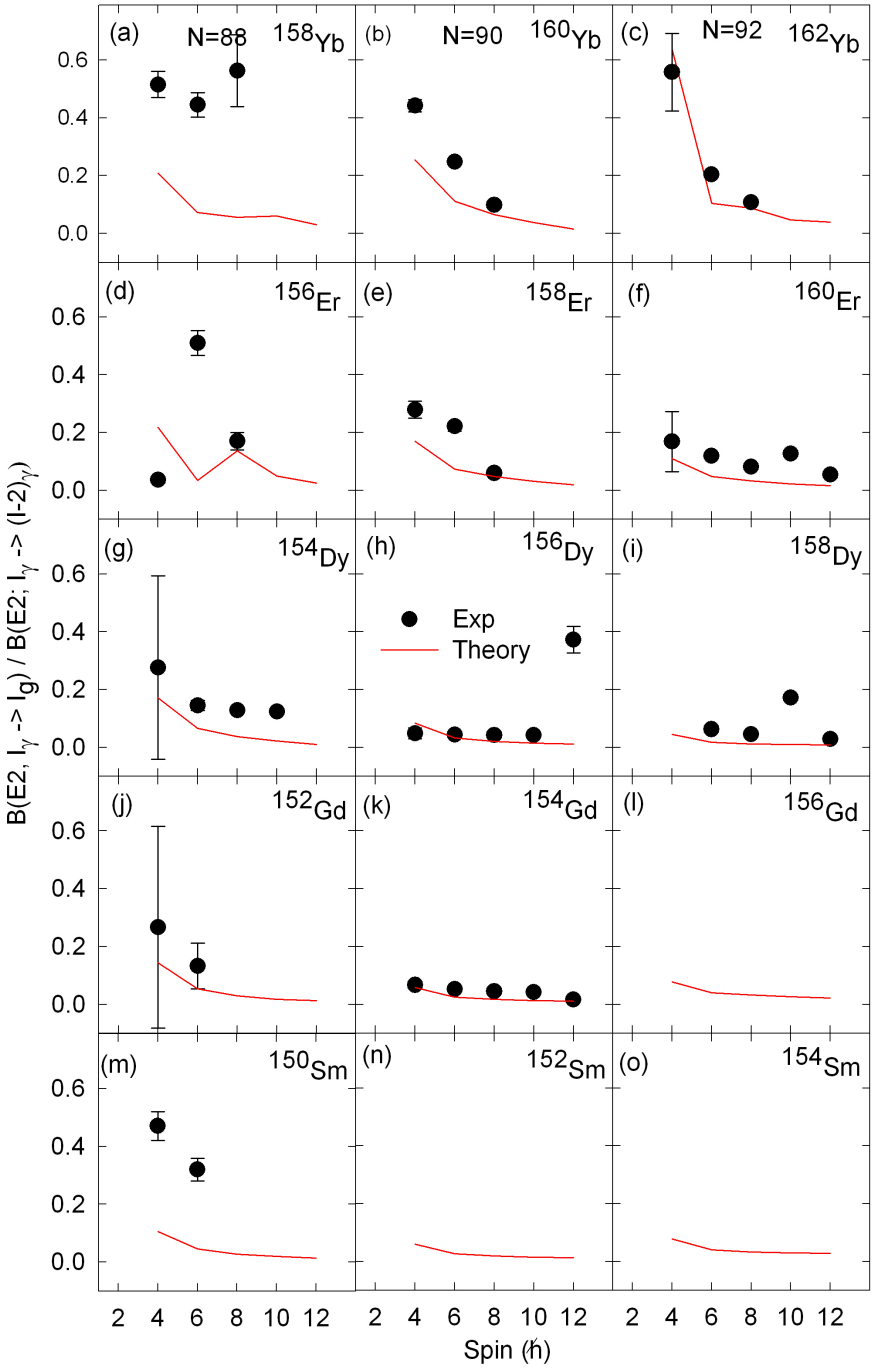

Figure 45: The available experimental branching ratios for out-of-band to in-band transitions, $B(E2; I_\gamma \rightarrow I_g)/B(E2; I_\gamma \rightarrow (I-2)_\gamma$ for the γ bands in the N = 88, 90, and 92 isotones, in comparison with the theoretical calculations. Modified from [18].

.

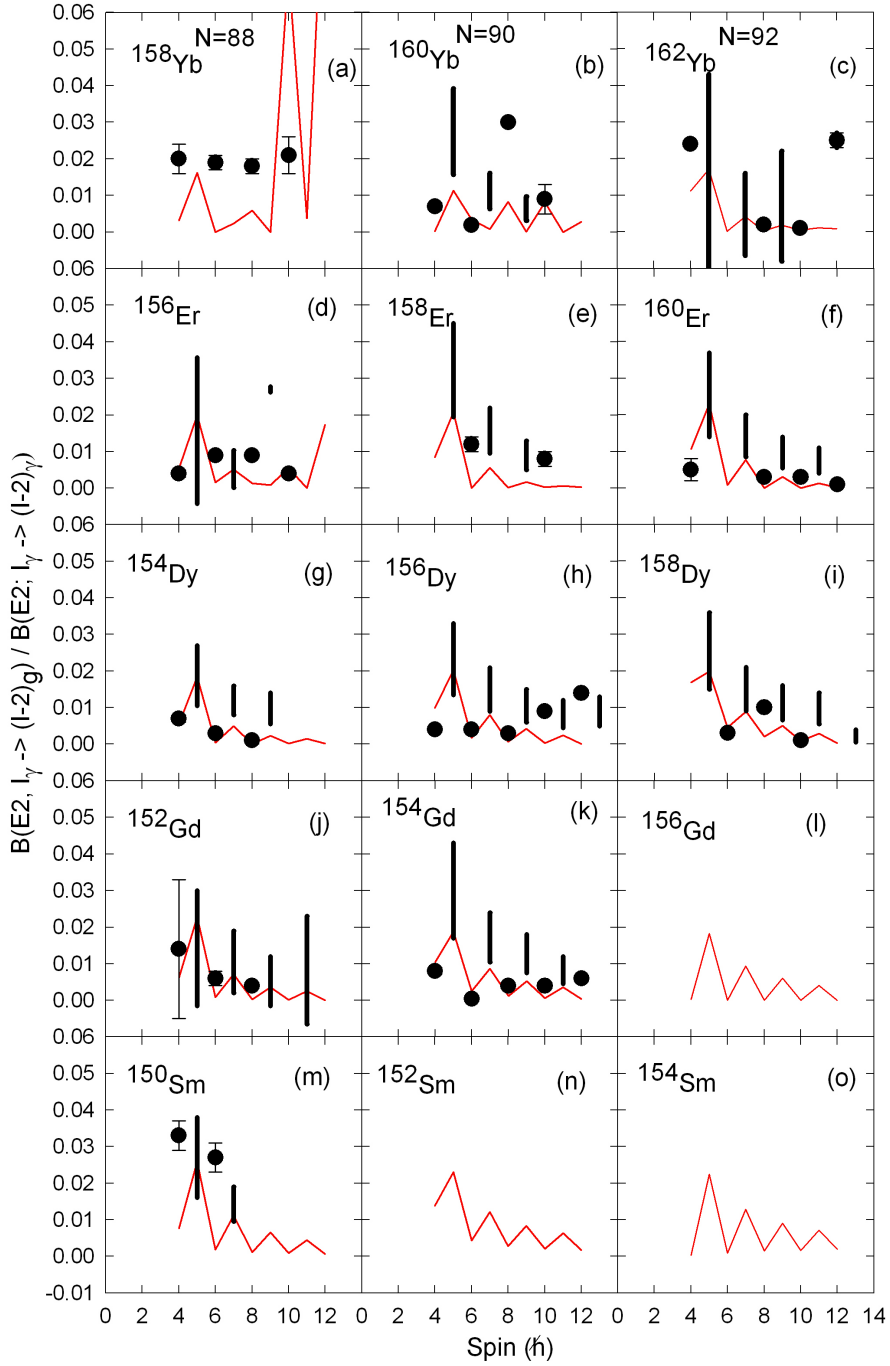

Figure 46: The available experimental branching ratios for out-of-band to in-band transitions, $B(E2; I_\gamma \rightarrow (I-2)_g)/B(E2; I_\gamma \rightarrow (I-2)_\gamma$ for the γ bands in the N = 88, 90, and 92 isotones, in comparison with the theoretical calculations. Modified from [18]. The vertical lines can be understood as an error bar, thus implying that the $B(E)$ value with a correct mixing ratio lies anywhere within the limit.

5.5 Signature Splitting

The signature splitting between the even and odd-γ bands plays an important role in identifying whether a nucleus is γ-soft or γ-rigid [49]. According to Ref. [50], the presence of signature splitting in γ bands indicates that there is a γ-deformation. The signature splitting is calculated using equation 15 [51],

$$S(I) = \frac{[E(I) - E(I-1)] - [E(I-1) - E(I-2)]}{E(2_1^+)} \tag{15}$$

Where $E(I)$, $E(I-1)$, and $E(I-2)$ are the excited energy levels for γ bands at spins, I, $I-1$, and $I-2$ respectively. $E(2_1^+)$ denotes the energy level of the first excited 2^+ state. Significant signature splitting between the even and odd spin members of the γ band is observed in ^{162}Yb (see Figure 37) , which is due to the crossing of the 0_2^+ band with the even- spin members of the γ band. A full analysis of this crossing will be published later [52].

5.6 Band Crossings

There are many observations that have been made in nuclear physics that account for the shape and the behavior of the nucleus. One of those observations is the band crossing, observed in many deformed nuclei, especially those in the rare-earth region.
In many deformed nuclei, the band crossings between the ground-state band and the S-band are normally observed around spins $10^+ - 14^+$. Some of these band crossings in the $A \sim 160$ region are observed as a result of rotation aligments of a pair of $i_{\frac{13}{2}}$ neutrons [53].

In explaining and classifying the observed bands in deformed nuclei, we use Cranked shell model calculations [19]. The experimental data can be compared with the Cranked Shell Model calculations by transforming the measured level energies and spins to the energies (e') in the rotating frame. The calculated quasi-neutron energies in the rotating frame are shown in Figure 1. In this figure, the slope of the quasi-neutron states are related to the aligned angular momentum i, that is, the alignment of a band is the negative of the slope, $i = -de'/d\omega$. It is quite obvious that the largest slopes in this figure are those corresponding to the $i_{13/2}$ orbits.

As mentioned above, one needs to transform the experimental quantities into a rotating frame in order to compare them with the Cranked Shell Model calculations.
Consider a nucleus decaying from a state with spin $I+1$ to a state with spin $I-1$, the angular momentum I_x and the total experimental Routhian are respectively defined as,

$$I_x = \sqrt{I(I+1) - K^2} \sim \sqrt{I + \frac{1}{2} - K^2} \tag{16}$$

and

$$e'(I) = \frac{E(I+1) + E(I-1)}{2} - \hbar\omega(I) I_x(I) \tag{17}$$

where $E(I+1)$ and $E(I-1)$ are the excitation energy of the levels with spin $I+1$ and $I-1$. The experimental rotational frequency, $\hbar\omega$, between the two intermediate spin levels is given by,

$$\hbar\omega(I) = \frac{dE}{dI_x} = \frac{E(I+1) - E(I-1)}{I_x(I+1) - I_x(I-1)} \tag{18}$$

A substraction of the Routhian and aligned angular momentum of a reference core from experimental data is required when a comparison is made between the experimental quantities and CSM theoretical quantities. This substraction removes the contribution by core, and shows the behavior of the quasiparticles only.
The experimental quasiparticles Routhian and alignment are respectively defined as,

$$e'_{exp}(I) = E'_{exp}(I) - E'_{ref}(I) \tag{19}$$

and

$$i = I_x - I_{xg} \tag{20}$$

where I_x is the angular momentum along the rotation axis and I_{xg} is given by equation 21,

$$I_{xg} = (\eth_0 + \eth_1\omega^2)\omega \tag{21}$$

In this equation, $\eth_0$ and $\eth_1$ are Harris parameters [54] and ω is the rotational frequency. The angular momentum, I_x, and the rotational frequency, ω, are well explained in refs. [55, 56].

Thus, the experimental alignment i and Routhian e'_{exp} can be compared directly with the theoretical alignment and Routhian.

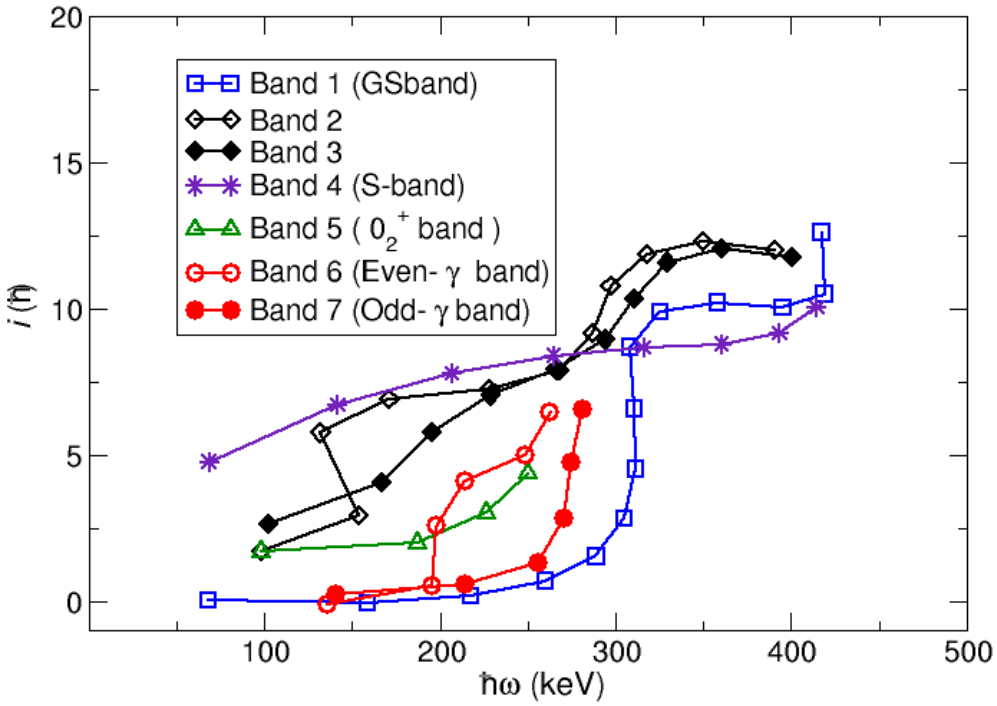

Figure 47: Alignment plots for all bands observed in ^{162}Yb, the Harris parameters used in this plot are 20 MeV^{-1} and 90 MeV^{-3} taken from ref. [55].

In the nucleus ^{162}Yb, there are several band crossings that have been observed. A nice and clear way to show these bands crossing is in the plot of aligned angular momentum, i, given by equation 20 [55], as a function of rotational frequency multiplied by $\hbar$. Shown in Figure 47 is the alignment plot for all bands observed in ^{162}Yb. In this figure, it can be seen that the crossing between the ground-state band and S-band occurs at $\hbar\omega \sim 280$ keV.

The band crossing can also easily be seen when one plots the experimental energies in a rotating frame (Routhian) as the function of $\hbar\omega$. These band crossings are shown in Figure 48. The plots shown in this figure show that the ground-state band is crossed by the S-band at $\hbar\omega \sim 280$ keV which is usual in the neighboring nuclei. Interestingly, the interaction between the ground-state band and a S-band is very weak indeed but then

there is a strong up-bend in the ground-state band at $\hbar\omega \sim 310$ keV (see Figure 47). This up-bend is presumably due to the aligments of a pair of $i_{\frac{13}{2}}$ neutrons. The up-bend in the odd-spin members of the γ band is at $\hbar\omega = 280$ keV.

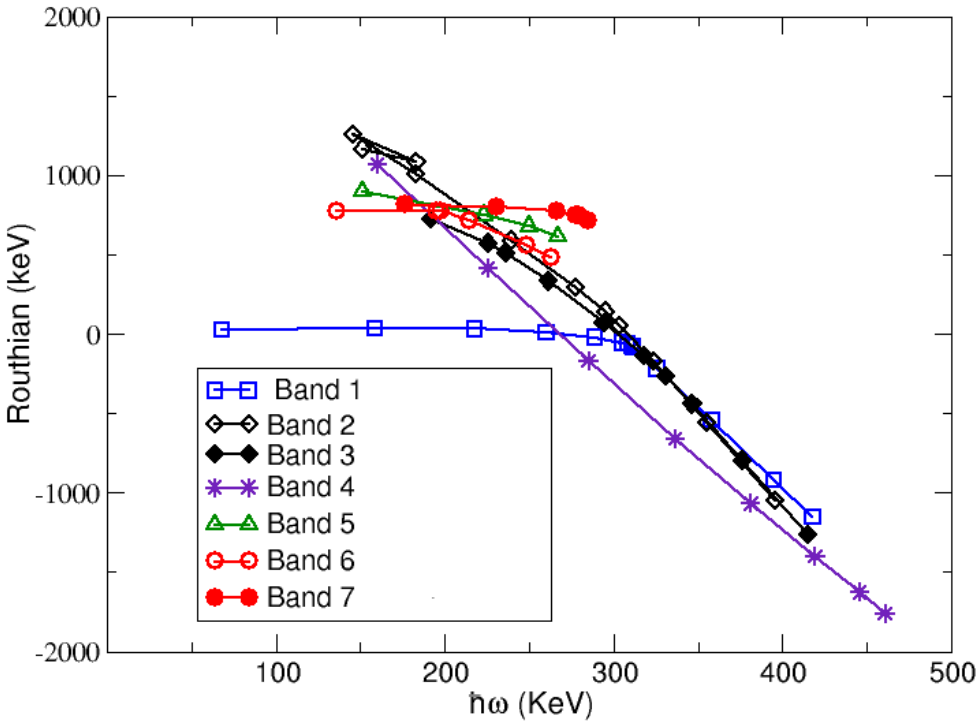

Figure 48: Shows the experimental energies in the rotating frame (Routhian) for bands observed in ^{162}Yb.

6 Conclusion

The spectroscopy of the nucleus ^{162}Yb has been studied. The data for the nucleus of interest (^{162}Yb) was collected at iThemba LABS, using the ^{150}Sm (^{16}O, 4n) ^{162}Yb fusion evaporation reaction. The gamma rays emitted from the reaction products were detected using the AFRODITE γ ray spectrometer equipped with escape-suppressed clover detectors. A total of 10 bands have been observed in this work. We observed all the bands and almost all the γ ray transitions that had been reported by previous experiments [10, 11]. The current study has not only confirmed all the rotational structures reported by previous in-beam works but has also extended the level scheme of ^{162}Yb by establishing 6 new bands. The DCO and polarization measurements have been used to confirm and assign spins and parities of well established structures and the majority of our newly established bands.

A band built on the low lying $K^{\pi} = 0_2^+$ excitation has been identified for the first time in this study. In addition, for the first time in ^{162}Yb, we also report rotational levels that form band structures of both the odd and even spin components of the $K^{\pi} = 2^+$ γ vibrational band. The microscopic properties of these bands are then theoretically explained with the aid of the five-dimensional collective Hamiltonian (5DCH) based on the covariant density functional theory (CDFT) [16, 17]. The rotational properties of both the 0_2^+ and γ bands are in good agreement with the predictions of the five-dimensional collective Hamiltonian calculations, particularly the energy levels and transition rates. This therefore implies that the former (i.e 0_2^+ band in ^{162}Yb) may be interpreted in a traditional sense, as a β vibrational band – without invoking the second vacuum hypothesis. However, if the traditional interpretation of the 0_2^+ band as a β vibrational band is to be accepted in this region, a more stringent test is required (i.e $E0$ transition strengths). The newly established odd γ band is consistent with the systematic behavior of γ bands in the transitional rare earth region. The general feature of γ bands in the transitional rare earth region is that these bands track the ground-state configuration. This feature is also well reproduced by the calculations. The calculations also predict a small signature

splitting between the even and odd γ bands, however, the present work observed a much bigger signature splitting compared to the theoretical ones. We believe that the reason for this significant signature splitting could be that the even-spin states mix with nearby states of the same spin and parity. This mixing causes the even γ band to lie lower in energy than the odd γ band, resulting in a much bigger signature splitting.

A comprehensive systematic review has also been performed for low lying positive parity bands of nuclei in the $A \sim 160$ mass region - with emphasis on $N \sim 90$ isotones and they are compared with the experimental results of the nucleus of interest, namely ^{162}Yb. Generally, there is a remarkably good agreement between the measured observables and the 5DCH-CDFT calculations – in terms of the level energies and transition rates. However, there is a minor discrepancy between data and theory (in terms of level energies) for some of the $N = 92$ isotones, particularly for 0_2^+ bands. Finally, the even spin γ band in ^{158}Yb, previously identified as a 0_2^+ band in [33], has been revised in the current study and is now interpreted as an even spin γ band.

7 Appendix Table of gamma rays in ^{162}Yb

The table below shows the DCO ratios (R_{DCO}) and the polarization (A_P) measured for the γ-ray energies (E_γ) together with the assigned multipolarities (γ Mult.).
E_i (I_i^π) and E_f (I_f^π) represent the initial and final energy levels (spins) for the γ-ray energies, respectively. The γ-ray energies that have been observed for the first time in this current work are marked by (*). Entries marked with dash (-) refers to the information that could not be obtained. Tentative spins and parities are given within parentheses.

Band 1							
E_i (keV)	I_i^π	E_γ (keV)	E_f (keV)	I_f^π	R_{DCO}	A_P	γ Mult.
167	2^+	167	0	0^+	0.943 (10)	-	$E2$
488	4^+	321	167	2^+	1.009 (6)	0.119 (10)	$E2$
925	6^+	437	488	4^+	1.089 (7)	0.149 (10)	$E2$
1446	8^+	521	925	6^+	1.084 (7)	0.134 (10)	$E2$
2024	10^+	579	1446	8^+	0.915 (19)	0.164 (13)	$E2$
2635	12^+	611	2024	10^+	1.031 (8)	0.112 (17)	$E2$
3259	14^+	624	2635	12^+	1.115 (12)	0.151 (28)	$E2$
3880	16^+	621	3259	14^+	1.184 (17)	0.136 (20)	$E2$
4497	18^+	617	3880	16^+	0.932 (48)	0.103 (37)	$E2$
5148	20^+	651	4497	18^+	1.115 (142)	0.275 (28)	$E2$
5864	22^+	716	5148	20^+	1.026 (33)	0.112 (62)	$E2$
6655	24^+	790	5864	22^+	1.010 (35)	0.266 (82)	$E2$
7492	26^+	836	6655	24^+	1.056 (74)	0.220 (114)	$E2$

Band 2							
E_i (keV)	I_i^π	E_γ (keV)	E_f (keV)	I_f^π	R_{DCO}	A_p	γ Mult.
1610	4^-	1122	488	4^+	0.555 (35)	-	-
1610	4^-	617*	993	3^-	0.589 (86)	-	-
1914	6^-	304*	1610	4^-	0.948 (81)	0.188 (79)	$E2$
1914	6^-	990*	925	6^+	0.586 (145)	0.499 (75)	$E1$
1914	6^-	430*	1485	5^-	0.740 (40)	-0.152 (74)	$M1$
2281	8^-	367*	1914	6^-	1.004 (31)	-	$E2$
2281	8^-	513	1769	7^-	0.813 (38)	-0.061 (44)	$M1/E2$
2281	8^-	835	1446	8^+	0.705 (45)	0.037 (59)	$M1$
2573	10^-	292	2281	8^-	0.894 (7)	0.218 (21)	$E2$
2573	10^-	420	2153	9^-	0.734 (19)	-0.036 (38)	$M1$
2573	10^-	549	2025	10^+	0.904 (42)	0.107 (109)	$E1$
2939	12^-	366	2573	10^-	1.312 (9)	0.350 (17)	$E2$
3418	14^-	479	2939	12^-	0.963 (7)	0.166 (14)	$E2$
3974	16^-	556	3418	14^-	0.997 (9)	0.194 (18)	$E2$
4564	18^-	590	3974	16^-	0.930 (10)	0.208 (25)	$E2$
5172	20^-	608	4564	18^-	1.062 (19)	0.058 (32)	$E2$
5819	22^-	647	5172	20^-	1.089 (22)	0.069 (48)	$E2$
6530	24^-	712	5819	22^-	1.063 (61)	0.351 (90)	$E2$
7321	26^-	791	6530	24^-	1.107 (91)	-	$E2$

Band 3

E_i (keV)	I_i^π	E_γ (keV)	E_f (keV)	I_f^π	R_{DCO}	A_p	γ Mult.
1484	5^-	997*	488	4^+	0.518 (105)	0.258 (78)	$E1$
1769	7^-	284	1485	5^-	-	-	
1769	7^-	844	925	6^+	0.463 (244)	0.193 (31)	$E1$
2153	9^-	384	1769	7^-	1.016 (53)	0.047 (79)	$E2$
2605	11^-	452	2153	9^-	1.010 (13)	0.068 (32)	$E2$
2605	11^-	581	2024	10^+	-	0.054 (16)	$E1$
3078	13^-	473	2605	11^-	-	0.036 (36)	$E2$
3602	15^-	521	3078	13^-	1.011 (6)	0.054 (12)	$E2$
4190	17^-	589	3601	15^-	1.073 (38)	0.075 (23)	$E2$
4827	19^-	636	4190	17^-	1.025 (36)	0.146 (37)	$E2$
5488	21^-	661	4827	19^-	1.055 (30)	0.244 (48)	$E2$
6182	23^-	693	5488	21^-	0.785 (69)	0.303 (112)	$E2$
6934	25^-	752	6181	23^-	-	-	-
7764	27^-	831	6934	25^-	-	-	-

Band 4

E_i (keV)	I_i^π	E_γ (keV)	E_f (keV)	I_f^π	R_{DCO}	A_p	γ Mult.
2806	12^+	782	2024	10^+	0.725 (134)	0.105 (18)	$E2$
2806	12^+	382	2425	10^+	0.974 (43)	0.241 (27)	$E2$
2806	12^+	212*	2595	10^+	1.092 (122)	-	$E2$
2806	12^+	176*	2631	10^+	1.054 (92)	-	$E2$
3126	14^+	321	2806	12^+	1.009 (6)	0.119 (10)	$E2$
3578	16^+	452	3126	14^+	1.073 (7)	0.279 (13)	$E2$
4148	18^+	571	3578	16^+	1.112 (10)	0.206 (20)	$E2$
4822	20^+	673	4148	18^+	1.110 (16)	0.210 (30)	$E2$
5584	22^+	763	4822.	20^+	1.056 (23)	0.162 (27)	$E2$
6423	24^+	839	5584	22^+	0.851 (38)	0.120 (44)	$E2$
7315	26^+	892	6423	24^+	1.108 (217)	-	$E2$
8237	28^+	922	7315	26^+	-	-	-

Band 5							
E_i (keV)	I_i^π	E_γ (keV)	E_f (keV)	I_f^π	R_{DCO}	A_p	γ Mult.
1343	4^+	1176	167	2^+	1.061 (410)	0.049 (440)	$E2$
1647	6^+	1160	488	4^+	0.862 (48)	0.065 (191)	$E2$
1647	6^+	304*	1343	4^+	0.948 (81)	0.188 (79)	$E2$
2094	8^+	447*	1647	6^+	-	-	$E2$
2094	8^+	1170	925	6^+	-	-	-
2595	10^+	501*	2094	8^+	1.068 (34)	-	$E2$
2595	10^+	1150	1446	8^+	1.042 (683)	-	$E2$
3129	12^+	534*	2595	10^+	-	-	-

Band 6

E_i (keV)	I_i^π	E_γ (keV)	E_f (keV)	I_f^π	R_{DCO}	A_p	γ Mult.
798	2^+	798	0	0^+	-	-	-
1150	4^+	352	798	2^+	1.159 (78)	-	$E2$
1150	4^+	983	167	2^+	1.229 (267)	-	$E2$
1150	4^+	663	488	4^+	1.083 (34)	0.063 (40)	$E2$
1574	6^+	423	1150	4^+	1.070 (19)	0.190 (43)	$E2$
1574	6^+	649	925	6^+	1.025 (26)	0.072 (28)	$E2$
1986	8^+	412	1574	6+	1.053 (10)	0.244 (21)	$E2$
1986	8^+	339	1647	6^+	0.843 (82)	0.380 (53)	$E2$
1986	8^+	1061	925	6^+	0.878 (57)	0.050 (39)	$E2$
1986	8^+	540	1446	8^+	0.947 (48)	-0.072 (32)	$M1/E2$
2425	10^+	439	1986	8^+	1.030 (4)	0.250 (8)	$E2$
2425	10^+	979	1446	8^+	0.878 (216)	0.207 (56)	$E2$
2425	10^+	400	2025	10^+	-	-	-
2930	12^+	505*	2424	10^+	1.282 (27)	-	$E2$
3462	14^+	532*	2930	12^-	1.053 (102)	-	$E2$

Band 7

E_i (keV)	I_i^π	E_γ (keV)	E_f (keV)	I_f^π	R_{DCO}	A_p	γ Mult.
993	3^+	826	167	2^+	1.159 (81)	0.222 (81)	$E2$
993	3^+	505	488	4^+	-	-	-
1394	5^+	401*	993	3^+	1.041 (156)	0.033 (248)	$E2$
1394	5^+	906*	488	4^+	0.660 (62)	0.152 (45)	$M1/E2$
1881	7^+	487*	1394	5^+	1.037 (90)	0.382 (200)	$E2$
1881	7^+	956*	925	6^+	0.695 (165)	-	-
2429	9^+	549*	1881	7^+	1.214 (96)	0.238 (127)	$E2$
2429	9^+	983*	1446	8^+	-	-	-
2996	11^+	566*	2429	9^+	0.973 (55)	-	-
3562	13^+	567*	2996	11^+	-	-	-
4138	15^+	576*	3562	13^+	-	-	-

Band 8							
E_i (keV)	I_i^π	E_γ (keV)	E_f (keV)	I_f^π	R_{DCO}	A_p	γ Mult.
2905	(12^+)	340*	2565	(10^+)	-	-	-
2565	(10^+)	1119	1446	(8^+)	-	-	-
3379	(14^+)	474*	2905	(12^+)	-	-	-
3969	(16^+)	590*	3379	(14^+)	-	-	-

Band 9							
E_i (keV)	I_i^π	E_γ (keV)	E_f (keV)	I_f^π	R_{DCO}	A_p	γ Mult.
3129	(2^+)	268*	2880	(10^+)	-	-	-
3129	(12^+)	1104	2025	(10^+)	-	-	-
3426	(14^+)	297*	3129	(12^+)	-	-	-
3835	(16^+)	409*	3426	(14^+)	-	-	-

Band 10							
E_i (keV)	I_i^π	E_γ (keV)	E_f (keV)	I_f^π	R_{DCO}	A_p	γ Mult.
2631	(10^+)	1185	1446	(8^+)	-	-	-
3911	(14^+)	600*	3311	(12^+)	-	-	-
3311	(12^+)	1287	2025	(12^+)	-	-	-

References

[1] J. F. Sharpey-Schafer et al., Eur. Phys. J. A47, 5 (2011)

[2] J. F. Sharpey-Schafer et al., Eur. Phys. J. A47, 6 (2011).

[3] S. P. Bvumbi et al., Phys. Rev. C87, 044333 (2013).

[4] T. S. Dinoko, PhD. thesis, UWC (2014).

[5] L. Msebi, MSc thesis, UJ (2016).

[6] G. L. Zimba, MSc thesis, UJ (2015).

[7] S. N. T. Majola, MSc thesis, UCT (2011).

[8] R. A. Bark et al., Phys. Rev.Lett. 104, 022501 (2010).

[9] J. F. Sharpey-Schafer, Nucl. Phys. News. Int. 14, 5 (2004).

[10] J. N. Mo et al., Nucl. Phys. A472, 285 (1987).

[11] E. A. McCutchan el al., Phys. Rev. C69, 024308 (2004).

[12] N. Blasi et al., Phys. Rev. C88, 014318 (2013).

[13] A. Bohr and Mottelson, Nuclear Structure, Volume .II, Singapore: Word Scientific,(1998).

[14] P. E. Garrett, J. Phys. G27, R1 (2001).

[15] L. Próchniak, K. Zajac, K. Pomorski, S.Rohoziński, and J. Srebrny, Nucl. Phys. A 648, 181 (1999)

[16] T. Niksšić, Phys. Rev. C79, 034303 (2009).

[17] Z.P. Li et al., Phys. Rev. C 79, 054301 (2009)

[18] Z. Shi, B. Y Song, Z. P. Li, and S.Q. Zhang, Description of low-lying spectroscopy in even-even $N \sim 88$, 90, and 92 isotones with five-dimensional collective Hamiltonian based on covariant density functional, (2016) to be published.

[19] R. Bengtsson, S.Frauendorf, and F.-R. May, Atomic Data and Data Tables, Vol. 35, 15-122 (1986).

[20] N. Bohr, Transmutation of Atomic Nuclei, Science 86, 2225 (1937).

[21] N. Bohr and J. A. Wheeler., Phys. Rev. 56, 426 (1939).

[22] K. S. Krane, Introductory Nuclear Physics, John Wiley & Sons. inc., (1988).

[23] J. Rainwater, Phys. Rev. 79, 432 (1950).

[24] A. Bohr and B. R. Mottelson, Phys. Rev. 90, 717L (1953).

[25] http://www.personal.soton.ac.uk/ab1u06/teaching/phys3002/course/05_shell.pdf (2016).

[26] https://www.physics.uoguelph.ca/garrettp/Collective-ex-def.htm (2016).

[27] C. Wheldon, Ph.D. thesis, University of Surrey, (1999).

[28] L. Dommelen, Quantum Mechanics for Engineers, Version 5.55 alpha (2012).

[29] A. Bohr and Mottelson, Nuclear Structure, Volume .II, Singapore: Word Scientific, P. 363 (1998).

[30] http://www.tlabs.ac.za/wp-content/uploads/pdf/RobWorkshop2011.pdf

[31] S. S. Ntshangase, PhD. thesis, UCT (2011).

[32] http://lise.nscl.msu.edu/pace4.html (2016).

[33] S. N. T. Majola, Ph.D. thesis, UCT (2015).

[34] Radford D. C., http://radware.phy.ornl.gov/rw/esclev/- esclev.html, (2000).

[35] Radford D. C., Nucl. Instr. and Meth., A361, 297, (1995).

[36] D. G. Roux et al., Eur. Phys. J. A48, 99 (2012).

[37] K. Starosta el al., Nucl. Instrum. Methods A 423, 16 (1999).

[38] M. A. Sithole, MSc thesis, UWC (2017) to be submitted.

[39] B. Rubio and W. Gelletly, Beta decay of exotic nuclei, Lect. Notes Phys. 764, 99-151 (2009).

[40] https://www.jyu.fi/fysiikka/en/research/accelerator/nucspec/JUROGAM.

[41] I. Y. Lee. The GAMMASPHERE. Nuclear Physics A 520, 641c–655c, (1990).

[42] P. A. Pipidis, Ph.D thesis, The Florida State University (2006).

[43] J.F. Sharpey-Schafer et al., Evolution of γ bands, Proc. XLIX Int. Winter Meeting on Nucl. Phys., Bormio, Italy. (2011).

[44] L. D. Landau, Phys. Z. Sov. 2, 46 (1932).

[45] C. Zenner, Proc. Roy. Soc. London A137 , 696 (1932).

[46] P. Ring and P. Schuck, The Nuclear Many-Body Problem (Springer-Verlag, Berlin, 526 (1980))

[47] D. M. Cullen et al., Phys. Rev. Lett. 65, 1547 (1990).

[48] H. Moriga and T. Yamazaki, In-beam gamma-ray spectroscopy, (North-Holland publishing company, Amsterdam New York Oxford, 1976).

[49] J. M. Rees et al., Phys. Rev. C83, 04431 (2011).

[50] S. N. T. Majola et al., Phys. Rev. C91, 034330 (2015).

[51] R. F. Casten, Nuclear Structure From A Simple Perspective (Oxford University Press, Oxford, P. 194 (1990)).

[52] L. Mdletshe et al, (2017) to be published.

[53] F. S. Stephens and R. S. Simon, Nucl. Phys. A183, 257 (1972).

[54] S. M. Harris, Phys. Rev. B138, 509 (1965).

[55] L. L. Riedinger, Nucl. Phys. A347, 141-169 (1980).

[56] O. Shirinda, MSc thesis, UWC (2007).